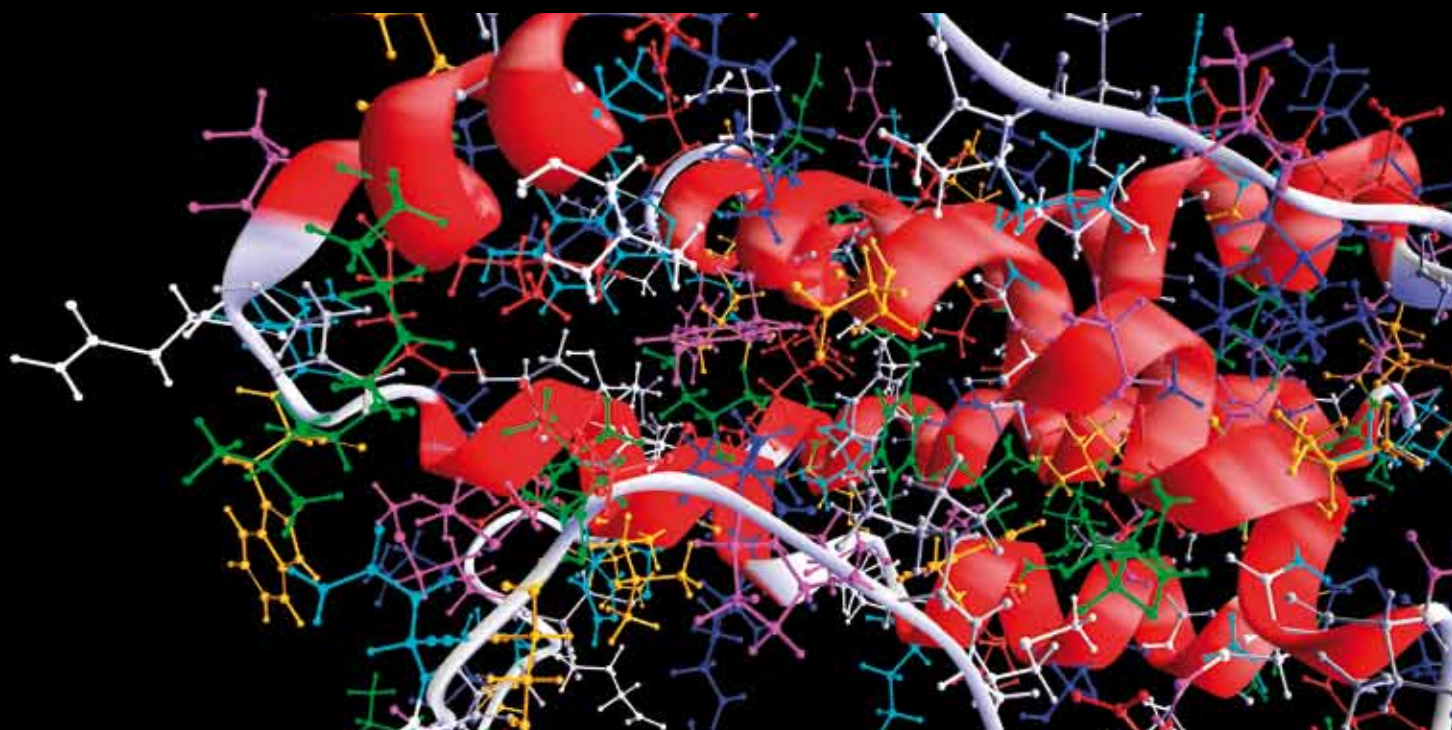


INTEGRATIVE APPROACHES IN COMPUTATIONAL BIOMEDICAL IMAGING 2013

GUEST EDITORS: HUAFENG LIU, PENGCHENG SHI, AND YUNMEI CHEN





**Integrative Approaches in Computational
Biomedical Imaging 2013**

Computational and Mathematical Methods in Medicine

**Integrative Approaches in Computational
Biomedical Imaging 2013**

Guest Editors: Huafeng Liu, Pengcheng Shi, and Yunmei Chen



Copyright © 2014 Hindawi Publishing Corporation. All rights reserved.

This is a special issue published in “Computational and Mathematical Methods in Medicine.” All articles are open access articles distributed under the Creative Commons Attribution License, which permits unrestricted use, distribution, and reproduction in any medium, provided the original work is properly cited.

Editorial Board

Emil Alexov, USA
Georgios Archontis, Cyprus
Dimos Baltas, Germany
Chris Bauch, Canada
Maxim Bazhenov, USA
Thierry Busso, France
Carlo Cattani, Italy
Sheng-yong Chen, China
William Crum, UK
Ricardo Femat, Mexico
Alfonso T. Garca-Sosa, Estonia

Damien Hall, Australia
Volkhard Helms, Germany
Seiya Imoto, Japan
Lev Klebanov, Czech Republic
Quan Long, UK
C-M Charlie Ma, USA
Reinoud Maex, France
Michele Migliore, Italy
Karol Miller, Australia
Ernst Niebur, USA
Kazuhisa Nishizawa, Japan

Hugo Palmans, UK
David James Sherman, France
Sivabal Sivaloganathan, Canada
Nestor V. Torres, Spain
Nelson J. Trujillo-Barreto, Cuba
Gabriel Turinici, France
Kutlu O. Ulgen, Turkey
Edelmira Valero, Spain
Guang Wu, China
Henggui Zhang, United Kingdom

Contents

Integrative Approaches in Computational Biomedical Imaging 2013, Huafeng Liu, Pengcheng Shi, and Yunmei Chen

Volume 2013, Article ID 757380, 1 page

Investigation on Cardiovascular Risk Prediction Using Physiological Parameters, Wan-Hua Lin, Heye Zhang, and Yuan-Ting Zhang

Volume 2013, Article ID 272691, 21 pages

A Novel Multiinstance Learning Approach for Liver Cancer Recognition on Abdominal CT Images Based on CPSO-SVM and IO, Huiyan Jiang, Ruiping Zheng, Dehui Yi, and Di Zhao

Volume 2013, Article ID 434969, 10 pages

Fast and Automatic Ultrasound Simulation from CT Images, Weijian Cong, Jian Yang, Yue Liu, and Yongtian Wang

Volume 2013, Article ID 327613, 13 pages

Automatic Sex Determination of Skulls Based on a Statistical Shape Model, Li Luo, Mengyang Wang, Yun Tian, Fuqing Duan, Zhongke Wu, Mingquan Zhou, and Yves Rozenholc

Volume 2013, Article ID 251628, 6 pages

An Approach for the Visualization of Temperature Distribution in Tissues According to Changes in Ultrasonic Backscattered Energy, Jingjing Xia, Qiang Li, Hao-Li Liu, Wen-Shiang Chen, and Po-Hsiang Tsui

Volume 2013, Article ID 682827, 10 pages

Automatic Vasculature Identification in Coronary Angiograms by Adaptive Geometrical Tracking, Ruoxiu Xiao, Jian Yang, Mahima Goyal, Yue Liu, and Yongtian Wang

Volume 2013, Article ID 796342, 11 pages

Editorial

Integrative Approaches in Computational Biomedical Imaging 2013

Huafeng Liu,¹ Pengcheng Shi,² and Yunmei Chen³

¹ State Key Laboratory of Modern Optical Instrumentation, Zhejiang University, Hangzhou 310027, China

² B. Thomas Golisano College of Computing and Information Sciences, Rochester Institute of Technology, Rochester, NY 14623, USA

³ Department of Mathematics, University of Florida, 458 Little Hall, Gainesville, FL 32611-8105, USA

Correspondence should be addressed to Huafeng Liu; liuhf@zju.edu.cn

Received 9 December 2013; Accepted 9 December 2013; Published 27 January 2014

Copyright © 2014 Huafeng Liu et al. This is an open access article distributed under the Creative Commons Attribution License, which permits unrestricted use, distribution, and reproduction in any medium, provided the original work is properly cited.

Biomedical imaging has continued to play increasingly important roles in clinical practice and research activities. While the enormous amount of imaging data provides observations on the organisms of interest, these data have to be properly analyzed in order to reveal the *insights* into the biological and physiological processes.

This special issue, following the very successful one in 2012, provides a snapshot of the latest and emerging computational biomedical imaging technologies and their applications in clinics and research. From the 20 submissions that have gone through the peer-review process, the guest editors have selected six papers covering some very interesting and timely topics, from forensic medicine to cardiovascular risk assessment.

The work of W. Lin et al. attempts to predict cardiovascular risk by using a combination of physiological parameters, including blood pressure, electrocardiogram, arterial stiffness, ankle-brachial blood pressure index, and blood glucose carrying valuable information. This paper provides the current status on the medical devices for physiological measurements and presents various points of view on potential implications for promoting cardiovascular disease prevention and treatment in the future.

Ultrasound imaging is the focus of the next two papers. The paper by J. Xia et al. presents an original concept for the visualization of temperature distribution in tissue building upon changes in ultrasonic backscattered energy. This approach visualizes temperature map in tissues during nonuniform heating without the need of tracking and

compensation of the echo shift. W. Cong et al. describe an intriguing platform to simulate ultrasound based on CT images, which has the potential to facilitate ultrasound guided navigation in clinical practice.

The paper by R. Xiao et al. focuses on vessel tracking for coronary artery identification. The system integrates multiscale Hessian information and discriminates the connecting relationship of the tracked ridge points in order to automatically track vessel from X-ray angiograms. This work has demonstrated its capability through clinical evaluation.

H. Jiang et al. present clinically important work on recognizing liver cancer from abdominal CT images by using multi-instance learning and support vector machine, which aims to improve the efficiency for liver cancer detection. The other paper of the special issue explores a novel application in forensic medicine and the determination of sex from 3D digital skulls using statistical shape model. The method has been tested on 208 skulls with very promising results.

We appreciate the many high quality submissions to this special issue from leading researchers in computational biomedical imaging.

Huafeng Liu
Pengcheng Shi
Yunmei Chen

Review Article

Investigation on Cardiovascular Risk Prediction Using Physiological Parameters

Wan-Hua Lin,^{1,2} Heye Zhang,^{1,2} and Yuan-Ting Zhang^{2,3}

¹SIAT-Institute of Biomedical and Health Engineering, Chinese Academy of Sciences, Shenzhen 518055, China

²The CAS Laboratory for Health Informatics, Shenzhen Institutes of Advanced Technology, Shenzhen 518055, China

³Department of Electronic Engineering, Joint Research Centre for Biomedical Engineering, The Chinese University of Hong Kong, Hong Kong

Correspondence should be addressed to Yuan-Ting Zhang; ytzhang@ee.cuhk.edu.hk

Received 14 July 2013; Accepted 23 September 2013

Academic Editor: Huafeng Liu

Copyright © 2013 Wan-Hua Lin et al. This is an open access article distributed under the Creative Commons Attribution License, which permits unrestricted use, distribution, and reproduction in any medium, provided the original work is properly cited.

Cardiovascular disease (CVD) is the leading cause of death worldwide. Early prediction of CVD is urgently important for timely prevention and treatment. Incorporation or modification of new risk factors that have an additional independent prognostic value of existing prediction models is widely used for improving the performance of the prediction models. This paper is to investigate the physiological parameters that are used as risk factors for the prediction of cardiovascular events, as well as summarizing the current status on the medical devices for physiological tests and discuss the potential implications for promoting CVD prevention and treatment in the future. The results show that measures extracted from blood pressure, electrocardiogram, arterial stiffness, ankle-brachial blood pressure index (ABI), and blood glucose carry valuable information for the prediction of both long-term and near-term cardiovascular risk. However, the predictive values should be further validated by more comprehensive measures. Meanwhile, advancing unobtrusive technologies and wireless communication technologies allow on-site detection of the physiological information remotely in an out-of-hospital setting in real-time. In addition with computer modeling technologies and information fusion. It may allow for personalized, quantitative, and real-time assessment of sudden CVD events.

1. Introduction

Cardiovascular disease (CVD) remains the world's top killer for death at this moment. As reported by World Health Organization [1], CVD will continue to dominate mortality trends in the coming decades. Moreover, it is always associated with substantial socioeconomic burden. Therefore, a considerable demand to improve cardiovascular health is greatly desired.

CVDs are chronic diseases that occur by long-term cumulative effects of risk factors. Besides, a large number of people die from acute cardiovascular events without prior symptoms [2]. And about two-thirds of deaths caused by CVD occur in out-of-hospital conditions [3]. It is therefore important to develop effective risk prediction approaches for screening individuals who are at high risk of developing CVD for timely prevention and treatment at an early stage before obvious symptoms happen.

In the past decades, several prediction models have been proposed to estimate a 10-year risk of developing CVD. The models are expressed as multivariate regression equations using risk factors as variables. The most influential model is the Framingham Risk Score (FRS), which predicts coronary heart disease (CHD) using traditional risk factors as follows: age, diabetes, smoking, systolic blood pressure (SBP), treatment for hypertension, total cholesterol, and high-density lipoprotein (HDL) cholesterol [4]. Other similar risk-scoring algorithms, such as ATP-III [5], SCORE [6], PROCAM [7], QRICK [8], Reynolds Risk Score [9, 10], and MUCA [11], are accomplished through the incorporation of factors into the FRS or recalibration of the Framingham functions to the local subjects. These prediction models have become primary tools in the prevention of CVD in clinical practice. Based on these models, individuals classified in low risk stratum, intermediate stratum, and high risk stratum

are recommended for lifestyle modification, further risk stratification or drug therapy, and more intensive preventive interventions, respectively [12].

However, they still have several known limitations. An example is that a considerable number of CVD events still occur in those asymptomatic patients who are classified into intermediate risk stratum [13]. Another example is that if subjects classified in the Framingham low-risk stratum are excluded from further screening, about a quarter of men and two-thirds of women with substantial atherosclerosis will be missed, where atherosclerosis is the main cause of CVD [14]. Therefore, in addition to traditional prediction approaches, further efforts should be made to develop novel strategies for accurately screening CVD.

Incorporation or modification of the risk factor that has an independent prognostic value of current prediction models would be a good choice for improving the performance of the prediction models. Some studies have reported the role of imaging [15], genetic test [16], and biomarker assay [17] in improving early CVD prediction. However, until now, there is not a study systematically reporting the role of physiological parameters for CVD prediction. Physiological parameters of the heart and arteries can be measured from the body surface by noninvasive tests and can be used for identifying multiphysics mechanisms of the cardiovascular system. Specifically, blood pressure (BP) reflects the hemodynamics inside the arteries. It is well known that high BP is a major cause of the development of atherosclerosis, an artery clogging and hardening process that results in heart attacks or strokes [18]. Electrocardiogram (ECG) measures the electrophysiology of the heart. Abnormalities on ECG can be used for screening vulnerable myocardium, which may lead to acute myocardial infarction [19]. Arterial stiffness measured by aortic pulse wave velocity (PWV) or pulse wave analysis reflects the blood fluid flow in the arteries and the hardening degree of the artery wall [20], where arterial hardening is a consequence of arteriosclerosis. Ankle-brachial blood pressure index (ABI), which is defined as the ratio of systolic pressure at the ankle to that in the arm, can be used for evaluating structural and functional changes in the blood vessel and has been used for measuring peripheral vascular disease. Blood glucose carries the biochemical information of the blood. Elevated plasma glucose may cause several conditions that relate to the development of cardiovascular complications [21]. Moreover, increased hemodynamics of blood flow and mechanical shear stress of the coronary wall, which are reflected in the increases in BP, heart rate, and PWV, in combination with the increases in blood viscosity, are responsible for triggering plaque rupture and consequence progression of CVD [19, 22], where, plaque rupture accounts for around 70% of acute cardiac deaths [19].

Except for established physiological risk factors (clinical SBP and diabetes) adopted in the traditional prediction models, more studies find that emerging physiological parameters extracted from ambulatory BP, stress BP, ECG, arterial stiffness, ABI, and milder glucose abnormalities are also related to the occurrence of CVD. For examples, the Ohasama study shows that the heart rate variability (HRV) and blood pressure variability (BPV) captured by ambulatory

blood pressure monitoring (ABPM) should be regarded as independent risk factors for the prediction of CVD death in general individuals [23]. The Dublin study suggests that the nighttime BP can be more effective in the prediction of CVD mortality than clinical BP [24]. The Framingham study shows that exercise diastolic blood pressure (DBP) during stage 2 of the Bruce protocol and recovery predict incident CVD when adjusted for resting BP [25]. A meta-analysis of 17 longitudinal studies suggests that the risk of subjects with high aortic PWV is almost twice compared with those with lower aortic PWV [26]. The Strong Heart Study shows that low ABI (≤ 0.90) and high ABI (> 1.40) significantly improve the CVD mortality risk [27]. The Framingham Offspring Study indicates that milder glucose abnormalities such as impaired fasting glucose (IFG) or impaired glucose tolerance (IGT) are also independent risk factors for predicting CVD though the predictive values are small, and the risk increases mostly in those with combined IFG and IGT. Medical statistics studies also prove that early morning BP and heart rate surge [22, 28, 29], elevated BP in winter [29], exercise-induced ECG arrhythmias in athletes [30], and electrophysiological abnormalities in obstructive sleep apnea [31] are related to an increased incident of acute CVD events, such as myocardial infarction (MI) and stroke. In addition, noninvasive monitoring of these physiological parameters are convenience, cost-effective, and with low side effects. Therefore, it would be another good choice for improving CVD prediction by the use of physiological parameters that have been proved to be with independent prognostic values.

The objective of this paper is to review current evidences regarding these physiological parameters for CVD prediction, as well as to summarize the current status of the medical devices that used for monitoring these parameters and discuss the potential implications for promoting CVD prevention and treatment in the future.

2. Assessing the Predictive Ability of Risk Factors

Cohort studies in which populations are followed up over time and outcomes are determined prospectively are widely used for measuring the prognostic value of a risk marker for disease prediction and treatment [32]. Generally, the number of the population enlisted should be large and the followup should be conducted for years to get large numbers of outcome events for significant statistical analysis. In these studies, risk is assessed with a survival curve or by reporting the proportion of outcome events over a given period [32]. The statistical association between a risk marker and the outcome can then be tested using the Cox proportional hazards model, linear regression model, logistic regression model, or a parametric survival model and are assessed using metrics such as hazard ratio (HR), odds ratio (OR), or relative risk (RR, equal to relative hazard), along with confidence interval (CI) and P value [20, 32]. The HR refers to the ratio of the hazard rates corresponding to two levels of a variable. For instance, subjects with treatment or a particular exposure may suffer an outcome two times than the control

subjects, giving a HR of 2. The odds ratio refers to the odds that an outcome will occur with a particular exposure, compared to that without the exposure. Relative risk refers to the ratio of the probability of developing a disease in the exposed group versus the control group. Therefore, HR, OR, or RR of 1 means that the exposure or treatment does not influence the risk of developing the outcome, HR, OR, or RR > 1 means exposure or treatment associated with higher risk of developing the outcome, while HR, OR, or RR < 1 means exposure or treatment associated with lower risk of developing the outcome. Consequently, exposures with HR, OR, or RR far from 1 may be considered as risk factors for predicting disease outcome (e.g. CVD). For a risk factor to be considered with independent and incremental predictive value, the metrics should be calculated after adjustment for established risk factors.

More analysis including discrimination, calibration, and reclassification are also recommended by the American Heart Association for assessing the performance of risk prediction models with the inclusion of new markers [12, 32]. Discrimination represents the ability of a prediction model to discriminate cases from no cases [12]. It is quantified using C statistic or C index, which is equal to the area under the receiver operating characteristic curve (AUC) [12, 20]. A test with C statistic of 0.5 means no discrimination, while 1.0 means a perfect test. Calibration measures the capability of predicting accurately the proportion of individuals in a group who will develop disease events. Metric of Hosmer-Lemeshow χ^2 test is usually used for describing the calibration of a risk prediction model [12]. Reclassification refers to the ability whether the individuals reclassified into other risk strata will be more accurate [20]. Net reclassification improvement and integrative discrimination index are two metrics for quantitatively estimating the reclassification [12, 32].

Apart from the statistical measures described above, a new risk marker should also have a positive effect on clinical decisions and eventually on clinical outcomes [32]. Ultimately, the test for capturing the novel risk factor should be cost-effective, so it can be used for screening large scale individuals [32].

3. Initial Studies on Early CVD Prediction Using Physiological Parameters

3.1. Blood Pressure (BP). BP is a consistent risk factor for the development of atherosclerosis [18]. Specially, high BP increases the workload of the heart and injures the endothelium and the delicate lining of the artery walls. Injured endothelium will induce the deposition of cholesterol and cells in the artery wall and eventually lead to the formation of atherosclerosis plaques. Plaques can suddenly rupture, and cause blood clots that can block blood flow travelling to vital organs, such as the heart or the brain. Then ischemic heart disease or cerebrovascular accident will occur. Moreover, stress-induced hemodynamic and hemostatic changes will increase the likelihood of plaque rupture and thrombosis.

Continuous or category variables derived from resting BP, ABPM, and stress BP tests are used for cardiovascular risk

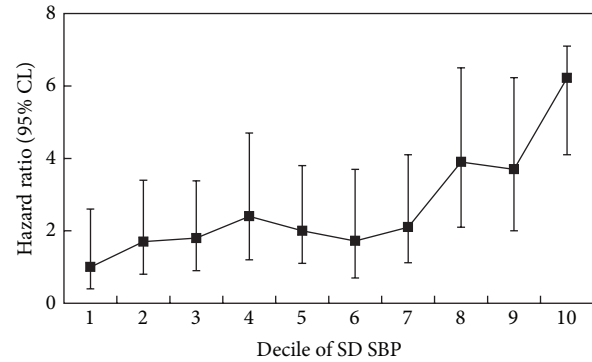


FIGURE 1: Hazard ratios for risk of stroke by deciles of visit-to-visit variability (SD) SBP over seven visit measurements (the interval between visits was 4 months), with the first decile as the control category. Analyses were performed in patients excluding those with a past history of stroke (1324 patients were eligible). Reproduced from [34].

prediction. Table 1 shows some of the representative cohort studies reporting the independent predictive value of BP.

3.1.1. Resting Blood Pressure. Accumulating traditional large scale cohort studies prove that high brachial artery BP at baseline is the most prevalent treatable vascular risk factor [8, 33, 34, 38]. A meta-analysis of one million adults shows that cardiovascular risk starts to increase as SBP rises from 115 mmHg or DBP rises from 75 mmHg to higher values [38]. The Japan Arteriosclerosis Longitudinal Study (JALS) group compares 4 BP indexes (DBP, SBP, pulse pressure [PP], and mean blood pressure [MBP]) and finds that SBP and MBP are the strongest predictors for the long-term incidence of stroke and myocardial infarction (MI), while PP is the weakest predictor of the four BP indexes [33].

In a recent persuasive study, variability in SBP and maximum SBP reached among repeated clinic visits over months are also demonstrated to be strong predictors of stroke, independent of mean SBP. As shown in Figure 1 and Table 1, the HR of the top-decile of SD SBP over seven visits for stroke prediction is 6.22, while the HR of the top-decile of maximum SBP reached for stroke prediction is 15.01, after adjustment for mean SBP (the first decile is the reference category) [34].

Diagnosis and treatment of hypertension are commonly recommended for the prevention of CVD events. Antihypertensive agents that can reduce BPV and MBP both will control the risk of stroke more effectively than agents who reduce MBP only [39, 40]. A meta-analysis finds that effects of drugs on interindividual variation in SBP account for more of the effects of treatment on stroke risk than do effects on mean SBP [41]. Thus, BPV is suggested to be taken into account to the current hypertension guidelines [42].

3.1.2. Ambulatory Blood Pressure. Blood pressures vary greatly according to the daily activities and may reflect the cerebrum central autonomic control. As reported by many

TABLE 1: Sample of cohort studies reporting the independent predictive values of blood pressure.

Markers	Population (no.)	Age at entry (y)	Followup (y)	Covariates	End events (no.)	Model based	Prognostic values	Discrimination, calibration, and reclassification	Reference
SBP	General Japanese man (48224)	40–89	8.4	Age, BMI, serum total cholesterol, and smoking	Stroke (1231) and MI events (220)	Poisson regression model	For stroke, HR = 1.51; For MI, HR = 1.23	NR	[33]
DBP							For stroke, HR = 1.53; For MI, HR = 1.17		
MBP							For stroke, HR = 1.60; For MI, HR = 1.22		
PP							For stroke, HR = 1.27; For MI, HR = 1.17		
Visit-to-visit variability (SD) in SBP	Patients with prev. transient ischaemic attack (1324)	60.3 (mean)	2	Age, sex, mean SBP, and other risk factors	Stroke (270), coronary event (166)	Cox model	For stroke, HR = 6.22	NR	[34]
Maximum SBP reached							For stroke, HR=15.01		
Episodic severe hypertension							For stroke, HR = 3.58		
Residual visit-to-visit variability (SD)	Patients with treated hypertension (2011)	40–79	5.5	NR	Stroke and coronary event	Cox model	For stroke, HR = 3.25	NR	[34]
Variability (CoV) of daytime SBP in ABPM							For vascular events, HR = 1.42		
Clinic SBP;	Subjects fulfilling series of exclusion and inclusion criteria (3344)	52.6 ± 14.5	5.6	Age, sex, and diabetes	Total CVD events (331)	Cox model	HR = 1.35	NR	[35]
Awake SBP mean;							HR = 1.35		
Asleep SBP mean;							HR = 1.52		
48-h SBP mean;							HR = 1.43		
Sleep-time relative decline;							HR = 0.72		
SD of awake SBP;							HR = 1.29		
SD of asleep SBP;							HR = 1.22		
SD of 48-h SBP							HR = 1.24		
Morning surge SBP							HR = 0.79		

TABLE 1: Continued.

Markers	Population (no.)	Age at entry (y)	Followup (y)	Covariates	End events (no.)	Model based	Prognostic values	Discrimination, calibration, and reclassification	Reference
24-h DBP SD;	Subjects referred for assessment of their hypertension (10499)	54.5 (mean)	5.8	Age, sex, and BMI, smoking, prev. CVD, 24-h BP, and 24-h DBP	CV death	Cox model	HR = 1.04	NR	[36]
24-h wDBP SD; DBP ARV;							HR = 1.06 HR = 1.06		
Daytime SBP	Untreated hypertension patients (5292)	16.2–92.4	8.4	Age, sex, BMI, smoking, diabetes, prev. CVD events, and clinic SBP	All-cause mortality (646)	Cox model	HR = 1.07	NR	[24]
Nighttime SBP							HR = 1.15 HR = 1.13		
24-h SBP							RR = 2.69	NR	[23]
Daytime systolic BP variability > 18.8	General Japanese subjects (1542)	≥40	8.5	Age, sex, smoking, diabetes, use of antihypertensive medication, obesity, prev. hyperlipidemia, CVD, 24-h SBP, DBP, and heart rate	CV mortality (67)	Cox model			
Daytime heart rate variability < 7.2							RR = 4.45		
Bruce stage 2 DBP	Framingham Study	20–69	20	Age, sex	CVD events (240)	Cox model	HR = 1.41; HR = 0.97	NR	[25]
Bruce stage 2 SBP							HR = 1.53		
Recovery DBP after exercise (3rd min)	Subjects (3045)								
Bruce stage 2 SBP > 180 mmHg (versus SBP ≤ 180 mmHg)	Asymptomatic patients (6578)	30–70	20	Age, sex, diabetes, LDL and HDL cholesterol, triglycerides, smoking, BMI, and family history	CVD death (385)	Cox model	HR = 1.96	Net reclassification improvement, SBP, 12%; DBP, 9.9%	[37]
Bruce stage 2 DBP > 90 mmHg (versus DBP ≤ 90 mmHg)							HR = 1.48		

BMI indicates body mass index; CoV: coefficient of variation; wDBP SD: weighted mean of daytime and nighttime DBP SD; ARV: average real variability; NR: not report; prev.: previous; LDL: low-density lipoprotein; HDL: high-density lipoprotein; CV: cardiovascular.

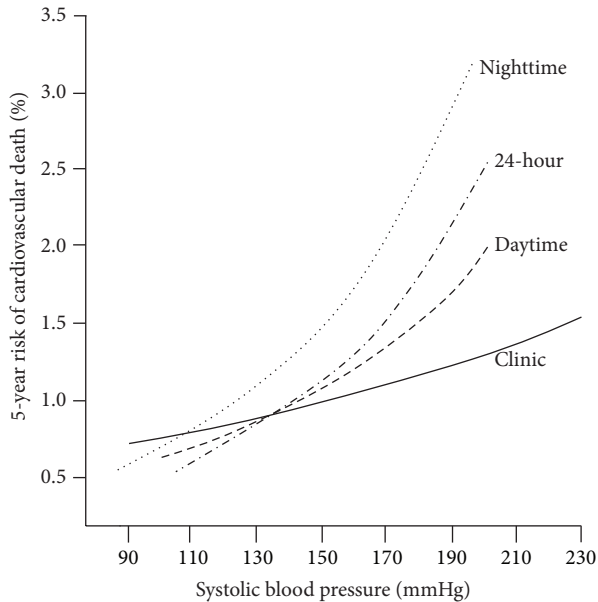


FIGURE 2: Adjusted 5-year risk of cardiovascular mortality versus systolic blood pressure captured by ambulatory blood pressure monitoring in different periods of the day. Reproduced from [24].

researchers, ABPM can be used for monitoring the variability pattern of BP, which can provide additional important information missed under office BP monitoring or common home monitoring, and is superior to clinic BP measurement in predicting mortality [24].

Different indexes including daytime BP mean, nighttime BP mean, 24 h BP mean, and night-to-day BP ratio in ABPM are indicated to consistently predict all CVD events. Figure 2 depicts an adjusted 5-year risk of cardiovascular death versus SBP captured by ABPM in the Dublin study [24]. It indicates that elevated nighttime BP mean is a better predictor of cardiovascular risk than 24 hour BP mean, daytime BP mean, or clinic BP, which is just the same as other common studies showed [43–46]. Another role of ABPM for the prediction of CVD events is that it could be used for evaluating the BPV during different periods of time. Short-term variability is estimated as the variation of reading-to-reading at baseline ABPM. The Ohasama study shows that the RR for daytime ambulatory systolic BPV > 18.8 is 2.69 ($P = 0.02$), with the BPV of 11.5–13.9 as the reference category, suggesting a strong predictive value for cardiovascular mortality [23]. Other cohort studies also prove that an increase in reading-to-reading BPV is only slightly associated with an increase in subsequent CVD events/complications (HRs are slightly larger than 1) [35, 36, 47]. Conversely, some studies find that the association loses in the presence of other well-known risk factors. The elusive results are in part because of the different sample and different BPV index adopted.

Other evidences indicate that an abnormal pattern of cyclic variation of BP (circadian or seasonal) is correlated well with an increased cardiovascular risk [29]. For example, excessive increase of BP just after rising in the morning, blunt, or nondipping of nocturnal BP (night-to-day BP

ratio ≥ 1 , sleep hypertension) is correlated with increased cardiovascular risk [28, 48, 49]. Such correlation could also be found in people with obstructive sleep apnea (OSA), whose BP rises at night while the risk of sudden cardiac death increases during sleep [31]. Besides, elevation of seasonal BP variation will increase cardiovascular risk. A study shows that the BP rises in the winter, while the frequency of acute MI increases by 53% in the winter [29].

Further study evaluates the different effects of taking antihypertension medications in different periods of time with the use of ABPM [50]. The results show that bedtime dosing would be better than morning dose in improving BP control including lowering the nocturnal BP, 24 h BP mean, or the morning BP surge. Intervention study also demonstrates that the progressive decrease in asleep BP mean captured by ABPM can efficiently reduce cardiovascular risk [35].

3.1.3. Stress Blood Pressure. Abnormal exercise BP response is demonstrated to be associated with an imbalance of autonomic nervous regulation, a future hypertension, and a future hypertensive left ventricular hypertrophy [51–53], suggesting a link to a high risk for the development of CVD. Though exaggerated exercise BP response and attenuated BP recovery are demonstrated to show prognostic information in identifying cardiovascular risk, even in normotensive individuals [25, 37, 54]. The results of the prognostic value are still controversial [25, 37]. That depends in part on the stage when BP is measured in the exercise and different exercise BP indexes adopted [37].

Two important studies (as shown in Table 1) report that submaximal BP during exercise is greater than maximal BP in predicting the risk of CVD death [25, 37]. One study, the Framingham study, shows that DBP during stage 2 of the Bruce protocol and recovery rather than SBP predict incident CVD when adjusted for resting BP [25]. The other study shows that Bruce stage 2 BP (submaximal exercise BP) $> 180/90$ mm Hg identifies normotensive individuals at higher risk of CVD death, independent of rest BP [37].

3.2. Electrocardiograph (ECG). Abnormalities on ECG reflect the electrical instability of the myocardium; therefore ECG can be used for screening vulnerable myocardium, which may lead to acute myocardial infarction [19]. Compared to conventional risk factors corresponding to long-term risk, ECG abnormalities are better for predicting short-term risk [55]. Quantitative measures assessed from resting ECG, ambulatory ECG, and stress ECG have been reported for predicting subsequent CVD events and mortality. At the present epidemiological studies, ECG abnormalities are widely evaluated with the use of Minnesota Code (MC) or Novacode (NC) [56].

3.2.1. Resting ECG. Abnormal ECGs relating to heart rate, conduction, left ventricular mass, or repolarization are shown to link to cardiovascular risk. The prognostic measures used include increased heart rate, left ventricular hypertrophy (LVH) [57], ST segment depression [58], negative T wave [58], pathological Q wave [56], left bundle branch blocks

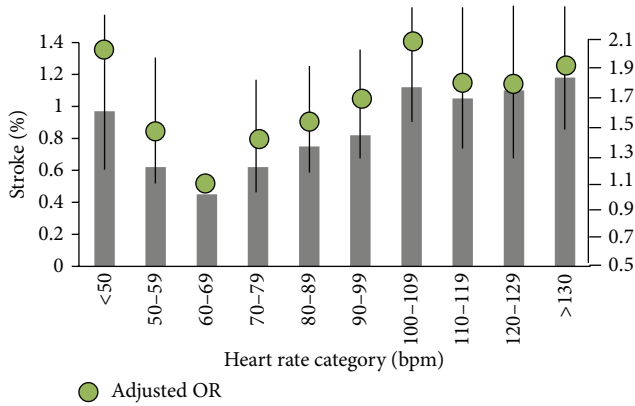


FIGURE 3: The risk of stroke versus heart rate groups. The heart rate group of 60–69 bpm is used as the reference category. Reproduced from [65].

(LBBB), arrhythmias (e.g., atrial fibrillation), QRS duration [59], and QT interval prolongation [60]. Some studies have tried to investigate pooled categories by combining some of the abnormalities above for improving the prognostic value. The pool categories used include major and minor abnormalities [61], ECG strain pattern [62, 63], and ischemic ECG findings (Minnesota codes I3, IV1–3, VI–3, or VIII) [64].

Large prospective cohort studies including the CRUSADE [65] and INVEST [66] show that the relationship between resting heart rate and adverse cardiovascular outcomes follows a “J-shaped” curve. Figure 3 depicts the relationship between the risk of stroke and heart rate groups in 135164 patients with acute coronary syndromes [65]. The risk of stroke increases with heart rate below or above the lowest point of 60–69 bpm. Other studies also show that increased resting heart rate can be used as a strong, graded, and independent risk factor for predicting incident CVD, especially for the sudden death from MI [67, 68]. Further cohort trials including the BEAUTIFUL and SHIFT studies prove that heart rate reduction benefiting from beta-blockers and other heart-rate lowering drugs is associated with a reduction of mortality in patients with coronary artery disease [69–71]. The possible pathophysiological mechanisms for the effects of elevated rest heart rate include the direct detriment on the progression of coronary atherosclerosis, on the occurrence of MI and ventricular arrhythmias, and on the left ventricular function [69]. A faster heart rate will necessarily impose more shear stress than a slow one [67] thus increases the likelihood of disruption of preexisting atherosclerotic plaque [72], which may lead to the occurrence of acute coronary artery disease.

ECG LVH may imply severe hypertension, which is related to elevated cardiovascular risk [73]. Numerous prospective cohort studies, including the Framingham study and the LIFE study, prove the value of LVH diagnosed by ECG criteria for predicting cardiovascular morbidity and mortality in hypertensive patients [57, 74, 75]. The predictive value is particularly great when repolarization abnormalities (i.e., ST depression and negative T wave) are present [62, 63]. Antihypertensive treatment that can induce the regression of ECG

LVH will reduce the risk of CVD events, independent of how much the BP is lowered [57, 74]. However, ECG is insensitive when used alone for screening LVH; the criteria for diagnosis of LVH are different [57]. Magnetic resonance imaging (MRI) is used as a standard for left ventricular mass measurement [76], while other techniques like echocardiography can also be used for the diagnosis of LVH [57].

ST segment depression and negative T waves, reflecting repolarization abnormalities, are markers of ischemic diseases. ST depression, isolated T wave abnormalities, and combined ST-T change are indicated to be independent predictors for cardiovascular death in substantial epidemiological data [56, 58, 77, 78]. Joint occurrence of ST-T change in combination with ECG LVH is the ECG abnormality with the greatest prognostic information for the future cardiac incidents [62].

Q-wave abnormality indicates myocardial tissue damage. It is usually used as a marker for identifying unrecognized or “silent” cardiac disease (e.g., unrecognized MI) [55]. Evidences from clinical studies indicate that both Q-wave alone and unrecognized MI diagnosed by ECG criteria based on Q-wave show the value for predicting the risk of mortality, heart failure, or stroke [56, 79, 80].

Composite variables such as major and minor abnormalities are used for the prediction of CVD events and mortality in asymptomatic persons [61]. The Women’s Health Initiative clinical trial including 14749 postmenopausal asymptomatic women shows that the addition of ECG findings to the FRS increased AUC from 0.69 to 0.74, which indicates an improvement of the risk discrimination [61].

3.2.2. Ambulatory ECG. The prognostic values of ambulatory heart rate parameters including increased daytime “night-time” 24 h heart rate, increased night-to-day heart rate ratio (heart rate nondipping), and decreased heart rate variability (HRV) are recently studied. A cohort study with 6928 subjects and with a 9.6-year followup shows that nighttime heart rate predicts cardiovascular mortality (HR = 1.15) night-to-day heart rate ratio predicts cardiac (HR = 1.23) and coronary (HR = 1.17) outcomes, while 24 h and daytime heart rate provide little prediction value for the identification of cardiovascular risk (HRs are slightly greater or less than 1.0) [73]. Heart rate variability (HRV) is affected by both vagal and sympathetic modulation of the sinus node. Diminished HRV reflects a decreased vagal activity, which increases the risk of death [81]. In a clinical study, reduced HRV measured in standard deviation of normal-to-normal intervals (SDNN) or low-frequency power (LF) is shown to be independent predictors of mortality after myocardial infarction or heart failure [82]. The Ohasama study shows that the RR for daytime HRV < 7.2 is 4.45 ($P = 0.003$), with the HRV > 14.0 as the reference category, suggesting a strong predictive value for identifying cardiovascular mortality [23]. Another study shows that the impaired heart rate deceleration capacity is a powerful predictor of mortality in postinfarction cohort, with a better AUC (0.74) than SDNN (0.64) [81]. However, conventional HRV indices lose predictive power in patients with MI, who have treatment with betablocks and revascularization [82]. In

summary, the prediction value of ambulatory heart rate now remains low and somewhat controversial.

3.2.3. Stress ECG. The stress ECG measures, including ST-segment deviation, failure heart rate increased, low heart rate recovery, and exercise-induced abnormalities (e.g., ventricular ectopy), show independent predictive value for identifying cardiovascular risk, even in patients with clinically normal resting electrocardiograms [20, 83–85].

Descending ST-segment during exercise is used for assessment of ischemia [86]. Exercise-induced ST-segment depression ≥ 1.0 mm of horizontal or down-sloping ST-segment depression at 80 ms after the J point is considered to be abnormal and is shown to be associated with sudden cardiac death and all-cause mortality [83, 87]. However, most of the adjusted HRs are only a little more than 1. The isolated ST-segmentation loses the prognostic value in asymptomatic women [84].

Heart rate responses to exercise reflect the function of autonomic nervous system and offer predictive value for major CVD and total death [20]. Failure of the heart rate to rise appropriately during exercise (termed chronotropic incompetence) reflects a “blunted” sympathetic reaction [20, 86]. Abnormal chronotropic index ≤ 0.80 , not achieving target heart rate, and exercise-induced heart rate increased < 89 bpm are shown to be independently predictive of MI, CHD death, and all-cause mortality in large cohort studies [84, 86, 88]. By contrast, reduced fall of the heart rate appropriately after exercise (termed reduced heart rate recovery) reflects an increased sympathetic activity or lack of vagal activity [20]. Reduced heart rate recovery with different cut-off values (e.g., < 12 , 18, 22, or 25 bpm after 1 min, < 22 or 42 bpm after 2 min, and < 50 after 3 min) is proved to provide additional, independent prognostic information of mortality [84, 88, 89]. A study shows that chronotropic incompetence (with HR of 2.8) is a stronger predictor of cardiovascular death than heart rate recovery (with HR of 2.0) [90]. In summary, heart rate recovery is limited by the variable recovery protocols and variable criteria for abnormality. It needs a further refinement before being used in making clinical decisions.

Quantitative measures of exercise-induced abnormalities, including higher heart rate, more leftward QRS axis, longer QT interval, and frequent ventricular ectopy in recovery, are shown to provide modest additional prognostic value [83].

Another non-ECG measure in the stress test, reduced exercise capacity, measured in metabolic equivalents (METs) or exercise duration, is proved to be one of the strongest predictors of cardiac and all-cause mortality among both healthy persons and those with CVD [91, 92].

Composite variables by synthesizing the measures above are used for predicting cardiovascular risk. For example, a composite ECG score by the combination of heart rate, conduction, left ventricular mass, and repolarization information in exercise ECG is adopted for improving the discrimination (C index increases 0.04) and the reclassification of risk of mortality [83]. Duke treadmill score (DTS) by the combination of exercise capacity, ST-segment deviation,

and exercise-induced angina pectoris is used for the posttest of risk stratification [93]. Another nomogram-illustrated model, which takes account of additional demographics (age, sex), simple risk factors (smoking, hypertension, and diabetes), and exercise test predictors (heart rate recovery and stress-related ventricular ectopy), is demonstrated to be better than DTS at risk discrimination (C index, 0.83 versus 0.73) [20, 89]. More details can be seen in Table 2.

3.3. Arterial Stiffness. Arterial stiffness is a consequence of arteriosclerosis, which integrates the effects of genetic background and long-term cumulative damage of cardiovascular risk factors in the arteries [20, 26, 94]. On the other hand, the increased arterial stiffness will lead to increased pulsatile component of BP, which is a valuable factor in modulating atherosclerosis progression and atherosclerotic plaque instability and thereby leading to acute coronary syndromes and other vascular complications [94]. Commonly applied methods for measuring arterial stiffness in epidemiological studies conclude aortic pulse wave velocity (PWV) and pulse wave analysis [95].

3.3.1. Aortic PWV. Aortic PWV is defined as the speed of travel of the aortic pulse wave, which directly influences the regional blood flow field around the plaque. It is calculated as the distance between two selected sites divided by pulse transit time [26]. The velocity of pulse wave propagation turns to be fast when the arteries become stiff. Thus, PWV reflects the arterial stiffness [20]. Measuring aortic PWV from the carotid to the femoral artery (cfPWV) was regarded as the clinical gold standard for assessing aortic stiffness [26]. However, the clinical application of cfPWV is limited by complicated measurement and the need to expose the privacy region in patients. Brachial-ankle pulse wave velocity (baPWV) is shown to be significantly correlated to cfPWV and is widely used in Asia for its convenience measurement [96].

Studies including a meta-analysis of 17 longitudinal studies analyze the increased aortic PWV as a strong independent predictor of the risk of CVD events [26, 97]. The risk of subjects with high aortic PWV is almost twice compared with those with lower aortic PWV (the cut-off values for dividing the high versus low stiffness groups are different from 8.2 to 17.7 m/s in different studies) [26]. It is increasingly used in clinical practice [98]. When PWV is added to standard risk factor models, the discrimination slope increases from 7.8 to 8.5 in Framingham study [99], while in Rotterdam study, the area under ROC curve improves from 0.70 to 0.72 [100].

3.3.2. Pulse Wave Analysis. As shown in Figure 4, central BP waveform is a sum of a forward traveling wave, generated by ventricular ejection, and a reflected wave coming back from the periphery [94]. Augmentation pressure (ΔP) is calculated as the SBP (the peak of the observed wave) minus the peak of the forward waveform. Thus, augmentation pressure represents the additional SBP due to the wave reflection [94]. Increased PWV due to increased arterial stiffness would lead to the increased overlap between forward and backward

TABLE 2: Sample of cohort studies reporting the independent predictive values of stress ECG measures.

Markers	Population characteristics (no.)	Age (y) at entry	Followup (y)	Covariates	End events (no.)	Model based	Prognostic value	Discrimination, calibration, and reclassification	Reference
Chronotropic response < 89 bpm heart rate recovery < 25 bpm	Men in Paris civil service (5713)	42–53	23	Non	Sudden death from MI (81)	Cox model	RR = 6.18 RR = 2.20	NR NR	[88]
ECG score (75th versus 25th percentile)	Patients without known CV disease (18964)	51 (mean)	10.7	Age, sex, smoking, diabetes, hypertension, and so forth.	All-cause mortality (1585)	Cox model	HR = 1.36	C index = 0.84, increased by 0.04 compared with established risk factors	[83]
Duke treadmill score nomogram-illustrated model	Patients with suspected CAD and normal ECG (33268)	52	6.2	Non	All-cause mortality (1619)	nomogram-illustrated model	NR NR	C index = 0.73 C index = 0.83	[89]

NR: not report; CAD: coronary artery disease; CV: cardiovascular.

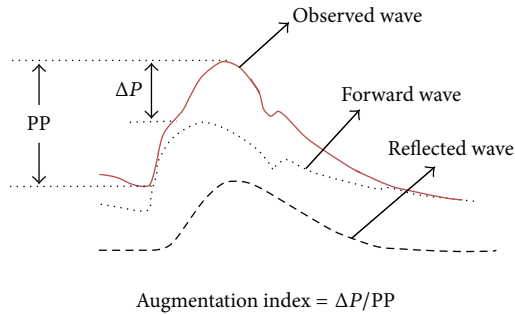


FIGURE 4: A central blood pressure waveform which contains a forward and a backward (reflected) components. PP indicates pulse pressure. Reproduced from [94, 95].

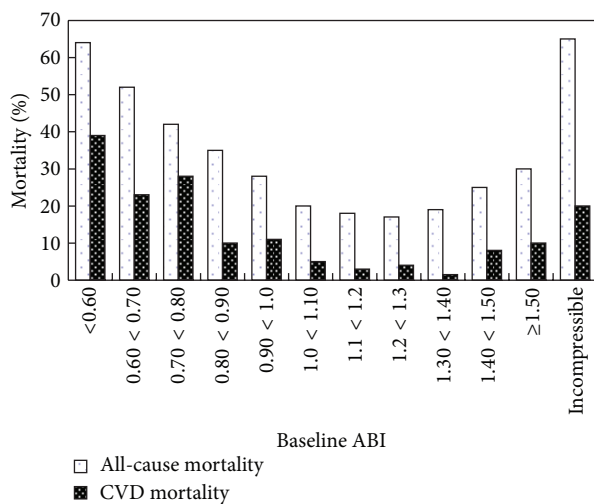


FIGURE 5: All-cause and CVD mortality according to ankle-brachial index (ABI) groups. Reproduced from [27].

wave, which would enhance the augmentation pressure and subsequently central SBP and pulse pressure [94]. Central BP, pulse pressure, and aortic augmentation index (AIx) therefore indirectly reflect the arterial stiffness. The pulse pressure is calculated as SBP minus DBP, while the AIx is expressed as ΔP to a proportion of the central pulse pressure, PP ($\Delta P/PP$), as shown in Figure 4 [94, 95].

There are researches demonstrating that central BP is superior to brachial BP and brachial PP in the prediction of CVD events in an unselected geriatric population and hypertensive patients [101–103]. The predictive power is stronger in the younger group than in the older group, since aging will lessen pulse pressure amplification [102]. Pulse pressure is reported to be a weak predictor [33]. In the geriatric population ≥ 65 years, brachial PP loses its predictive power while central PP remains a valid predictor of CVD events [101]. AIx predicts adverse cardiovascular events in patients with established coronary artery disease [104], predicts CHD in men undergoing angiography [105], and predicts mortality in patients with end-stage renal failure [106]. However, it yields conflicting results in patients with systolic heart failure. In these kinds of people, patients with

lower values of central PP or AIx have more advanced systolic dysfunction [107]. Besides, AIx is not a reliable measure of arterial stiffness in people with diabetes [108]. A recent study reports that reflected wave magnitude, but not AIx, predicts cardiovascular death independent of cfPWV [109]. Other measures including ambulatory arterial stiffness index (AASI) [110] and carotid pulse pressure (versus brachial pulse pressure) [101] are studied within general populations.

As described above, reflective pulse wave analysis and PWV are commonly used for measuring arterial stiffness. However, they are different in the following: (1) wave reflection analysis is sensitive to pulse wave velocity, the wave reflection site, the duration and pattern of ventricular ejection, changes in heart rate, and antihypertensive drugs, while PWV reflects the inherent stiffness of the arterial wall [95]; (2) AIx is considered to be a more sensitive marker in younger individuals, while aortic PWV is a better predictor in older individuals [111]; (3) aortic PWV may be more useful for measuring long-term changes in arterial stiffness, whereas wave reflection analysis reflects short-term changes, for example, in the condition of therapeutic interventions [95].

In therapeutic trials, destiffening strategies with the use of antihypertrophic drugs, which have the benefit of reducing wave reflections and subsequently lowering the central SBP and PP, show significant reduction of cardiovascular risk [94]. For example, diuretic and calcium antagonist which with the effect of lowering central SBP and PP is better than classic betablocker which reduces the peripheral SBP only in lowering cardiovascular risk [94]. A recent study indicates that vasodilatory antihypertensives have the effect of reducing the central BP independently of the peripheral BP [103].

3.4. Ankle-Brachial Index. Ankle-brachial blood pressure index (ABI) is defined as the ratio of systolic pressure at the ankle to that in the arm. It is another parameter for evaluating structural and functional change in the vascular and is used for measuring peripheral vascular disease. An abnormal low ABI (≤ 0.90) indicates the presence of peripheral artery disease, which is defined as $>50\%$ stenosis, while an abnormal high ABI (>1.40) indicates artery calcification. Mortality risk increases both at abnormally low or high ABI. Slightly abnormal values (0.91 to 1.10) also have a graded association with CVD risk [20, 112].

Numerous epidemiological studies prove that an abnormal ABI is associated with an increased cardiovascular risk [20, 113]. Figure 5 shows an association between mortality and ABI groups in the Strong Heart study, which includes 4393 individuals aged 45–74 and followup of 8.3 ± 2.2 years [27]. We can see that low ABI (≤ 0.90) and high ABI (>1.40) significantly improve the mortality risk. A metastudy by following up of 24955 men and 23339 women shows that, for a low ABI (≤ 0.9) compared with a normal ABI (1.11 to 1.40), the HR for 10-year cardiovascular mortality is 4.2 for men and 3.5 for women. When adjusted for FRS, the values are 2.9 and 3.0, respectively, indicating that, by adding the abnormal ABI as a risk factor, the risk prediction extends beyond that of the

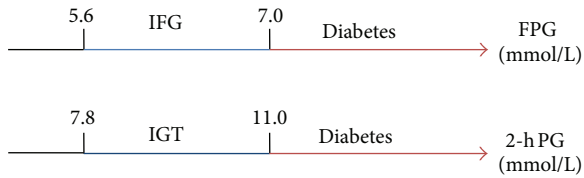


FIGURE 6: Categories for prediabetes and diabetes mellitus FPG, fasting plasma glucose. 2 h PG, 2 hour plasma glucose in the oral glucose tolerance test. IFG: impaired fasting glucose. IGT: impaired glucose tolerance.

FRS [113]. The MESA study shows that the AUC improved by the addition of ABI to the FRS is 0.036 [114].

3.5. Blood Glucose. Elevated plasma glucose may cause several conditions that relate to the development of cardiovascular complications, such as thrombophilic condition, endothelial dysfunction, and enhanced platelet adhesion [21]. The relationship between glucose level and cardiovascular incident is graded and independent [115]. Cut-off values for defining glucose abnormalities are modified recently with regard to the risk of cardiovascular [116]. According to the latest 2012 American Diabetes Association (ADA) criteria, categories for glucose abnormalities classification are based on fasting plasma glucose (FPG) and 2 h plasma glucose (2 h PG) in the oral glucose tolerance test, as shown in Figure 6 [116]. Individuals whose FPG levels are of 5.6 mmol/L to 7.0 mmol/L are thought to have impaired fasting glucose (IFG), while people with 2 h PG values of 7.8 mmol/L to 11.0 mmol/L are thought to have impaired glucose tolerance (IGT). And those with either FPG of >7.0 mmol/L or 2 h PG of >11.0 mmol/L are thought to have diabetes.

Hyperglycemia for cardiovascular risk prediction is widely investigated in cohort studies. Diabetes is proven to be established factors in predicting CVD risk and is widely applied in clinical practice. Besides, cohort studies including the Framingham Offspring Study and a meta-analysis suggest that milder glucose abnormalities such as IFG or IGT are also independent risk factors for predicting CVD though the predictive values are small (HRs are slightly larger than 1), and the risk increases mostly in those with combined IFG and IGT [115, 117, 118]. Some data show that 2 h PG is a better risk predictor than IFG [118].

4. Initial Studies on Physiological Parameters for Near-Term CVD Prediction

Researchers are trying to further identify the individuals who are at high risk of developing near-term CVD events and are in most urgent need of intervention [119]. To date, tools to predict near-term cardiovascular risk after acute coronary syndromes (ACS) are already available, such as the 7-point Thrombolysis in Myocardial Infarction (TIMI) risk score (for forecasting 30-day mortality) and the Global Registry of Acute Coronary Events (GRACE) risk score (for assessing the risk of six-month postdischarge death) [119]. However, there is not an algorithm that can be used for forecasting near-term

risk in asymptomatic populations. With the addition of new sensitive risk factors that directly relate to the pathological process of CVD may promote the development of near-term prediction strategies.

58 international clinical experts from different groups have shown that vulnerable patients characterized as vulnerable plaques (prone to thrombotic complications and rapid progression), vulnerable blood (prone to thrombosis), and vulnerable myocardium (prone to fatal arrhythmia) are those people at high risk of developing acute cardiovascular events [2]. Some cardiovascular parameters captured by physiological tests have been proved to be directly related to the process of atherothrombotic plaque rupture, blood vulnerability, and myocardial susceptibility. As mentioned before, blood pressure, arterial stiffness, ABI, and blood glucose reflect the regional blood flow field conditions (blood pressure, blood velocity, and blood viscosity) of the blood vessels, which are responsible for triggering plaque rupture and consequence progression of CVD. ECG reflects the vulnerable property of the myocardium, whose abnormalities often lead to acute myocardial infarction. Therefore, physiological parameters are those sensitive risk factors that directly relate to the pathological process of CVD.

There are several prospective cohort studies showing the evidences of using physiological parameters as risk factors for predicting near-term risk of CVD events. The Cardiovascular Health study shows that diabetes, SBP, atrial fibrillation (AF), and ECG-defined LVH are associated with short-term risk of stroke (with followup of 3.31 years) in older adults [120]. ABI is shown to be highly associated with one-year risk of cardiovascular death in a cohort study with 6880 old patients (OR adjusted by age and sex was 3.7) [121]. Aortic augmentation pressure, a measure of arterial stiffness, is shown to be significantly predictive of adverse cardiovascular outcomes in 297 patients with coronary artery during 1.2–3.3 years of followup [104]. Increased arterial wave reflection, another measure of arterial stiffness, also proves to be highly associated with severe short-term CVD events in 262 patients undergoing percutaneous coronary intervention during 2-year followup [122].

Therefore, in addition of emerging factors extracted from physiological signals may be benefit for the assessment of near-term CVD risk.

5. Developments in the Medical Devices for Physiological Parameter Test

In daily clinical practice, physiological parameters of the heart and arteries are measured from the body surface by noninvasive or mini-invasive tests. For instance, resting ECG is captured with the use of electrodes that adhere directly to the surface of the skin. Ambulatory ECG is collected with the use of a portable Holter [20]. Resting BP is examined by clinical examination or home visit using a mercury sphygmomanometer or a validated digital automatic BP monitor with placing a cuff on the brachial artery surface [40]. Ambulatory BP monitoring is performed using an ambulatory BP monitor with placing a cuff on the brachial artery surface [28]. PWV

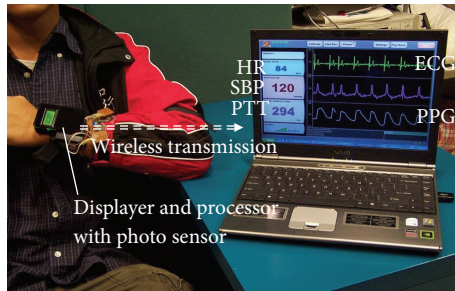


FIGURE 7: A health shirt designed in our research center for capturing multiparameters including ECG, PPG, and cuffless BP. Reproduced from [135].

is commonly collected using an applanation tonometry [123] but can also be measured by Doppler probes [109] or MRI [124]. Noninvasive arterial waveform measurement is generally obtained by placing an applanation tonometry on the peripheral artery surface (carotid or radial artery). For ABI monitoring, arm BP and ankle BP (posterior tibial artery) are commonly collected by Doppler. Blood glucose measurement is mini-invasive. Laboratory blood glucose value is collected using biochemical analyzer. In electrochemical meters, the concentration of glucose in the blood specimen is estimated by detecting the charge generated by the oxidation reaction using enzyme electrodes. When immediate blood glucose monitoring is performed out of the laboratory, blood sample is collected by piercing the skin (typically, on the finger) with a needle then applying the blood to a disposable glucose reagent strip. Compared to other modalities of tests for early CVD prediction, such as imaging [15], genetic test [16], and biomarker assay [17], noninvasive monitoring of physiological parameters have the advantages of ease of use, simple procedure, small cost, and low side effects.

In the past decades, novel unobtrusive monitoring methods have been invented to acquire physiological signals and parameters without disturbing the subject's daily life or even without awareness, such as ECG, heart rate, BP, and blood glucose. For ECG monitoring, noncontact sensors based on capacitively coupled principle and embedded in furniture, clothing, or wearable accessories provide an avenue for unobtrusive sensing of ECG [125]. The heart rate can be calculated indirectly from signals that can be detected unobtrusively, including ECG, photoplethysmography (PPG), and video images of a subject's face [126]. It can also be detected directly using unobtrusive sensors. For example, it can be detected remotely by microwave radar sensors based on the Doppler effect [127]. For BP monitoring, advanced technologies are focusing on developing methods that can be used for capturing BP continuously and noninvasively without using a cuff [125]. Radial pulse waveform acquired by arterial tonometry [128] and pulse transit time (PTT) measured from ECG and PPG signals [129, 130] provide two promising techniques for continuous and cuffless BP monitoring. Technologies advanced in blood glucose detection concentrate on developing needle-free, transcutaneous methods for noninvasive and continuous measurements. Potential technologies include impedance spectroscopy, reverse

iontophoresis, enzyme-based direct electron, transfer electrophoresis, near infrared spectroscopy, and photoacoustic spectroscopy [131, 132]. Some of the technologies have been integrated into wrist-worn devices, such as GlucoWatch biographer, for unobtrusive measurement [133]. In addition, there are no direct evidences showing the measurement of arterial stiffness and ABI using unobtrusive devices. Radial pulse waveform acquired by arterial tonometry suggests the potential possibility of measuring arterial stiffness through reflective pulse wave analysis. A study also introduces a novel potential method for assessing arterial stiffness based on finger height and PTT [134]. And the emergence of cuffless BP measurement may also make assessing ABI with unobtrusive devices become possible.

The captured physiological health information from unobtrusive instruments can then be transmitted to a remote clinical center using wireless communication technology. In this way, the patient's CVD status can be remotely monitored in an out-of-hospital setting in real-time. Figure 7 provides an example of a health shirt designed in our research center for unobtrusively multiparameters monitoring including ECG, PPG, and cuffless BP [135]. In this system, the garment is made from e-textiles for ECG monitoring, and PPG detector is embedded in the "watch-like" device. BP is estimated based on PTT which is measured from ECG and PPG signals. And all the health information is transmitted to a distanced control center by wireless transmission.

6. Computer Modeling for the Management of CVD

CVD is an extremely heterogeneous disease, with multiple forms of phenotypes and disease mechanisms. Increased technologies have provided the risk markers of the CVD and the information of cardiovascular system in multimodalities and multiscales. High-resolution imaging can supply the information of structure, component, and metabolism. Genetic test and biomarker assay provide the information at cellular, molecular, and protein levels. Physiological test reflects the hemodynamics and electrophysiology of the cardiovascular system. However, by means of current measurements of cardiac function are no longer specific enough to identify exactly the type of CVD a patient may suffer. Computer modeling supplies an opportunity for the fusion of the multiscale information through an unified platform for the understanding of CVD progress comprehensively and precisely and even for predicting the CVDs. It has been shown recently that computational models integrating multiscale health information can provide a quantitative assessment of the physiological and pathological activities of organism from simulation environment. For example, the Virtual Physiological Rat (VRP) Project develops computer models that integrate disparate data of genomic, anatomic, physiological, and so forth to explain and predict specific functions and diseases [136]. A multiscale cardiac functional modeling platform developed by the Heart Physiome Project can be used for demonstrating the mechanisms that underlie cardiac arrhythmia and fibrillation [137, 138]. The euHeart

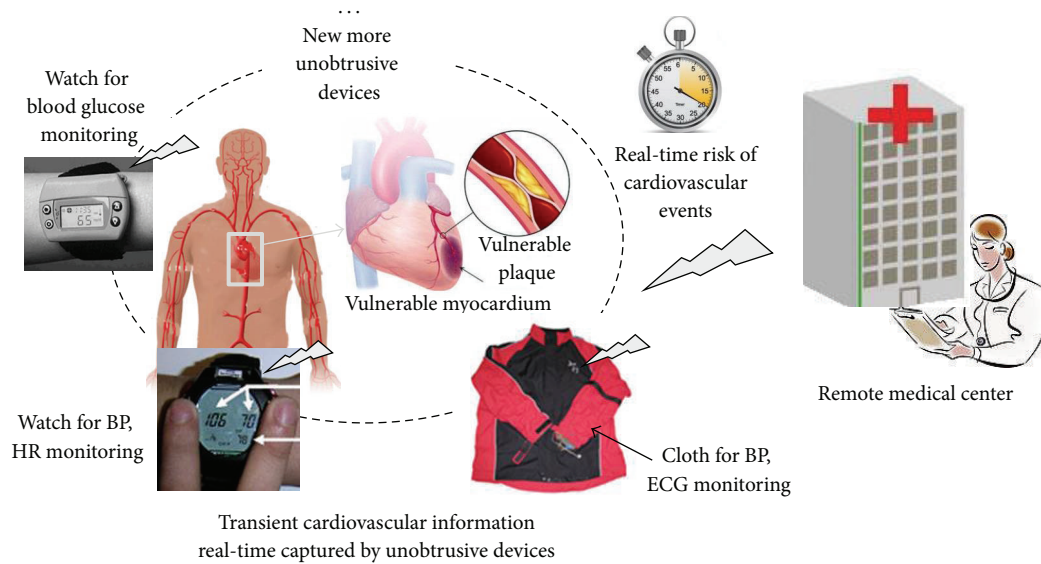


FIGURE 8: A blue print of real-time prediction of sudden cardiovascular events by physiological test using unobtrusive medical devices. The devices in the print are from [125, 133]. BP: blood pressure; HR: heart rate.

Project develops patient-specific cardiovascular modeling frameworks for personalized and integrated cardiac care [139]. Wang et al. develops an integrated model based on tagged MRI data for better understanding of the underlying passive ventricular mechanics that adapt to pathophysiological changes [140].

7. Discussion and Conclusion

After review, established and potential physiological risk factors used for the early CVD prediction are systematically summarized in Table 3. Predictive power, significance, and limitations are also presented for each of the predictors in the table. Currently, most of the studies assess the prognostic values of physiological risk factors by reporting adjusted HR, OR, or RR with CIs and *P* values. The results show that measures extracted from blood pressure, ECG, arterial stiffness, ABI, and blood glucose are statistically associated with adverse CVD events. However, only a small number of studies further report other more rigorous metrics such as calibration, discrimination, and reclassification for assessing the performance of a risk prediction model with the inclusion of the new markers. There are also limited studies reporting the effects on CVD events reduction by doing management of these factors. Thus, more studies are needed to provide more comprehensive measures before these risk factors to be considered useful for providing incremental predictive information over a standard risk assessment profile. It is noteworthy that the new cardiovascular risk factors should be validated before they are adopted in standard clinical care according to the following phases [32]: initial proof of the notion, prospective verification in independent individuals, documentation of additional information when added to established risk factors, evaluation of effects on patient

treatment and outcomes, and cost-effectiveness, which are proposed by the American Heart Association.

Emerging factors captured by means of continuous or long-term monitoring, such as visit-to-visit blood pressure variability, elevated nighttime blood pressure, elevated nighttime heart rate, morning surge of blood pressure and heart rate, chronotropic incompetence, and reduced heart rate recovery, are proved to be with powerful prediction. This indicates the prospective applications of unobtrusive medical devices in the field of CVD prediction and management. First, with the use of unobtrusive methods for the continuous, real-time, and long-term collection of the physiological signals and parameters, critical risk markers can probably be extracted for predicting plaque rupture and acute CVD events. Second, continuous and long-term collection of the fluctuating health information before the near events will help unravel the dynamic mechanism of the CVD progression. Third, unobtrusive devices are suitable for on-site detection in out-of-hospital settings in real-time, which will allow taking preemptive treatments in response to the acute CVD events. However, as mentioned before, BP, ECG, and blood glucose now can be monitored unobtrusively, and arterial stiffness and ABI have also shown potential to be monitored in an unobtrusive way. Besides, techniques such as motion artifact elimination are needed to be overcome to acquire high quality signals for reaching unobtrusive monitoring in real life.

Current CVD prediction models are based on statistical analysis of populations and can hardly provide a basis for personalized prognosis because of the individual difference. Advancing technologies, such as high resolution imaging [15], genetic test [16], biomarker assay [17], and physiological monitoring, now can provide multiscale health information of the heart, spinning from gene, protein, cell, issue, organ, to the system levels. Computational models

TABLE 3: Established and potential physiological risk factors used for prediction of cardiovascular diseases.

Physiological parameters	Predictors	Significance and limitations	Predictive power	
BP	Resting BP	Usual BP Visit-to-visit BPV Maximum BP	Measures the brachial artery cuff blood pressure. Strong risk factors for CV prediction. Cuffless and continuous monitoring are under improvement.	+++++
	ABPM	Daytime BP mean Nighttime BP 24-h mean BP Night-to-day BP ratio Night BPV Day BPV 24-hour BPV		
Stress BP	Stress BP	Sub maximal BP Maximal BP Recovery BP after exercise	Provide additional prognostic information in CV prediction beyond normal rest blood pressure. The results remain controversial depending on different exercise BP indexes adopted.	++ + ++
	ECG	Resting heart rate LVH ST segment depression Negative T wave Pathological Q-wave LBBB Arrhythmias Prolonged QRS duration QT interval prolongation Major and minor abnormalities ECG strain pattern Ischemic ECG findings Composite ECG score	Measures the electrical activity of the heart and relates to short-term risk of CVD. Resting heart rate is a strong, graded, and independent risk factor. Repolarization abnormalities in combination with LVH show great prediction value. Noncontact wireless ECG sensors based on capacitively coupled principle are becoming washable and can be integrated in clothing or wearable accessories for unobtrusive monitoring.	++++
Ambulatory ECG	Ambulatory ECG	Nighttime heart rate Night-to-day heart rate ratio HRV	The prediction value of ambulatory heart rate remains low and somewhat controversial. HRV measures the vagal and sympathetic modulation of the sinus node.	++ +
	Stress ECG	Exercise-induced ST-segment depression Chronotropic incompetence Reduced heart rate recovery Exercise-induced abnormalities Composite ECG score Exercise capacity Duke treadmill score Nomogram-illustrated model	Provide additional prognostic information beyond normal resting ECG. Chronotropic incompetence, reduced heart rate recovery, and exercise capacity are proved to be strong predictors. The predictive values of others remain low. Heart rate recovery is still limited by the variable recovery protocols and variable criteria for abnormality.	+++
Arterial Stiffness	Aortic PWV	cfPWV baPWV	Clinical gold standard for assessing aortic stiffness. Widely used in large scale trials for its convenience measurement.	+++ ++
	Pulse wave analysis	AIx Central SBP PP Reflected wave magnitude AASI	Offering wave reflection information. Indirect indicator of arterial stiffness.	++
Blood glucose	Blood glucose	Diabetes mellitus Impaired fasting glucose Impaired glucose tolerance Combined IFG & IGT	Strong, graded, and independent predictors. Technical advances in noninvasive and continuous glucose monitoring are under development.	++++ + ++ +++

TABLE 3: Continued.

Physiological parameters	Predictors	Significance and limitations	Predictive power
ABI	ABI < 0.9 ABI > 1.4	Indicating the presence of peripheral artery disease Indicating calcified arteries	++++ ++++

BP: blood pressure; CV: cardiovascular; ABPM: ambulatory blood pressure monitoring; BPV: blood pressure variability; ECG: electrocardiogram; LVH: left ventricular hypertrophy; CVD: cardiovascular disease; LBBB: left bundle branch blocks; HRV: heart rate variability; cfPWV: carotid femoral pulse wave velocity; baPWV: brachial-ankle pulse wave velocity; Aix: aortic augmentation index; SBP: systolic blood pressure; PP: pulse pressure; AASI: ambulatory arterial stiffness index; ABI: ankle-brachial blood pressure index; IFG: impaired fasting glucose; IGT: impaired glucose tolerance.

that integrate the multiscale health information provide a pathway for a patient-specific quantitative assessment of the physiological and pathological activities of the cardiovascular system from a simulation environment [141]. Therefore, a multiscale patient-specific model based on computer model technology and information fusion theory is prospected to be constructed for allowing the prediction of the cardiac mechanisms from observing signals. In this way, quantitative and personalized assessment of the risk of developing CVD events can be put into practice. In addition, the predictive value of the physiological parameters and the advancing unobtrusive technologies are used for real-time, on-site detection of the physiological parameters, indicating the possibility for real-time risk prediction of the acute CVD events. Figure 8 depicts a blue print of real-time prediction of sudden cardiovascular events by physiological tests using unobtrusive technologies and wireless communication technologies [125, 133].

In the future, a personalized quantitative risk assessment and real-time prediction model for sudden CVD events can be further studied and verified by constructing animal models to mimic the cardiovascular disease progression of plaque rupture, thrombosis, and adverse events, before applying to persons. It is of great importance to develop unobtrusive monitoring techniques to provide more accurate and quantifiable prognostic information for screening of vulnerable patients before the events occur. The application of unobtrusive technologies may be widened for detecting other risk factors that reflect the process of arteriosclerosis, such as developing microfluid chips for biomarker analysis.

Conflict of Interests

The authors declare that there is no financial relationship with any product, service, or company mentioned in this paper.

Acknowledgments

This work is supported in part by the National Basic Research Program 973 (no. 2010CB732606), the Guangdong Innovation Research Team Fund for Low-Cost Healthcare Technologies in China, the External Cooperation Program of the Chinese Academy of Sciences (no. GJHZ1212), the Key Lab for Health Informatics of Chinese Academy of Sciences, and the National Natural Science Foundation of China (nos. 81101120 and 61002002).

References

- [1] WHO, "Cardiovascular diseases (CVDs)," Tech. Rep., World Health Organization, Geneva, Switzerland, 2012.
- [2] M. Naghavi, P. Libby, E. Falk et al., "From vulnerable plaque to vulnerable patient: a call for new definitions and risk assessment strategies: part II," *Circulation*, vol. 108, no. 15, pp. 1772–1778, 2003.
- [3] J. Mackay, G. A. Mensah, S. Mendis, and K. Greenlund, "The atlas of heart disease and stroke," Tech. Rep., World Health Organization, Geneva, Switzerland, 2004.
- [4] R. B. D'Agostino Sr., R. S. Vasan, M. J. Pencina et al., "General cardiovascular risk profile for use in primary care: the framingham heart study," *Circulation*, vol. 117, no. 6, pp. 743–753, 2008.
- [5] S. M. Grundy, J. I. Cleeman, C. N. Merz et al., "Implications of recent clinical trials for the national cholesterol education program adult treatment panel III guidelines," *Circulation*, vol. 110, no. 2, pp. 227–239, 2004.
- [6] R. M. Conroy, K. Pyörälä, A. P. Fitzgerald et al., "Estimation of ten-year risk of fatal cardiovascular disease in Europe: the SCORE project," *European Heart Journal*, vol. 24, no. 11, pp. 987–1003, 2003.
- [7] G. Assmann, P. Cullen, and H. Schulte, "Simple scoring scheme for calculating the risk of acute coronary events based on the 10-year follow-up of the prospective cardiovascular münster (PROCAM) study," *Circulation*, vol. 105, no. 3, pp. 310–315, 2002.
- [8] J. Hippisley-Cox, C. Coupland, Y. Vinogradova, J. Robson, M. May, and P. Brindle, "Derivation and validation of QRISK, a new cardiovascular disease risk score for the United Kingdom: prospective open cohort study," *British Medical Journal*, vol. 335, no. 7611, pp. 136–141, 2007.
- [9] P. M. Ridker, N. P. Paynter, N. Rifai, J. M. Gaziano, and N. R. Cook, "C-reactive protein and parental history improve global cardiovascular risk prediction: the reynolds risk score for men," *Circulation*, vol. 118, no. 22, pp. 2243–2251, 2008.
- [10] P. M. Ridker, J. E. Buring, N. Rifai, and N. R. Cook, "Development and validation of improved algorithms for the assessment of global cardiovascular risk in women: the reynolds risk score," *Journal of the American Medical Association*, vol. 297, no. 6, pp. 611–619, 2007.
- [11] Y. Wu, X. Liu, X. Li et al., "Estimation of 10-year risk of fatal and nonfatal ischemic cardiovascular diseases in Chinese adults," *Circulation*, vol. 114, no. 21, pp. 2217–2225, 2006.
- [12] D. M. Lloyd-Jones, "Cardiovascular risk prediction: basic concepts, current status, and future directions," *Circulation*, vol. 121, no. 15, pp. 1768–1777, 2010.
- [13] S. C. Smith Jr., "Current and future directions of cardiovascular risk prediction," *American Journal of Cardiology*, vol. 97, 1, no. 2A, pp. 28A–32A, 2006.
- [14] K. M. Johnson and D. A. Dowe, "The detection of any coronary calcium outperforms framingham risk score as a first step in screening for coronary atherosclerosis," *American Journal of Roentgenology*, vol. 194, no. 5, pp. 1235–1243, 2010.
- [15] V. Fuster, F. Lois, and M. Franco, "Early identification of atherosclerotic disease by noninvasive imaging," *Nature Reviews Cardiology*, vol. 7, no. 6, pp. 327–333, 2010.
- [16] L. N. Pu, Z. Zhao, and Y. T. Zhang, "Investigation on cardiovascular risk prediction using genetic information," *IEEE Information Technology in Biomedicine*, vol. 16, no. 5, pp. 795–808, 2012.
- [17] D. Tousoulis, G. Hatzis, N. Papageorgiou et al., "Assessment of acute coronary syndromes: focus on novel biomarkers," *Current Medicinal Chemistry*, vol. 19, no. 16, pp. 2572–2587, 2012.
- [18] H. Lu, L. A. Cassis, and A. Daugherty, "Atherosclerosis and arterial blood pressure in mice," *Current Drug Targets*, vol. 8, no. 11, pp. 1181–1189, 2007.
- [19] M. Naghavi, P. Libby, E. Falk et al., "From vulnerable plaque to vulnerable patient: a call for new definitions and risk assessment strategies: part I," *Circulation*, vol. 108, no. 14, pp. 1664–1672, 2003.
- [20] P. Greenland, J. S. Alpert, G. A. Beller et al., "2010 ACCF/AHA guideline for assessment of cardiovascular risk in asymptomatic adults: a report of the American college of cardiology

- foundation/American heart association task force on practice guidelines," *Circulation*, vol. 122, no. 25, pp. e584–e636, 2010.
- [21] G. Paolisso, M. R. Rizzo, M. Barbieri, D. Manzella, E. Ragno, and D. Maugeri, "Cardiovascular risk in type 2 diabetics and pharmacological regulation of mealtime glucose excursions," *Diabetes and Metabolism*, vol. 29, no. 4, part 1, pp. 335–340, 2003.
- [22] G. Thrall, D. Lane, D. Carroll, and G. Y. H. Lip, "A systematic review of the prothrombotic effects of an acute change in posture: a possible mechanism underlying the morning excess in cardiovascular events?" *Chest*, vol. 132, no. 4, pp. 1337–1347, 2007.
- [23] M. Kikuya, A. Hozawa, T. Ohokubo et al., "Prognostic significance of blood pressure and heart rate variabilities: the ohasama study," *Hypertension*, vol. 36, no. 5, pp. 901–906, 2000.
- [24] E. Dolan, A. Stanton, L. Thijs et al., "Superiority of ambulatory over clinic blood pressure measurement in predicting mortality: the Dublin outcome study," *Hypertension*, vol. 46, no. 1, pp. 156–161, 2005.
- [25] G. D. Lewis, P. Gona, M. G. Larson et al., "Exercise blood pressure and the risk of incident cardiovascular disease (from the framingham heart study)," *American Journal of Cardiology*, vol. 101, no. 11, pp. 1614–1620, 2008.
- [26] C. Vlachopoulos, K. Aznaouridis, and C. Stefanadis, "Prediction of cardiovascular events and all-cause mortality with arterial stiffness. a systematic review and meta-analysis," *Journal of the American College of Cardiology*, vol. 55, no. 13, pp. 1318–1327, 2010.
- [27] H. E. Resnick, R. S. Lindsay, M. M. McDermott et al., "Relationship of high and low ankle brachial index to all-cause and cardiovascular disease mortality: the strong heart study," *Circulation*, vol. 109, no. 6, pp. 733–739, 2004.
- [28] T. Giles, "Relevance of blood pressure variation in the circadian onset of cardiovascular events," *Journal of Hypertension*, vol. 23, no. 1, pp. S35–S39, 2005.
- [29] M. S.-J. Rim, "Blood pressure variation and cardiovascular risks," *Korean Circulation Journal*, vol. 38, no. 3, pp. 131–134, 2008.
- [30] A. Halkin, A. Steinvil, R. Rosso, A. Adler, U. Rozovski, and S. Viskin, "Preventing sudden death of athletes with electrocardiographic screening: what is the absolute benefit and how much will it cost?" *Journal of the American College of Cardiology*, vol. 60, no. 22, pp. 2271–2276, 2012.
- [31] A. S. Gami, D. E. Howard, E. J. Olson, and V. K. Somers, "Day-night pattern of sudden death in obstructive sleep apnea," *The New England Journal of Medicine*, vol. 352, no. 12, pp. 1206–1279, 2005.
- [32] M. A. Hlatky, P. Greenland, D. K. Arnett et al., "Criteria for evaluation of novel markers of cardiovascular risk: a scientific statement from the American heart association," *Circulation*, vol. 119, no. 17, pp. 2408–2416, 2009.
- [33] K. Miura, H. Nakagawa, Y. Ohashi et al., "Four blood pressure indexes and the risk of stroke and myocardial infarction in Japanese men and women a meta-analysis of 16 cohort studies," *Circulation*, vol. 119, no. 14, pp. 1892–1898, 2009.
- [34] P. M. Rothwell, S. C. Howard, E. Dolan et al., "Prognostic significance of visit-to-visit variability, maximum systolic blood pressure, and episodic hypertension," *The Lancet*, vol. 375, no. 9718, pp. 895–905, 2010.
- [35] R. C. Hermida, D. E. Ayala, A. Mojón, and J. R. Fernández, "Decreasing sleep-time blood pressure determined by ambulatory monitoring reduces cardiovascular risk," *Journal of the American College of Cardiology*, vol. 58, no. 11, pp. 1165–1173, 2011.
- [36] G. Bilo, E. Dolan, E. O'Brien, and G. Parati, "Blood pressure variability as a predictor of cardiovascular mortality: results of Dublin outcome study: 4B. 01," *Journal of Hypertension*, vol. 28, article 209, 2010.
- [37] S. A. Weiss, R. S. Blumenthal, A. R. Sharrett, R. F. Redberg, and S. Mora, "Exercise blood pressure and future cardiovascular death in asymptomatic individuals," *Circulation*, vol. 121, no. 19, pp. 2109–2116, 2010.
- [38] S. Lewington, R. Clarke, N. Qizilbash, R. Peto, and R. Collins, "Age-specific relevance of usual blood pressure to vascular mortality: a meta-analysis of individual data for one million adults in 61 prospective studies," *The Lancet*, vol. 360, no. 9349, pp. 1903–1913, 2002.
- [39] P. M. Rothwell, S. C. Howard, E. Dolan et al., "Effects of β blockers and calcium-channel blockers on within-individual variability in blood pressure and risk of stroke," *The Lancet Neurology*, vol. 9, no. 5, pp. 469–480, 2010.
- [40] P. M. Rothwell, "Limitations of the usual blood-pressure hypothesis and importance of variability, instability, and episodic hypertension," *The Lancet*, vol. 375, no. 9718, pp. 938–948, 2010.
- [41] A. J. Webb, U. Fischer, Z. Mehta, and P. M. Rothwell, "Effects of antihypertensive-drug class on interindividual variation in blood pressure and risk of stroke: a systematic review and meta-analysis," *The Lancet*, vol. 375, no. 9718, pp. 906–915, 2010.
- [42] B. Carlberg and L. H. Lindholm, "Stroke and blood-pressure variation: new permutations on an old theme," *The Lancet*, vol. 375, no. 9718, pp. 867–869, 2010.
- [43] H.-Q. Fan, Y. Li, L. Thijs et al., "Prognostic value of isolated nocturnal hypertension on ambulatory measurement in 8711 individuals from 10 populations," *Journal of Hypertension*, vol. 28, no. 10, pp. 2036–2045, 2010.
- [44] T. W. Hansen, Y. Li, J. Boggia, L. Thijs, T. Richart, and J. A. Staessen, "Predictive role of the nighttime blood pressure," *Hypertension*, vol. 57, no. 1, pp. 3–10, 2011.
- [45] P. Verdecchia, F. Angeli, and C. Cavallini, "Ambulatory blood pressure for cardiovascular risk stratification," *Circulation*, vol. 115, no. 16, pp. 2091–2093, 2007.
- [46] J. Boggia, L. Thijs, T. W. Hansen et al., "Ambulatory blood pressure monitoring in 9357 subjects from 11 populations highlights missed opportunities for cardiovascular prevention in women," *Hypertension*, vol. 57, no. 3, pp. 397–405, 2011.
- [47] T. W. Hansen, L. Thijs, Y. Li et al., "Prognostic value of reading-to-reading blood pressure variability over 24 hours in 8938 subjects from 11 populations," *Hypertension*, vol. 55, no. 4, pp. 1049–1057, 2010.
- [48] G. Mancia, M. Bombelli, R. Facchetti et al., "Long-term prognostic value of blood pressure variability in the general population: results of the pressioni arteriose monitorate e lassociazioni study," *Hypertension*, vol. 49, no. 6, pp. 1265–1270, 2007.
- [49] E. Ingelsson, K. Björklund-Bodegård, L. Lind, J. Ärnlöv, and J. Sundström, "Diurnal blood pressure pattern and risk of congestive heart failure," *Journal of the American Medical Association*, vol. 295, no. 24, pp. 2859–2866, 2006.
- [50] J. Zeng, M. Jia, H. Ran et al., "Fixed-combination of amlodipine and diuretic chronotherapy in the treatment of essential hypertension: improved blood pressure control with bedtime dosing a multicenter, open-label randomized study," *Hypertension Research*, vol. 34, no. 6, pp. 767–772, 2011.

- [51] N. Miyai, M. Arita, I. Morioka, S. Takeda, and K. Miyashita, "Ambulatory blood pressure, sympathetic activity, and left ventricular structure and function in middle-aged normotensive men with exaggerated blood pressure response to exercise," *Medical Science Monitor*, vol. 11, no. 10, pp. CR478–CR484, 2005.
- [52] P. S. Ramos and C. G. S. Araújo, "Normotensive individuals with exaggerated exercise blood pressure response have increased cardiac vagal tone," *Arquivos Brasileiros de Cardiologia*, vol. 95, no. 1, pp. 85–90, 2010.
- [53] N. Kucukler, F. Yalçın, T. P. Abraham, and M. J. Garcia, "Stress induced hypertensive response: should it be evaluated more carefully?" *Cardiovascular Ultrasound*, vol. 9, no. 1, article 22, 2011.
- [54] K. Ellis, C. E. Pothier, E. H. Blackstone, and M. S. Lauer, "Is systolic blood pressure recovery after exercise a predictor of mortality?" *American Heart Journal*, vol. 147, no. 2, pp. 287–292, 2004.
- [55] E. A. Ashley, V. Raxwal, and V. Froelicher, "An evidence-based review of the resting electrocardiogram as a screening technique for heart disease," *Progress in Cardiovascular Diseases*, vol. 44, no. 1, pp. 55–67, 2001.
- [56] Z. M. Zhang, R. J. Prineas, and C. B. Eaton, "Evaluation and comparison of the minnesota code and novacode for electrocardiographic Q-ST wave abnormalities for the independent prediction of Incident coronary heart disease and total mortality (from the women's health initiative)," *American Journal of Cardiology*, vol. 106, no. 1, pp. 18–25, 2010.
- [57] M. A. Bauml and D. A. Underwood, "Left ventricular hypertrophy: an overlooked cardiovascular risk factor," *Cleveland Clinic Journal of Medicine*, vol. 77, no. 6, pp. 381–387, 2010.
- [58] N. Rumana, T. C. Turin, K. Miura et al., "Prognostic value of ST-T abnormalities and left high R waves with cardiovascular mortality in Japanese (24-Year follow-up of NIPPON DATA80)," *American Journal of Cardiology*, vol. 107, no. 12, pp. 1718–1724, 2011.
- [59] L. Oikarinen, M. S. Nieminen, M. Viitasalo et al., "QRS duration and QT interval predict mortality in hypertensive patients with left ventricular hypertrophy: the losartan intervention for endpoint reduction in hypertension study," *Hypertension*, vol. 43, no. 5, pp. 1029–1034, 2004.
- [60] G. F. Salles, W. Deccache, and C. R. L. Cardoso, "Usefulness of QT-interval parameters for cardiovascular risk stratification in type 2 diabetic patients with arterial hypertension," *Journal of Human Hypertension*, vol. 19, no. 3, pp. 241–249, 2005.
- [61] P. Denes, J. C. Larson, D. M. Lloyd-Jones, R. J. Prineas, and P. Greenland, "Major and minor ECG abnormalities in asymptomatic women and risk of cardiovascular events and mortality," *Journal of the American Medical Association*, vol. 297, no. 9, pp. 978–985, 2007.
- [62] C. T. Larsen, J. Dahlin, H. Blackburn et al., "Prevalence and prognosis of electrocardiographic left ventricular hypertrophy, ST segment depression and negative T-wave: the Copenhagen city heart study," *European Heart Journal*, vol. 23, no. 4, pp. 315–324, 2002.
- [63] P. M. Okin, R. B. Devereux, M. S. Nieminen et al., "Electrocardiographic strain pattern and prediction of cardiovascular morbidity and mortality in hypertensive patients," *Hypertension*, vol. 44, no. 1, pp. 48–54, 2004.
- [64] D. De Bacquer, G. De Backer, M. Kornitzer, K. Myny, Z. Doyen, and H. Blackburn, "Prognostic value of ischemic electrocardiographic findings for cardiovascular mortality in men and women," *Journal of the American College of Cardiology*, vol. 32, no. 3, pp. 680–685, 1998.
- [65] S. Bangalore, F. H. Messerli, F. S. Ou et al., "The association of admission heart rate and in-hospital cardiovascular events in patients with non-ST-segment elevation acute coronary syndromes: results from 135 164 patients in the CRUSADE quality improvement initiative," *European Heart Journal*, vol. 31, no. 5, pp. 552–560, 2010.
- [66] R. Kolloch, U. F. Legler, A. Champion et al., "Impact of resting heart rate on outcomes in hypertensive patients with coronary artery disease: findings from the INternational VErpapamil-SR/trandolapril STudy (INVEST)," *European Heart Journal*, vol. 29, no. 10, pp. 1327–1334, 2008.
- [67] M. T. Cooney, E. Vartiainen, T. Laakitainen, A. Juolevi, A. Dudina, and I. M. Graham, "Elevated resting heart rate is an independent risk factor for cardiovascular disease in healthy men and women," *American Heart Journal*, vol. 159, no. 4, pp. 612–619, 2010.
- [68] G. Parodi, B. Bellandi, R. Valenti et al., "Heart rate as an independent prognostic risk factor in patients with acute myocardial infarction undergoing primary percutaneous coronary intervention," *Atherosclerosis*, vol. 211, no. 1, pp. 255–259, 2010.
- [69] K. Fox, J. S. Borer, A. J. Camm et al., "Resting heart rate in cardiovascular disease," *Journal of the American College of Cardiology*, vol. 50, no. 9, pp. 823–830, 2007.
- [70] J. S. Borer, "Heart rate: from risk marker to risk factor," *European Heart Journal supplements*, vol. 10, pp. F2–F6, 2008.
- [71] K. Fox, R. Ferrari, M. Tendera, P. G. Steg, and I. Ford, "Rationale and design of a randomized, double-blind, placebo-controlled trial of ivabradine in patients with stable coronary artery disease and left ventricular systolic dysfunction: the morbidity-mortality Evaluation of the If inhibitor ivabradine in patients with coronary disease and left ventricular dysfunction (BEAUTIFUL) Study," *American Heart Journal*, vol. 152, no. 5, pp. 860–866, 2006.
- [72] U. E. Heidland and B. E. Strauer, "Left ventricular muscle mass and elevated heart rate are associated with coronary plaque disruption," *Circulation*, vol. 104, no. 13, pp. 1477–1482, 2001.
- [73] T. W. Hansen, L. Thijs, J. Boggia et al., "Prognostic value of ambulatory heart rate revisited in 6928 subjects from 6 populations," *Hypertension*, vol. 52, no. 2, pp. 229–235, 2008.
- [74] P. M. Okin, R. B. Devereux, S. Jern et al., "Regression of electrocardiographic left ventricular hypertrophy during antihypertensive treatment and the prediction of major cardiovascular events," *Journal of the American Medical Association*, vol. 292, no. 19, pp. 2343–2349, 2004.
- [75] A. Oberman, R. J. Prineas, J. C. Larson, A. LaCroix, and N. L. Lasser, "Prevalence and determinants of electrocardiographic left ventricular hypertrophy among a multiethnic population of postmenopausal women (The Women's Health Initiative)," *American Journal of Cardiology*, vol. 97, no. 4, pp. 512–519, 2006.
- [76] A. Jain, H. Tandri, D. Dalal et al., "Diagnostic and prognostic utility of electrocardiography for left ventricular hypertrophy defined by magnetic resonance imaging in relationship to ethnicity: the Multi-Ethnic Study of Atherosclerosis (MESA)," *American Heart Journal*, vol. 159, no. 4, pp. 652–658, 2010.
- [77] A. Kumar, R. J. Prineas, A. M. Arnold et al., "Prevalence, prognosis, and implications of isolated minor nonspecific ST-segment and T-wave abnormalities in older adults cardiovascular health study," *Circulation*, vol. 118, no. 25, pp. 2790–2796, 2008.

- [78] E. Z. Soliman, R. J. Prineas, L. D. Case et al., "Electrocardiographic and clinical predictors separating atherosclerotic sudden cardiac death from incident coronary heart disease," *Heart*, vol. 97, no. 19, pp. 1597–1601, 2011.
- [79] M. J. G. Leening, S. E. Elias-Smale, J. F. Felix et al., "Unrecognised myocardial infarction and long-term risk of heart failure in the elderly: the Rotterdam study," *Heart*, vol. 96, no. 18, pp. 1458–1462, 2010.
- [80] E. Sigurdsson, G. Thorgeirsson, H. Sigvaldason, and N. Sigfusson, "Unrecognized myocardial infarction: epidemiology, clinical characteristics, and the prognostic role of angina pectoris. the Reykjavik study," *Annals of Internal Medicine*, vol. 122, no. 2, pp. 96–102, 1995.
- [81] A. Bauer, J. W. Kantelhardt, P. Barthel et al., "Deceleration capacity of heart rate as a predictor of mortality after myocardial infarction: cohort study," *The Lancet*, vol. 367, no. 9523, pp. 1674–1681, 2006.
- [82] G. Kudaiberdieva, B. Görennek, and B. Timuralp, "Heart rate variability as a predictor of sudden cardiac death," *Anadolu Kardiyoloji Dergisi*, vol. 7, no. 1, pp. 68–70, 2007.
- [83] E. Z. Gorodeski, H. Ishwaran, E. H. Blackstone, and M. S. Lauer, "Quantitative electrocardiographic measures and long-term mortality in exercise test patients with clinically normal resting electrocardiograms," *American Heart Journal*, vol. 158, no. 1, pp. 61–70, 2009.
- [84] S. Mora, R. F. Redberg, Y. Cui et al., "Ability of exercise testing to predict cardiovascular and all-cause death in asymptomatic women: a 20-Year follow-up of the lipid research clinics prevalence study," *Journal of the American Medical Association*, vol. 290, no. 12, pp. 1600–1607, 2003.
- [85] Y. Nishiyama, H. Morita, H. Harada et al., "Systolic blood pressure response to exercise as a predictor of mortality in patients with chronic heart failure," *International Heart Journal*, vol. 51, no. 2, pp. 111–115, 2010.
- [86] C. W. Israel, "Non-invasive risk stratification: prognostic implications of exercise testing," *Herzschrittmachertherapie und Elektrophysiologie*, vol. 18, no. 1, pp. 17–29, 2007.
- [87] J. A. Laukkanen, T. H. Mäkikallio, R. Rauramaa, and S. Kurl, "Asymptomatic ST-segment depression during exercise testing and the risk of sudden cardiac death in middle-aged men: a population-based follow-up study," *European Heart Journal*, vol. 30, no. 5, pp. 558–565, 2009.
- [88] X. Jouven, J. P. Empana, P. J. Schwartz, M. Desnos, D. Courbon, and P. Ducimetière, "Heart-rate profile during exercise as a predictor of sudden death," *The New England Journal of Medicine*, vol. 352, no. 19, pp. 1951–1958, 2005.
- [89] M. S. Lauer, C. E. Pothier, D. J. Magid, S. S. Smith, and M. W. Kattan, "An externally validated model for predicting long-term survival after exercise treadmill testing in patients with suspected coronary artery disease and a normal electrocardiogram," *Annals of Internal Medicine*, vol. 147, no. 12, pp. 821–828, 2007.
- [90] J. Myers, S. Y. Tan, J. Abella, V. Aleti, and V. F. Froelicher, "Comparison of the chronotropic response to exercise and heart rate recovery in predicting cardiovascular mortality," *European Journal of Cardiovascular Prevention and Rehabilitation*, vol. 14, no. 2, pp. 215–221, 2007.
- [91] T. D. Miller, "The exercise treadmill test: estimating cardiovascular prognosis," *Cleveland Clinic Journal of Medicine*, vol. 75, no. 6, pp. 424–430, 2008.
- [92] A. S. Adabag, G. A. Grandits, R. J. Prineas, R. S. Crow, H. E. Bloomfield, and J. D. Neaton, "Relation of heart rate parameters during exercise test to sudden death and all-cause mortality in asymptomatic men," *American Journal of Cardiology*, vol. 101, no. 10, pp. 1437–1443, 2008.
- [93] E. O. Nishime, C. R. Cole, E. H. Blackstone, F. J. Pashkow, and M. S. Lauer, "Heart rate recovery and treadmill exercise score as predictors of mortality in patients referred for exercise ECG," *Journal of the American Medical Association*, vol. 284, no. 11, pp. 1392–1398, 2000.
- [94] M. E. Safar, J. Blacher, and P. Jankowski, "Arterial stiffness, pulse pressure, and cardiovascular disease—Is it possible to break the vicious circle?" *Atherosclerosis*, vol. 218, no. 2, pp. 263–271, 2011.
- [95] S. S. Franklin, "Beyond blood pressure: arterial stiffness as a new biomarker of cardiovascular disease," *Journal of the American Society of Hypertension*, vol. 2, no. 3, pp. 140–151, 2008.
- [96] H. Tanaka, M. Munakata, Y. Kawano et al., "Comparison between carotid-femoral and brachial-ankle pulse wave velocity as measures of arterial stiffness," *Journal of Hypertension*, vol. 27, no. 10, pp. 2022–2027, 2009.
- [97] C. Giannattasio, "Aortic stiffness as a predictor of coronary atherosclerosis," *Journal of Hypertension*, vol. 24, no. 12, pp. 2347–2348, 2006.
- [98] S. Laurent, J. Cockcroft, L. Van Bortel et al., "Expert consensus document on arterial stiffness: methodological issues and clinical applications," *European Heart Journal*, vol. 27, no. 21, pp. 2588–2605, 2006.
- [99] G. F. Mitchell, S. J. Hwang, R. S. Vasan et al., "Arterial stiffness and cardiovascular events: the framingham heart study," *Circulation*, vol. 121, no. 4, pp. 505–511, 2010.
- [100] F. U. Mattace-Raso, T. J. Van Der Cammen, A. Hofman et al., "Arterial stiffness and risk of coronary heart disease and stroke: the Rotterdam Study," *Circulation*, vol. 113, no. 5, pp. 657–663, 2006.
- [101] R. Pini, M. C. Cavallini, V. Palmieri et al., "Central but not brachial blood pressure predicts cardiovascular events in an unselected geriatric population. the ICARE Dicomano Study," *Journal of the American College of Cardiology*, vol. 51, no. 25, pp. 2432–2439, 2008.
- [102] M. J. Roman, R. B. Devereux, J. R. Kizer et al., "Central pressure more strongly relates to vascular disease and outcome than does brachial pressure: the strong heart study," *Hypertension*, vol. 50, no. 1, pp. 197–203, 2007.
- [103] H. Miyashita, A. Aizawa, J. Hashimoto et al., "Cross-sectional characterization of all classes of antihypertensives in terms of central blood pressure in Japanese hypertensive patients," *American Journal of Hypertension*, vol. 23, no. 3, pp. 260–268, 2010.
- [104] J. A. Chirinos, J. P. Zambrano, S. Chakko et al., "Aortic pressure augmentation predicts adverse cardiovascular events in patients with established coronary artery disease," *Hypertension*, vol. 45, no. 5, pp. 980–985, 2005.
- [105] T. Weber, J. Auer, M. F. O'Rourke et al., "Arterial stiffness, wave reflections, and the risk of coronary artery disease," *Circulation*, vol. 109, no. 2, pp. 184–189, 2004.
- [106] G. M. London, J. Blacher, B. Pannier, A. P. Guérin, S. J. Marchais, and M. E. Safar, "Arterial wave reflections and survival in end-stage renal failure," *Hypertension*, vol. 38, no. 3, pp. 434–438, 2001.
- [107] T. Weber, J. Auer, G. Lamm, M. F. O'Rourke, and B. Eber, "Arterial stiffness, central blood pressures, and wave reflections in cardiomyopathy—Implications for risk stratification," *Journal of Cardiac Failure*, vol. 13, no. 5, pp. 353–359, 2007.

- [108] P. S. Lacy, D. G. O'Brien, A. G. Stanley, M. M. Dewar, P. P. R. Swales, and B. Williams, "Increased pulse wave velocity is not associated with elevated augmentation index in patients with diabetes," *Journal of Hypertension*, vol. 22, no. 10, pp. 1937–1944, 2004.
- [109] K. L. Wang, H. M. Cheng, S. H. Sung et al., "Wave reflection and arterial stiffness in the prediction of 15-year all-cause and cardiovascular mortalities: a community-based study," *Hypertension*, vol. 55, no. 3, pp. 799–805, 2010.
- [110] E. Dolan, L. Thijs, Y. Li et al., "Ambulatory arterial stiffness index as a predictor of cardiovascular mortality in the Dublin outcome study," *Hypertension*, vol. 47, no. 3, pp. 365–370, 2006.
- [111] C. M. McEniery, Y. Yasmin, I. R. Hall, A. Qasem, I. B. Wilkinson, and J. R. Cockcroft, "Normal vascular aging: differential effects on wave reflection and aortic pulse wave velocity: the Anglo-Cardiff Collaborative Trial (ACCT)," *Journal of the American College of Cardiology*, vol. 46, no. 9, pp. 1753–1760, 2005.
- [112] F. G. Fowkes, M. Criqui, and G. D. Murray, "Ankle brachial index improves prediction of mortality determined by Framingham risk score in 48, 115 healthy subjects in sixteen studies worldwide," *Circulation*, vol. 114, article II.907, 2006.
- [113] F. G. Fowkes, G. D. Murray, I. Butcher et al., "Ankle brachial index combined with framingham risk score to predict cardiovascular events and mortality: a meta-analysis," *Journal of the American Medical Association*, vol. 300, no. 2, pp. 197–208, 2008.
- [114] J. Yeboah, R. L. McClelland, T. S. Polonsky et al., "Comparison of novel risk markers for improvement in cardiovascular risk assessment in intermediate-risk individuals," *The Journal of the American Medical Association*, vol. 308, no. 8, pp. 788–795, 2012.
- [115] J. B. Meigs, D. M. Nathan, R. B. D'Agostino Sr., and P. W. F. Wilson, "Fasting and postchallenge glycemia and cardiovascular disease risk: the framingham offspring study," *Diabetes Care*, vol. 25, no. 10, pp. 1845–1850, 2002.
- [116] American Diabetes Association, "Diagnosis and classification of diabetes mellitus," *Diabetes Care*, vol. 35, pp. 562–569, 2012.
- [117] N. Sarwar, P. Gao, S. R. Seshasai et al., "Fasting blood glucose concentration, and risk of vascular disease: a collaborative meta-analysis of 102 prospective studies," *The Lancet*, vol. 375, no. 9733, pp. 2215–2222, 2010.
- [118] Q. Qiao, K. Pyörälä, M. Pyörälä et al., "Two-hour glucose is a better risk predictor for incident coronary heart disease and cardiovascular mortality than fasting glucose," *European Heart Journal*, vol. 23, no. 16, pp. 1267–1275, 2002.
- [119] K. A. Eagle, G. S. Ginsburg, K. Musunuru et al., "Identifying patients at high risk of a cardiovascular event in the near future: current status and future directions: report of a national heart, lung, and blood institute working group," *Circulation*, vol. 121, no. 12, pp. 1447–1454, 2010.
- [120] T. A. Manolio, R. A. Kronmal, G. L. Burke, D. H. O'Leary, and T. R. Price, "Short-term predictors of incident stroke in older adults: the cardiovascular health study," *Stroke*, vol. 27, no. 9, pp. 1479–1486, 1996.
- [121] S. Lange, H. J. Trampisch, R. Haberl et al., "Excess 1-year cardiovascular risk in elderly primary care patients with a low ankle-brachial index (ABI) and high homocysteine level," *Atherosclerosis*, vol. 178, no. 2, pp. 351–357, 2005.
- [122] T. Weber, J. Auer, M. F. O'Rourke et al., "Increased arterial wave reflections predict severe cardiovascular events in patients undergoing percutaneous coronary interventions," *European Heart Journal*, vol. 26, no. 24, pp. 2657–2663, 2005.
- [123] M. R. Nelson, J. Stepanek, M. Cevette, M. Covalciuc, R. T. Hurst, and A. J. Tajik, "Noninvasive measurement of central vascular pressures with arterial tonometry: clinical revival of the pulse pressure waveform?" *Mayo Clinic Proceedings*, vol. 85, no. 5, pp. 460–472, 2010.
- [124] A. Dogui, N. Kachenoura, F. Frouin et al., "Consistency of aortic distensibility and pulse wave velocity estimates with respect to the Bramwell-Hill theoretical model: a cardiovascular magnetic resonance study," *Journal of Cardiovascular Magnetic Resonance*, vol. 13, article 11, 2011.
- [125] C. C. Y. Poon, Q. Liu, H. Gao, W. H. Lin, and Y. T. Zhang, "Wearable intelligent systems for E-health," *Journal of Computing Science and Engineering*, vol. 5, no. 3, pp. 246–256, 2011.
- [126] M. Z. Poh, D. J. McDuff, and R. W. Picard, "Non-contact, automated cardiac pulse measurements using video imaging and blind source separation," *Optics Express*, vol. 18, no. 10, pp. 10762–10774, 2010.
- [127] S. Suzuki, T. Matsui, H. Imuta et al., "A novel autonomic activation measurement method for stress monitoring: non-contact measurement of heart rate variability using a compact microwave radar," *Medical and Biological Engineering and Computing*, vol. 46, no. 7, pp. 709–714, 2008.
- [128] K. G. Ng, C. M. Ting, J. H. Yeo et al., "Progress on the development of the MediWatch ambulatory blood pressure monitor and related devices," *Blood Pressure Monitoring*, vol. 9, no. 3, pp. 149–165, 2004.
- [129] C. C. Y. Poon, Y. M. Wong, and Y. T. Zhang, "M-health: the development of cuff-less and wearable blood pressure meters for use in body sensor networks," in *Proceedings of the IEEE/NLM Life Science Systems and Applications Workshop (LSSA '06)*, Bethesda, Md, USA, July 2006.
- [130] P. Shaltis, A. Reisner, and H. Asada, "Calibration of the photoplethysmogram to arterial blood pressure: capabilities and limitations for continuous pressure monitoring," in *Proceedings of the 27th Annual International Conference of the Engineering in Medicine and Biology Society (IEEE-EMBS '05)*, pp. 3970–3973, Shanghai, China, September 2005.
- [131] C. M. Girardin, C. Huot, M. Gonthier, and E. Delvin, "Continuous glucose monitoring: a review of biochemical perspectives and clinical use in type 1 diabetes," *Clinical Biochemistry*, vol. 42, no. 3, pp. 136–142, 2009.
- [132] C. E. Ferrante do Amaral and B. Wolf, "Current development in non-invasive glucose monitoring," *Medical Engineering and Physics*, vol. 30, no. 5, pp. 541–549, 2008.
- [133] M. J. Tierney, J. A. Tamada, R. O. Potts, L. Jovanovic, and S. Garg, "Clinical evaluation of the GlucoWatch biographer: a continual, non-invasive glucose monitor for patients with diabetes," *Biosensors and Bioelectronics*, vol. 16, no. 9–12, pp. 621–629, 2001.
- [134] Y. Liu, C. C. Poon, Y. T. Zhang, G. W. Yip, and C. M. Yu, "A novel method for assessing arterial stiffness by a hydrostatic approach," in *Proceedings of the Annual International Conference of the IEEE Engineering in Medicine and Biology Society (EMBC '09)*, pp. 1789–1791, Engineering in Medicine and Biology Society, Minneapolis, Minn, USA, 2009.
- [135] Y. T. Zhang, C. C. Y. Poon, C. H. Chan, M. W. W. Tsang, and K. F. Wu, "A health-shirt using e-textile materials for the continuous and cuffless monitoring of arterial blood pressure," in *Proceedings of the 3rd IEEE-EMBS International Summer School and Symposium on Medical Devices and Biosensors (ISS-MDBS '06)*, pp. 86–89, Boston, Mass, USA, September 2006.
- [136] A. Beard, M. L. Neal, N. Tabesh-Saleki et al., "Multiscale modeling and data integration in the virtual physiological rat

- project,” *Annals of Biomedical Engineering*, vol. 40, no. 11, pp. 2365–2378, 2012.
- [137] P. J. Hunter and T. K. Borg, “Integration from proteins to organs: the physiome project,” *Nature Reviews Molecular Cell Biology*, vol. 4, no. 3, pp. 237–243, 2003.
- [138] “Wellcome trust heart physiome project,” 2004, <http://heart.physiomeproject.org/index.html>.
- [139] N. Smith, A. D. de Vecchi, M. McCormick et al., “euHeart: personalized and integrated cardiac care using patient-specific cardiovascular modelling,” *Interface Focus*, vol. 1, no. 3, pp. 349–364, 2011.
- [140] V. Y. Wang, H. I. Lam, D. B. Ennis, B. R. Cowan, A. A. Young, and M. P. Nash, “Modelling passive diastolic mechanics with quantitative MRI of cardiac structure and function,” *Medical Image Analysis*, vol. 13, no. 5, pp. 773–784, 2009.
- [141] P. Hunter, N. Smith, J. Fernandez, and M. Tawhai, “Integration from proteins to organs: the IUPS physiome project,” *Mechanisms of Ageing and Development*, vol. 126, no. 1, pp. 187–192, 2005.

Research Article

A Novel Multiinstance Learning Approach for Liver Cancer Recognition on Abdominal CT Images Based on CPSO-SVM and IO

Huiyan Jiang,^{1,2} Ruiping Zheng,¹ Dehui Yi,³ and Di Zhao¹

¹ Software College, Northeastern University, Shenyang 110819, China

² Key Laboratory of Medical Image Computing of Ministry of Education, Shenyang 110819, China

³ Department of Hepatobiliary Surgery, First Affiliated Hospital of China Medical University, Shenyang 110001, China

Correspondence should be addressed to Huiyan Jiang; hyjiang@mail.neu.edu.cn

Received 18 July 2013; Revised 24 October 2013; Accepted 6 November 2013

Academic Editor: Yunmei Chen

Copyright © 2013 Huiyan Jiang et al. This is an open access article distributed under the Creative Commons Attribution License, which permits unrestricted use, distribution, and reproduction in any medium, provided the original work is properly cited.

A novel multi-instance learning (MIL) method is proposed to recognize liver cancer with abdominal CT images based on instance optimization (IO) and support vector machine with parameters optimized by a combination algorithm of particle swarm optimization and local optimization (CPSO-SVM). Introducing MIL into liver cancer recognition can solve the problem of multiple regions of interest classification. The images we use in the experiments are liver CT images extracted from abdominal CT images. The proposed method consists of two main steps: (1) obtaining the key instances through IO by texture features and a classification threshold in classification of instances with CPSO-SVM and (2) predicting unknown samples with the key instances and the classification threshold. By extracting the instances equally based on the entire image, the proposed method can ignore the procedure of tumor region segmentation and lower the demand of segmentation accuracy of liver region. The normal SVM method and two MIL algorithms, Citation-kNN algorithm and WEMISVM algorithm, have been chosen as comparing algorithms. The experimental results show that the proposed method can effectively recognize liver cancer images from two kinds of cancer CT images and greatly improve the recognition accuracy.

1. Introduction

With the development of computer technology, computer aided diagnosis (CAD) [1] technology used in quantitative analysis of medical imaging arose at the historic moment and became one of the research hotspots in medical imaging. Imageological diagnosis for liver cancer mainly includes four ways, angiography, ultrasonic scan, computed tomography (CT), and magnetic resonance imaging (MRI). In the early diagnosis of liver cancer, the CT image is generally preferred by the doctor [2] because of its high resolution, low damage to human body, and the ability to reflect the pathological position of liver cancer accurately. In traditional image diagnosis, the diagnosis of a mass of CT images brings a radiologist a huge workload. And an omission of a tiny detail because of the differences of visions or experiences may cause a wrong classification [3]. Moreover, liver cancer has the

characteristics of difficult treatment, poor curative effect, and high mortality. So, it urgently needs liver cancer CAD to give advisory opinions to the doctor and help improve the correct diagnostic rate.

Traditional liver cancer recognition methods in CAD can be roughly divided into two categories, learning-based classification and nonparametric classification. The approach of learning-based classification mainly includes Bayesian-based approach [4], SVM-based approach [5, 6], and ensemble learning approaches [7, 8]. In these methods, the classified image is the entire medical image [9], and the input features for classifier are usually from the region of interest (ROI). For example, the ROI of a liver cancer samples is the tumor region. However, the segmentation results of tumor region are always not accurate because the contrast of tumor regions, image artifacts, and other organizations is not obvious. This results in the fact that the tumor features extracted from ROIs

are not accurate. Finally, it will have a great influence on classification accuracy.

As for the above-mentioned problems, Hu et al. [10] introduced MIL first to the classification of breast tumors in ultrasound images. Using MIL can more clearly express the image with both tumor region and normal region, so as to solve the problem of multiple ROIs classification. However, Citation-kNN algorithm used in [10] has two problems.

- (1) Not considering the distribution characteristics of the images, such as relative distance, scattered degree, and sparse degree. It results that the classification accuracy is not high.
- (2) As a lazy learning algorithm, Citation-kNN needs to save the whole training set and go through the whole sample space when predicting. So it will cost a lot of time when classifying.

MIL was first proposed by Dietterich et al. in the context of drug activity prediction [11]. Since MIL was put forward, a lot of related learning algorithms have been proposed. Maron and Ratan [12] defined diverse density function and proposed Diverse Density (DD) algorithm by seeking optimal point of diverse density function as a concept point in the instances' attribute space. Zhang and Goldman [13] proposed EM-DD algorithm by combining DD algorithm with the Expectation Maximization (EM). Wang and Zucker [14] improved the K-nearest neighbor (kNN) algorithm and proposed two lazy learning algorithms named Bayesian-kNN algorithm and Citation-kNN algorithm. Andrews et al. [15] proposed mi-SVM algorithm and MI-SVM algorithm by introducing the MIL constraints to the objective function of SVM. Gartner et al. put forward MIL kernels, such as set kernels and statistic kernels, which are used to measure the similarity between two bags, and then the MIL problem will be transformed into traditional SVM learning problem. Chen and Wang [16] proposed DD-SVM MIL algorithm through the space conversion method. Zhou and Xu [17] proposed MissSVM algorithm using a special semisupervised SVM for MIL.

Huang [18] studied the combination of SVM and MIL (SVM-MIL) further and proposed an SVM-MIL method named WEMISVM. They converted MIL problem to the traditional single instance learning problem through dissolving of every bag and labeling its instances a consistent value with each bag's label. In the training phase, they regarded the average of the instance possible values calculated by voting method in ensemble learning as the label of the target bag. However, applying WEMISVM method to liver cancer recognition has a big problem. WEMISVM method assumes that the instances in one bag are independent of each other, and each instance has the same influence on its bag's label. While in fact each instance has a different influence on its bag's label, for example, the liver cancer block should have much influence on the label of the liver cancer image than the other blocks. In addition, the classification accuracy of WEMISVM method on 14 data sets is also not very high.

SVM is a supervised classifier which aims at finding hyperplane that separates the dataset with maximum margin [19]. The SVM parameters directly affect the learning ability

and generalization ability of the classifier. So the improvement of SVM is usually realized by the optimization of SVM parameters. Recently there are many algorithms for SVM parameters optimization, such as genetic algorithm (GA), ant colony optimization (ACO), and particle swarm optimization (PSO). PSO has a high precision and fast convergence rate, so it is generally used in parameter optimization. However, in this paper, every sample needs to use the parameters optimization once, which means that using this method for parameter optimization will consume a lot of time. local optimization (LO) can reduce the time for optimization when there is a good reference point. So we use a combination algorithm of particle swarm optimization and local optimization (CPSO) to optimize the parameters.

In order to obtain a classifier with high classification accuracy and low time complexity for liver cancer recognition, we use MIL method to solve multiple ROIs classification problem, use the idea of bag dissolution to convert MIL problem into a single instance learning problem, use CPSO-SVM to obtain the label of the target bag, and use ensemble learning method to improve the classification performance, and finally we proposed the SVM-IOMIL algorithm. The advantages of our algorithm are as follows.

- (1) The instances are extracted equally based on the entire image, so our method can ignore the process of tumor region segmentation and lower the requirements of liver region segmentation accuracy.
- (2) Through two-time instance optimization to find the key instances and the modified CPSO-SVM classifier to classify, our method greatly improved the recognition accuracy of liver cancer.

The rest of this paper is arranged as follows. Section 2 gives a simple description of SVM and MIL and a specific description of our proposed algorithm. Results and discussion of our method are presented in Section 3. Section 4 concludes this paper and expounds our future work.

2. Materials and Method

2.1. Multiinstance Learning. In the field of machine learning, according to the ambiguity of training data, this field can be roughly divided into three learning frameworks: supervised learning, unsupervised learning, and reinforcement learning. As a new learning framework, MIL [10] is the new weak supervised learning method presented by Dietterich et al. to solve the problem of molecular activity prediction. It can be described as follows.

We suppose that each data in the training data set is a bag, which is a set of instances, and each bag has a training label, while the instances in the bag are not labeled. If a bag is labeled positive, there will be at least one positive instance in the bag. If a bag is labeled negative, all of the instances in it are negative. The goal of MIL algorithm is to train a classifier, which can classify unseen bags correctly by learning the training bags. MIL framework is shown in Figure 1.

2.2. Support Vector Machine. In the 1990s, Vapnik [20] proposed SVM theory for solving classification problems.

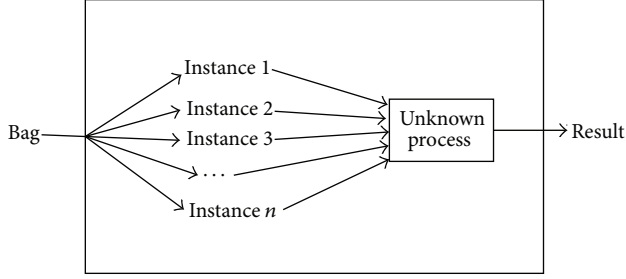


FIGURE 1: MIL framework diagram.

The theory is based on VC dimension theory and structural risk minimization in statistical learning theory (SLT). In order to obtain the best classification performance and promotion capability, the theory uses the information of limited instances to seek the best compromise between the complexities of the model. Since SVM has shown a good learning ability, performance, and the ability of generalization, it causes great attention to the field [21].

SVM is a supervised classifier which aims at finding hyperplane that separates the dataset with maximum margin. Suppose that the training sample set is $\{(x_1, y_1), (x_2, y_2), \dots, (x_n, y_n)\}$, where $x_i \in R^m$ ($i = 1, 2, \dots, n$) stands for the i th sample, n is the number of training samples, and $y_i \in \{-1, 1\}$ is the corresponding category label. Before training, it needs to map the input vector to a high-dimensional feature space H using a mapping function. Then, in this high-dimensional space, it needs to construct hyperplane which has the largest classification interval, namely, the optimal hyperplane, to ensure minimum classification error rate.

The classification surface equation is $w \cdot z + b = 0$, and then we obtain a mapping $\Phi : R_m \rightarrow H$. The objective function is shown as

$$\min L(w) = \frac{1}{2} \|w\|^2 + C \sum_{i=1}^N s_i \xi_i, \quad s_i > 0, \quad (1)$$

$$y_i (w z_i + b_i) \geq 1 - \xi_i, \quad \xi_i \geq 0, \quad i = 1, 2, \dots, N.$$

In (1), C is the penalty factor, ξ_i is the relaxation factor, and s_i is the coefficient of Lagrange.

The optimal hyperplane can be obtained by quadratic optimization. When the number of features is extremely huge, in order to solve the objective function effectively, we can transform the objective function into the corresponding dual forms.

Let the optimal solution be w^* ; thus the discriminate function for binary classification is defined as

$$f(x) = \text{sgn} \left(\sum_{i=1}^N w_i^* y_i z_i + b^* \right). \quad (2)$$

When we construct the optimal hyperplane in the feature space H , the training algorithm only uses the dot product in the space, $\Phi(x_i) \cdot \Phi(x_j)$. So, the only thing we need to do is finding a function K which satisfies $K(x_i, x_j) = \Phi(x_i) \cdot \Phi(x_j)$.

In this way, we only need to operate the dot product which can be realized by the function K in the original space, and there is no need to know the form of the transformation Φ . According to the related functional theory, if and only if $K(x_i, x_j)$ satisfies the Mercer constraint [20], the kernel function $K(x_i, x_j)$ would be corresponding to an inner dot product in some transformation space.

Therefore, though introducing the kernel function, the discriminate function for binary classification is redefined as

$$f(x) = \text{sgn} \left(\sum_{i=1}^N w_i^* y_i K(x_i, x) + b^* \right), \quad (3)$$

where b^* is any w_j^* which satisfies the constraint $C > w_j^* > 0$. Putting it into (3), we obtain

$$y_j \left(\sum_{i=1}^l w_i^* y_i K(x_i, x) + b^* \right) = 1. \quad (4)$$

2.3. Liver Cancer Recognition Based on SVM-IOMIL. In this section, firstly we will introduce the whole procedure of the proposed method, which is shown in Figure 2, and then we will give a detailed explanation of each process.

In this paper, SVM-IOMIL _{i} ($i = 1, 2, 3$) stands for three classifiers used for different datasets. SVM-IOMIL₁ is a classifier for liver cancer and normal liver, SVM-IOMIL₂ is a classifier for liver cancer and liver cirrhosis, and SVM-IOMIL₃ is a classifier for liver cancer and liver cyst.

The process of the proposed method is as follows.

- (1) *Image Preprocessing.* Before the preprocessing, we extract the liver region manually from the abdominal CT image. Then we normalize the images and process them with histogram equalization after extraction.
- (2) *Instance Extracting.* We regard the liver CT image extracted by the first process as a bag and the block extracted equally based on the entire liver CT image as an instance.
- (3) *Feature Extraction.* In this paper, we use Gray Level Concurrence Matrix (GLCM) to extract the features for classification.
- (4) *Instance Optimization.* We use two-time instance optimization and CPSO-SVM to extract the instances and get the key instances finally.
- (5) *Predicting the Unknown Samples.* We use the key instances and a classification threshold to predict the unknown samples.

2.3.1. Preprocessing. Preprocessing includes image normalization and histogram equalization. As MIL algorithm does not require segmentation accuracy, we extract the liver region manually. The inaccurate sections of liver region are marked with a red curve in Figure 3(a).

In the procedure of image normalization, according to the location of the liver in the image and the experimental observation, we normalize the size of the images to

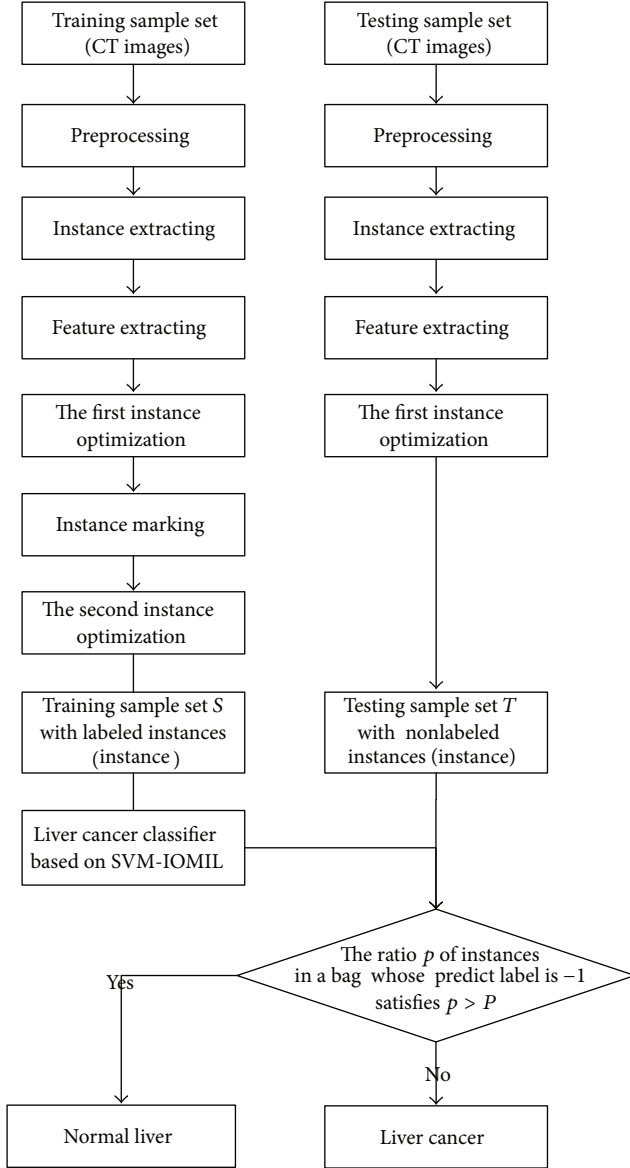


FIGURE 2: The main flow of the proposed method.

339×339 . The result of the image after normalization is shown in Figure 3(b).

In order to make the image texture characteristics clearer, we process the CT images with histogram equalization, as a result we highlight the difference between two categories of images. The result of histogram equalization is shown in Figure 3(c).

2.3.2. Instance Extraction. In order to extract the instances, firstly we define the CT image after preprocessing as a bag, and then we define the bag structure through extracting the blocks equally based on the entire liver CT image and define each block as an instance. The bag structure is shown in Figure 4.

The tumor block will be defined as a liver cancer instance, while the others will be defined as nonmalignant liver

instances. Therefore, a nonmalignant liver instance can exist in a liver cancer image or a nonmalignant liver image, while a liver cancer instance can only exist in a liver cancer image. The bag is defined as positive if there is at least one liver cancer instance in the CT image. Otherwise it will be defined as negative.

2.3.3. Feature Extraction. Angular second moment (ASM) can reflect an image's uniformity degree of grayscale distribution and the texture roughness. Entropy (ENT) can show the texture complexity of an image. Contrast (CON) can reflect the sharpness of the image and the depth of groove in texture. Correlation (COR) can show the correlation of local grayscale in an image. Therefore, we extract features from 8 matrices which are from 4 directions $\theta = \{0^\circ, 45^\circ, 90^\circ, 135^\circ\}$ and 2 distances $d = \{1, 2\}$ by Gray Level Concurrence Matrix (GLCM) for each instance. Finally we choose the mean and variance of 4 texture features, which are ASM, ENT, CON, and COR, respectively, in 2 distances as the experiment features. The design equations for the texture features are shown as

$$\begin{aligned}
 \text{ASM} &= \sum_i \sum_j I(i, j)^2, \\
 \text{ENT} &= -\sum_i \sum_j I(i, j) \lg I(i, j), \\
 \text{CON} &= \sum_i \sum_j (i - j)^2 I(i, j), \\
 \text{COR} &= \frac{[\sum_i \sum_j ((ij) I(i, j)) - u_x u_y]}{\sigma_x \sigma_y},
 \end{aligned} \tag{5}$$

where $I(i, j)$ is the element of the image, and $u_x, u_y, \sigma_x, \sigma_y$ is defined as follows, respectively: $u_x = \sum_i \sum_j I(i, j)$, $u_y = \sum_i i \sum_j I(i, j)$, $\sigma_x = \sum_i (i - u_x) \sum_j I(i, j)$, and $\sigma_y = \sum_j (j - u_y) \sum_i I(i, j)$.

2.3.4. Instance Optimization. Before marking the instances, in order to minimize the interference of background and reduce the cost of operation, we optimize the instances for the first time. After marking the instances, in order to improve the classification performance, we optimize the instances for the second time.

(1) *The First Instance Optimization.* The ASM value of the background block, which is the block without liver region, is 1, while the ASM value of the block with the liver region cannot be 1. So, according to the ASM value, we can determine whether the current instance is background block or not. If it is background block, we abandon the instance directly to remove interference or we reserve it temporarily.

We labeled the instance with the label of the bag which the instance belongs to. Furthermore if the instance reserved after the first instance optimization is in a positive bag, we mark it to 1; otherwise, we mark it to -1. After the first

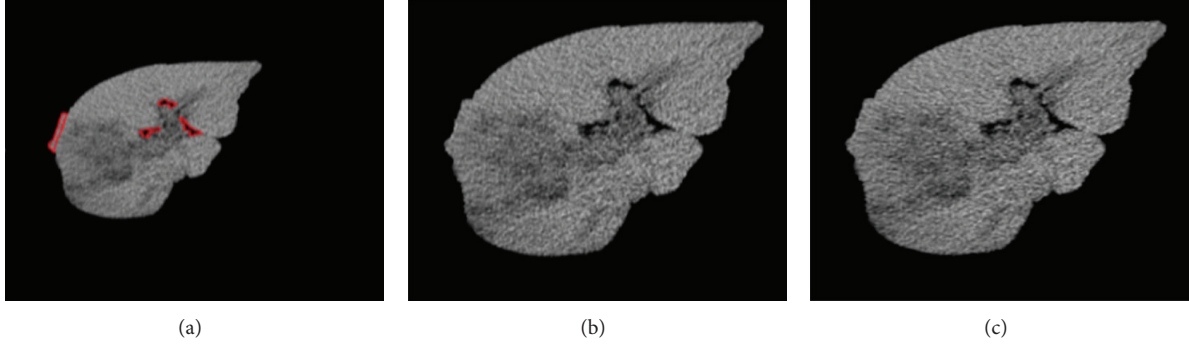


FIGURE 3: Preprocessing for liver CT images. (a) Liver region. (b) Normalization result. (c) Histogram equalization result.

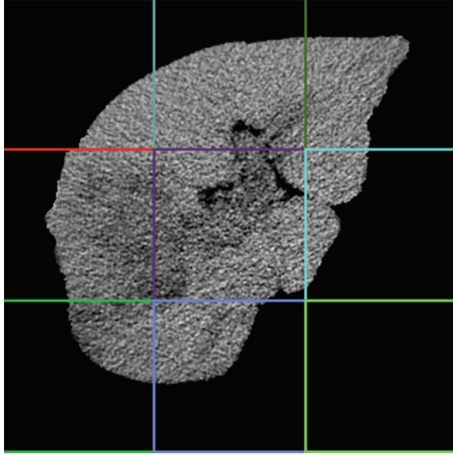


FIGURE 4: Bag structure sketch.

instance optimization, the image with instance label is shown in Figure 5.

(2) *The Second Instance Optimization.* Figure 5 illustrates that some instances have less liver region and more background. This leads to the classification interference. So we improve the algorithm further. Firstly, in training phase, we choose the instances classified correctly in the bags which have the higher classification accuracy as “excellent instances.” Secondly, we store the “excellent instances” into a new training set. Then we determine the category of instances and bags according to the new training set. In this way, we have improved the accuracy of recognition. The second instance optimization must be processed through experiments, so we do not know the result in advance. Figure 6 shows a possible case.

2.3.5. *Construction of Liver Cancer Classifier.* N is the total number of instances and $N = \sum_{i=1}^l n_i$, n_i is the amount instances in i th bag. According to the character of liver cancer, we redefine the objective function for SVM as

$$\begin{aligned} \min L(w) &= \frac{1}{2} \|w\|^2 + C \sum_{i=1}^N a_j \xi_i, \quad a_j \in \{0, 1\}, \\ y_i (w + b_i) &\geq 1 - \xi_i, \quad \xi_i \geq 0, \quad i = 1, 2, \dots, N, \end{aligned} \quad (6)$$

where C is the penalty factor. ξ_i is the relaxation factor. a_j is the parameter used for instance extraction and its default value is 0.

The process of classifier construction for liver cancer and normal liver is as follows:

input: the training set D which contains the labeled training bags;

output: SVM-IOMIL₁ classifier (w^*, b^*) .

Step 1. Set the instances attribute space $S = \emptyset$ and then extract instances in S .

Step 2. For all $B_i \in D$, B_i is a bag and B_{ij} is the j th instance of the bag B_i .

If B_i is a positive bag, we classify the instance B_{ij} reserved after the first instance optimization in this bag, by SVM classifier. We label the “excellent instance” to 1, set the parameter a_j to 1, and add them to S .

If B_i is a negative bag, we classify the instance B_{ij} , and then we label the “excellent instance” to -1 , set the parameter a_j to 0, and add them to S .

Step 3. Optimize the parameters of the SVM classifier by choosing the best penalty factor C and the kernel function’s control factor g .

Step 4. Set S as the training sample set and train the SVM-IOMIL₁ classifier (w^*, b^*) according to (6).

Step 5. If B_i is not the last instance, then go to Step 2. Otherwise, we get our classifier and the key instances which is a set of the “excellent instances.”

The SVM-IOMIL₂ classifier for liver cancer and liver cirrhosis and the SVM-IOMIL₃ classifier for liver cancer and liver cyst are the same as SVM-IOMIL₁, so there is no need to repeat them here.

2.3.6. *Prediction Algorithm for Classification.* After the classifier construction, we use the liver CT images which are not used in training to test the classifier as follows:

input: training sample set S and testing sample set T which contains the unlabeled test bags;

output: the classification result of the test bag B .

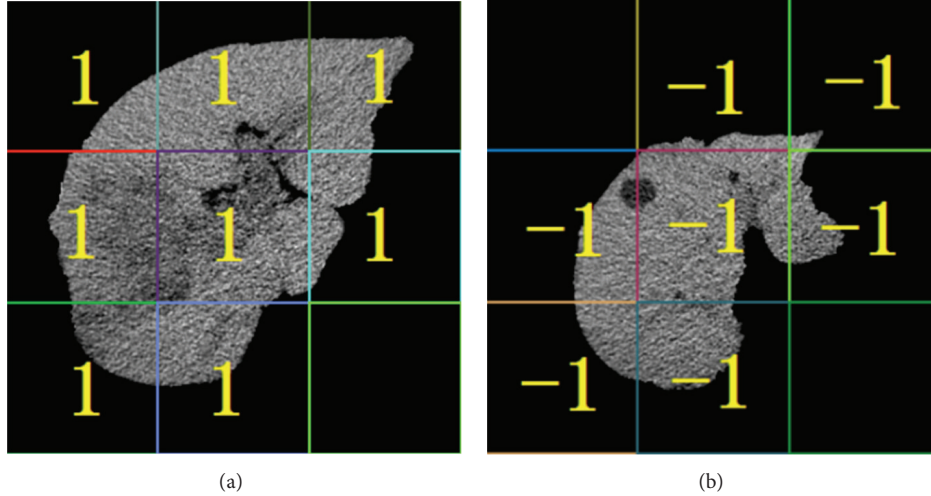


FIGURE 5: Result of the first instance optimization. (a) Instance label for liver cancer image. (b) Instance label for liver cyst image.

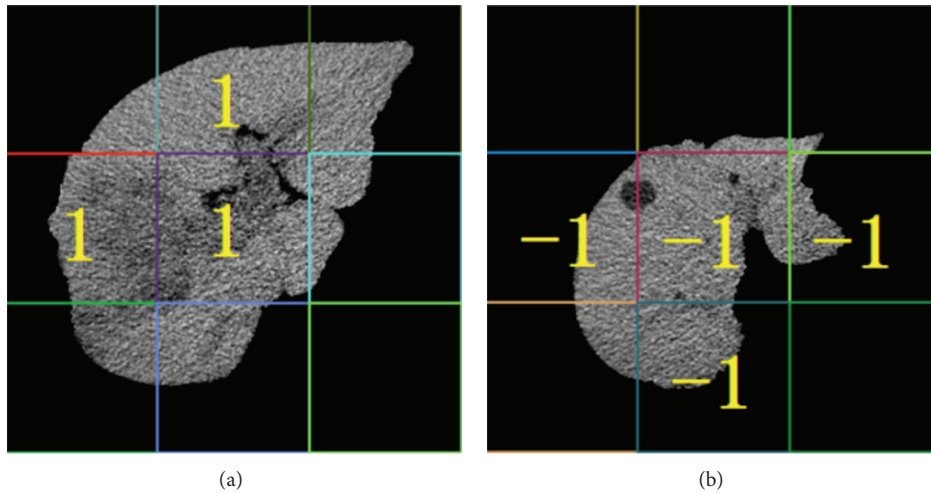


FIGURE 6: Result of the second instance optimization. (a) Instance label for liver cancer image. (b) Instance label for liver cyst image.

Step 1. Put the test bag B contained in testing sample set T into SVM-IOMIL₁ classifier (w^*, b^*).

Step 2. Predict the reserved instance after the first instance optimization in test bag B according to (3).

If the ratio that the label of the instance in test bag B predicted to be -1 is larger than threshold P , the test bag B will be a negative bag; otherwise, it will be a positive bag.

3. Results and Discussion

3.1. The Experimental Data and Environment. The original data are 440 abdominal CT images provided by the radiology department of a large hospital in Shenyang, China. These images are abdominal CT images with a resolution of 512×512 pixels, which are BMP format. After preprocessing, the images we use in the experiments are liver CT images with a resolution of 339×339 pixels and their format is BMP. The

TABLE 1: Datasets used in our experiments.

Images	Training samples	Testing samples	Total
Liver cancer	40	40	80
Normal cancer	60	60	120
Liver cirrhosis	60	60	120
Liver cyst	60	60	120

images include 120 normal liver cases, 120 liver cyst cases, 120 liver cirrhosis cases, and 80 liver cancer cases. The datasets used in this paper are shown in Table 1.

In this paper, we divide each kind of the images into two parts randomly and equally. One part is regarded as a potential sub-set of the training set, and the other one is the part of the potential subset of the testing set. The training set consists of one part of the liver cancer images and one part of other images. We divide the original testing data randomly into 5 groups and then we regard the data in one group as

current validation set and the data of the key instances as training set. Finally, we use the average value of the validation set's evaluation criterion in these 5 groups as the classifier's performance evaluation criterion.

Experimental environment is as follows: Intel(R) Core (TM) i7-2600 CPU @3.4 GHz, 4 G RAM, 900 G hard disk, Windows7 OS, and MATLAB 7.14 simulation environment.

3.2. Evaluation Criterion for Classification Performance. In experiments, we use accuracy (ACC), sensitivity (SEN), specificity (SPE), processing time (PT), and training time (TT) to evaluate classification performance of the liver cancer recognition experiment. The definitions of the evaluation criterion are shown as

$$\begin{aligned} \text{ACC} &= \frac{\text{TP} + \text{TN}}{\text{TP} + \text{FN} + \text{TN} + \text{FP}}, \\ \text{SEN} &= \frac{\text{TP}}{\text{TP} + \text{FN}}, \\ \text{SPE} &= \frac{\text{TN}}{\text{TN} + \text{FP}}, \end{aligned} \quad (7)$$

where TP and FN are the number of positive samples discriminated right and wrong, respectively, and TN and FT are the number of negative samples discriminated right and wrong, respectively.

Sensitivity mainly represents the recognition accuracy of liver cancer. Specificity represents the recognition accuracy of nonmalignant liver.

Processing time (PT): the time from inputting images to extracting features.

Training time (TT): the time from acquiring the information of feature data to acquiring the result of classification.

3.3. Experimental Results and Analysis

3.3.1. Determining the Best Block Length. When we regard the blocks which we segmented equally based on the entire liver CT image as instances, the size of the block has a great influence on classification results. In order to obtain an objective data, we do multigroup experiments on different block length based on the existing Citation-kNN algorithm. The experimental results are shown in Figure 7.

Analyzing the experimental data from Figure 7, we obtain the following conclusions. (1) The smaller the size of block is, the more the number of instances is and the more the PT is, but the effect on ACC is small. (2) When the size of blocks is small, with the block length increasing, ACC increases. When the size of blocks is bigger than 113, with the block length increasing, ACC decreases. When the size of block is 169.5, ACC decreases sharply.

The reasons are as follows. (1) The more blocks lead to more time for feature extraction, so the PT increases. (2) Using a smaller block length means fewer pixels in the block, and GLCM is statistics-based texture features. Therefore it does not reflect the statistical properties. Furthermore the

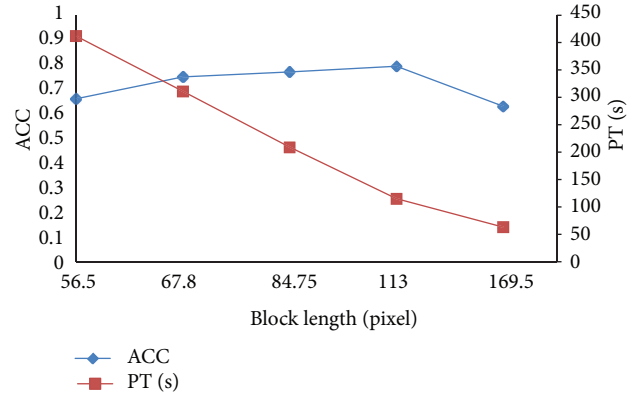


FIGURE 7: Classification results on different block length.

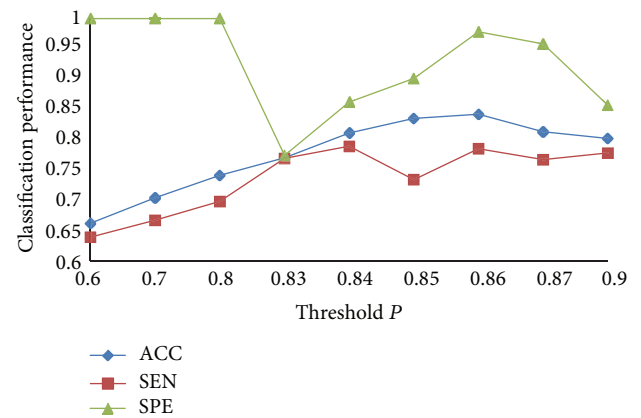
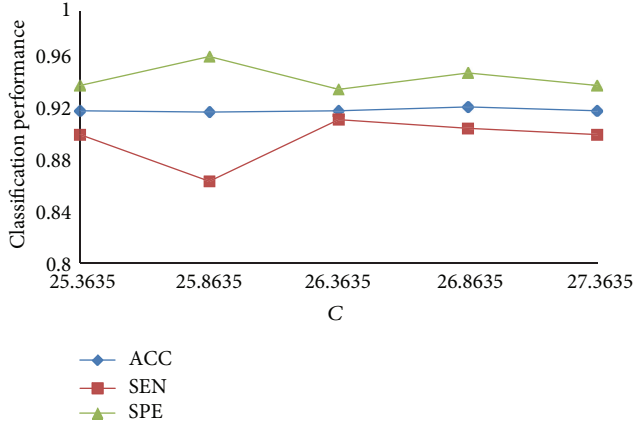


FIGURE 8: Classification results on different thresholds.

speckle noise is also easy to affect the quality of feature extraction and ultimately makes ACC decrease. After that, through the increasing block length, the amount of information in a block increases, and ACC gradually increases. But to a certain amount, since the block is too large, much more complex texture information will be mixed; ACC decreases instead. Considering PT and ACC, we obtain the best classification effect when the block length is 113.

3.3.2. Determining the Threshold. The instances in a liver cancer image are not all tumor blocks. In fact few of them are tumor blocks. So the threshold P should be in $[0.5, 1]$. We do 9 groups of experiments with different threshold P , and the minimum increase margin is 0.01. The comparison of experimental results is shown in Figure 8.

In Figure 8, when P varies from 0.6 to 0.85, ACC increases obviously; when P is 0.86, ACC is the best; when P continues to increase, ACC decreases instead. As a whole SEN increases firstly and then decreases, SPE decreases firstly and then increases. They can achieve a balance when ACC is the best. The reasons are as follows. When P is smaller, it means that we regard more liver cancer cases as nonmalignant liver cases, and this will produce a large number of false positive bags. As a result, all the nonmalignant liver cases can be recognized correctly, but ACC of liver cancer cases is very low.

FIGURE 9: Classification results with different values of C .

When P is a certain value, we can recognize the liver cancer better. Through analysis of the experiment results, when P is 0.86, we get the best classification effect.

3.3.3. Parameter Optimization for SVM. Parameter optimization undoubtedly can improve the accuracy of classification when we use SVM for classification. There are many parameters in SVM, and they always have a default value. But we cannot get the desired effect in many cases with the default values. So we optimize the parameters C and g in order to achieve the optimal classification results. Firstly, we get the best C and g when we classify the bag with “excellent instance” by PSO algorithm. Then we use LO to get the final optimal SVM parameters. The process of LO is as follows.

The values of C generally focus on the scope of 25 to 27 in the bag with “excellent instance,” and g focus on the scope of 3 to 10. We choose one pair of the parameters, $C = 26.3635$ and $g = 5.0861$, as the initial parameters. Figure 9 shows the classification results with different values of C when g is 5.0861, and Figure 10 shows the classification results with different values of g when C is 26.8635.

In Figure 9, with the change of the value of C , the effect on ACC is not obvious, and the best C we choose is 26.8635. SPE and SEN are always one increased and another decreased, but they can achieve a better result relatively when ACC is the best.

In Figure 10, the value of C is 26.8635. When the value of g is increasing, ACC increases. When g is bigger than 6.9861, ACC decreases following the increasing of g . Thus, we obtain the best ACC when C is 26.8635 and g is 6.9861. Although SEN and SPE have some fluctuation, they achieve a satisfying result when ACC is the best.

3.3.4. Experimental Results by SVM-IOMIL with Different Classification Samples. The classification sample sets are liver cancer and normal liver, liver cancer and liver cyst cases, and liver cancer and liver cirrhosis, and we represent them by A, B, and C, respectively. The experimental results are shown in Figure 11.

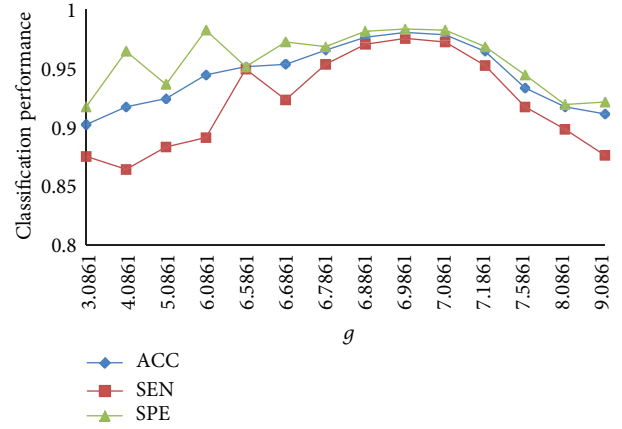
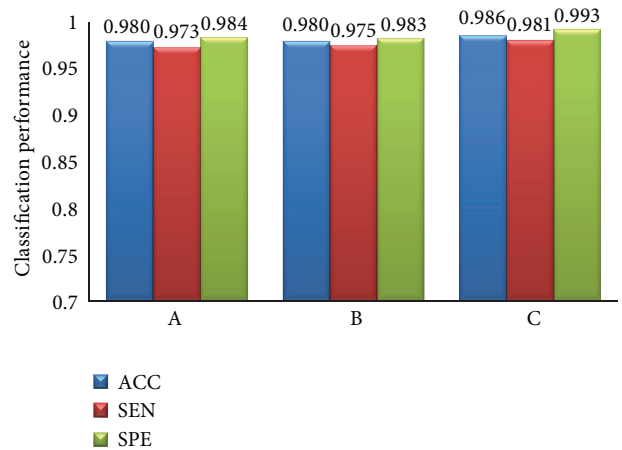
FIGURE 10: Classification results with different values of g .

FIGURE 11: Classification results with different samples.

As we can see in Figure 11, the proposed classification algorithm has generality. It has a high ACC, SEN, and SPE for the three different samples. The ACCs for the three different samples are all over 98%. And the inputting of experimental data and processing of the three experiments are similar, so PT and TT are the same for different samples.

3.3.5. Comparison between Our Algorithm and Other Algorithms. Several contrast experiments are carried out with the same feature data and different algorithms in this paper. The algorithms are Citation-kNN algorithm with minimum Hausdorff distance, the traditional SVM algorithm, WEMISVM algorithm, and our algorithm. The classification results of these algorithms are shown in Figures 12 and 13.

As Figure 12 shows, ACC, SEN, and SPE of our algorithm are higher than those of the other three algorithms obviously.

As for PT, the traditional SVM algorithm is much less than the other three algorithms. Citation-kNN algorithm, WEMISVM algorithm, and our algorithm are all MIL algorithms, while the SVM algorithm is a traditional single instance algorithm. The MIL algorithm needs to extract more instances, but the traditional algorithm needs one.

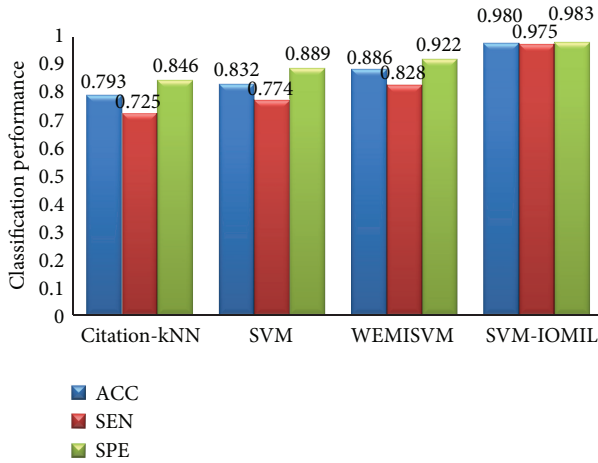


FIGURE 12: The classification efficiency comparison of four different algorithms.

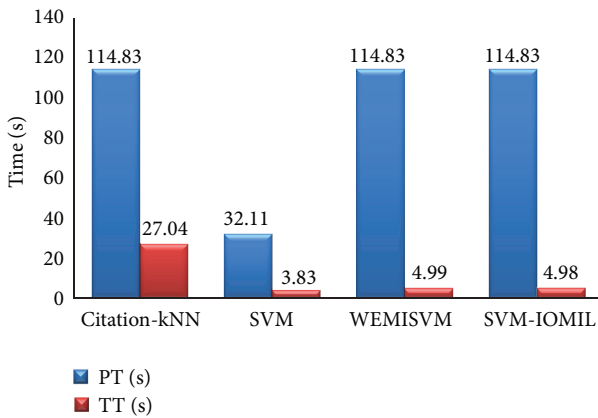


FIGURE 13: The time efficiency comparison of four different algorithms.

As a lazy learning algorithm, Citation-kNN algorithm needs to save the whole training set and go through the whole sample space when predicting, so it costs more time when classifying. The SVM algorithm, WEMISVM algorithm, and our algorithm benefit from the advantage of SVM, so they need less TT than Citation-kNN algorithm.

4. Conclusions

This paper proposed a novel MIL method to recognize liver cancer with abdominal CT images based on two-time instance optimization and CPSO-SVM. We eventually got three better classifiers to classify the liver cancer and the normal liver, the liver cancer and the liver cirrhosis, and liver cancer and the liver cyst. The proposed algorithm achieved a better classification accuracy and robustness of ROI segmentation. As the contrast experiments show, our method greatly improved the recognition accuracy for liver cancer. The instances are extracted equally based on the entire image, so our method can ignore the process of tumor region segmentation and lower the requirements of liver region

segmentation accuracy. However, the processing speed of our algorithm is lower than traditional SVM algorithm because our algorithm is a MIL algorithm. Obviously, MIL algorithm will extract features for more objects than the traditional single instance classification algorithm, so it certainly needs more time for image processing. This is also the main problem of MIL algorithm at present. Besides, our algorithm is only used in binary classification problems. In the future, we will explore some methods to reduce the time complexity of the MIL algorithm and come up with a new classification method to solve the multiclassification problems.

Acknowledgment

This research is supported by the National Natural Science Foundation of China (no. 60973071, and no. 61272176).

References

- [1] H. Fujita, Y. Uchiyama, T. Nakagawa et al., "Computer-aided diagnosis: the emerging of three CAD systems induced by Japanese health care needs," *Computer Methods and Programs in Biomedicine*, vol. 92, no. 3, pp. 238–248, 2008.
- [2] H. M. Taylor and P. R. Ros, "Hepatic imaging: an overview," *Radiologic Clinics of North America*, vol. 36, no. 2, pp. 237–245, 1998.
- [3] K.-H. Hwang, J. G. Lee, J. H. Kim et al., "Computer aided diagnosis (CAD) of breast mass on ultrasonography and scintimammography," in *Proceedings of the 7th International Workshop on Enterprise Networking and Computing in Healthcare Industry (HEALTHCOM '05)*, pp. 187–190, June 2005.
- [4] L. Fei-Fei, R. Fergus, and P. Perona, "Learning generative visual models from few training examples: an incremental Bayesian approach tested on 101 object categories," *Computer Vision and Image Understanding*, vol. 106, no. 1, pp. 59–70, 2007.
- [5] A. Bosch, A. Zisserman, and X. Munoz, "Representing shape with a spatial pyramid kernel," in *Proceedings of the 6th ACM International Conference on Image and Video Retrieval (CIVR '07)*, pp. 401–408, July 2007.
- [6] M. Varma and D. Ray, "Learning the discriminative power-invariance trade-off," in *Proceedings of the 11th International Conference on Computer Vision (ICCV '07)*, pp. 1–8, October 2007.
- [7] A. Opelt, M. Fussenegger, A. Pinz, and P. Auer, "Weak hypotheses and boosting for generic object detection and recognition," in *Proceedings of the IEEE International Conference on Computer Vision*, pp. 71–84, 2004.
- [8] X.-S. Xu, X. Xue, and Z.-H. Zhou, "Ensemble multi-instance multi-label learning approach for video annotation task," in *Proceedings of the 19th ACM International Conference on Multimedia ACM Multimedia (MM '11)*, pp. 1153–1156, December 2011.
- [9] Y. Shen and J.-P. Fan, "Multi-task multi-label multiple instance learning," *Journal of Zhejiang University C*, vol. 11, no. 11, pp. 860–871, 2010.
- [10] C. Hu, J. H. Huang, Y. T. Zhang, and X. L. Tang, "The application of multi-instance learning in multi-ROI breast tumor classification," *Intelligent Computer and Applications*, vol. 1, no. 1, pp. 66–73, 2011.

- [11] T. G. Dietterich, R. H. Lathrop, and T. Lozano-Pérez, "Solving the multiple-instance problem with axis-parallel rectangles," *Artificial Intelligence*, vol. 89, no. 1, pp. 31–71, 1997.
- [12] O. Maron and A. L. Ratan, "Multiple-instance learning for natural scene classification," in *Proceedings of the International Conference On Machine Learning (ICML '98)*, vol. 98, pp. 341–349, 1998.
- [13] Q. Zhang and S. A. Goldman, "EM-DD: an improved multiple-instance learning technique," in *Advances in Neural Information Processing Systems*, vol. 14, pp. 1073–1080, 2001.
- [14] J. Wang and J. D. Zucker, "Solving the multiple-instance problem: a lazy learning approach," in *Proceedings of the 17th International Conference on Machine Learning*, pp. 1119–1126, 2000.
- [15] S. Andrews, T. Hofmann, and I. Tsochantaris, "Multiple instance learning with generalized support vector machines," in *Proceedings of the 18th National Conference on Artificial Intelligence (AAAI '02)*, pp. 943–944, August 2002.
- [16] Y. Chen and J. Z. Wang, "Image categorization by learning and reasoning with regions," *The Journal of Machine Learning Research*, vol. 5, pp. 913–939, 2004.
- [17] Z.-H. Zhou and J.-M. Xu, "On the relation between multi-instance learning and semi-supervised learning," in *Proceedings of the 24th International Conference on Machine Learning (ICML '07)*, pp. 1167–1174, June 2007.
- [18] B. Huang, *Research and Application on Multi-Instance Learning Based on Support Vector Machine*, China University of Geosciences, 2009.
- [19] X. Pan and S. L. Zhang, "A novel parallelized remote sensing image SVM classifier algorithm," in *Proceedings of the 5th International Congress on Image and Signal Processing (CISP' 12)*, pp. 992–996, 2012.
- [20] V. Vapnik, *The Nature of Statistical Learning Theory*, Springer, 2nd edition, 2001.
- [21] T. Sirinya and S. Nobuhiko, "CT/US image registration using LS-SVM," in *Proceedings of the 4th International Conference on Intelligent Systems Modelling and Simulation (ISMS '13)*, pp. 258–263, 2013.

Research Article

Fast and Automatic Ultrasound Simulation from CT Images

Weijian Cong, Jian Yang, Yue Liu, and Yongtian Wang

Key Laboratory of Photoelectronic Imaging Technology and System of Ministry of Education of China, School of Optics and Electronics, Beijing Institute of Technology, Beijing 10081, China

Correspondence should be addressed to Jian Yang; jyang@bit.edu.cn

Received 17 July 2013; Accepted 28 August 2013

Academic Editor: Yunmei Chen

Copyright © 2013 Weijian Cong et al. This is an open access article distributed under the Creative Commons Attribution License, which permits unrestricted use, distribution, and reproduction in any medium, provided the original work is properly cited.

Ultrasound is currently widely used in clinical diagnosis because of its fast and safe imaging principles. As the anatomical structures present in an ultrasound image are not as clear as CT or MRI. Physicians usually need advance clinical knowledge and experience to distinguish diseased tissues. Fast simulation of ultrasound provides a cost-effective way for the training and correlation of ultrasound and the anatomic structures. In this paper, a novel method is proposed for fast simulation of ultrasound from a CT image. A multiscale method is developed to enhance tubular structures so as to simulate the blood flow. The acoustic response of common tissues is generated by weighted integration of adjacent regions on the ultrasound propagation path in the CT image, from which parameters, including attenuation, reflection, scattering, and noise, are estimated simultaneously. The thin-plate spline interpolation method is employed to transform the simulation image between polar and rectangular coordinate systems. The Kaiser window function is utilized to produce integration and radial blurring effects of multiple transducer elements. Experimental results show that the developed method is very fast and effective, allowing realistic ultrasound to be fast generated. Given that the developed method is fully automatic, it can be utilized for ultrasound guided navigation in clinical practice and for training purpose.

1. Introduction

The imaging principle behind an ultrasound is that the ultrasound wave generates a different amount of reflection or refraction when accounting for different tissues inside the human body. Given that the shape, density, and structure of different organs vary, the amounts of wavelets that are reflected or refracted can be used to reconstruct the anatomical structure of human tissues. Based on the wave pattern and image features, combined with personal anatomical and pathological knowledge, the texture and pathological characteristics of a specific organ can be quantified for medical professionals.

Over the past decades, the ultrasound imaging technique has played increasingly important role in clinical diagnosis. As a fast and safe method of imaging, ultrasound is the most ideal imaging modality for real-time image-guided navigation in minimally intrusive surgery [1–3]. However, the ultrasound image is usually mixed with a high level of noise and the anatomical structure is not as clear as that in CT and MRI [4]. Hence, a successful ultrasound doctor has

to possess a huge amount of anatomical knowledge, as well as considerable clinical experience. Currently, ultrasound clinical training is usually done under the guidance of experts who operate on real patients. Such training is time consuming and costly. Moreover, for some operations requiring careful manipulations, such as abscess drainage and tissue biopsy, incorrectly performed operations can cause great suffering to the patient or even lead to a number of complications. Comparably, the ultrasound simulation technique provides an economic and efficient way of observing and acquiring ultrasound images [5–7].

Currently, two categories of ultrasound simulation methods exist. The first involves the 3D ultrasound volume generated by a series of 2D ultrasound images, wherein the section slices of ultrasound images are generated from the location and direction of the ultrasound detector. Henry et al. [8] constructed the ultrasound volume from real images of a typical patient in offline preprocessing. The ultrasound image is then generated by considering both the position of the virtual probe and the pressure applied by this probe on the body. The system was successfully used to train physicians

to detect deep venous thrombosis of the lower limbs. Weidenbach et al. [9] calculated a 2D echocardiographic image from preobtained 3D echocardiographic datasets that are registered with the heart model to achieve spatial and temporal congruency. The displayed 2D echocardiographic image is defined and controlled by the orientation of the virtual scan plane. Such a simulation method requires the 3D ultrasound volume data to be acquired in advance, thus guaranteeing good image quality and high-speed scanning of the image slice. However, this method cannot simulate the image outside the 3D volume data and 3D ultrasound images are also quite difficult to obtain using general ultrasound devices.

The second method involves the ultrasound being simulated from volume data, such as CT or MRI images. Shams et al. [10] simulated ultrasound images from 3D CT scans by breaking down computations into a preprocessing and a run-time phase. The preprocessing phase generates fixed-view 3D scattering images, whereas the run-time phase calculates view-dependent ultrasonic artifacts for a given aperture geometry and position within a volume of interest. Based on the method of Shams, Kutter et al. [11] used a ray-based model combined with speckle patterns derived from a preprocessed CT image to generate view-dependent ultrasonic effects, such as occlusions, large-scale reflections, and attenuation. In his method, Graphics Processing Unit (GPU) was introduced for speed acceleration. Reichl et al. [12] estimated ultrasound reflection properties of tissues and modified them into a more computationally efficient form. In addition, they provided a physically plausible simulation of ultrasound reflection, shadowing artifacts, speckle noise, and radial blurring. Compared with the ultrasound volume-based method, the source image is easy to obtain and the calculation is comparably robust for the CT- and MRI-based method [13]. However, given that the imaging principles are totally different for CT, MRI, and ultrasound, such kind of simulation is more complicated than the ultrasound volume-based method. Moreover, the method is time consuming during preprocessing and intensity calculations. On the other hand, the CT- and MRI-based method can conveniently obtain the ultrasound image at any angle and position and the simulated ultrasound can also be fused with the CT or MRI. Hence, the CT- and MRI-based method can provide a more comprehensive understanding of diseases.

In this paper, a novel method is developed for the simulation of an ultrasound image from CT volume datasets. A multiscale method is proposed to simulate blood flow and to enhance tubular structures in the CT image [14]. The thin-plate spline [15–17] interpolation method is utilized to transform images between the sector and rectangle diagram. Differences of adjacent regions in terms of radiation are subjected to weighted integration in the CT image to obtain a realistic simulation of the acoustic response of common tissues. Finally, based on reflection and attenuation principles of ultrasound, the Kaiser window function [18] is used to overlay simulated images from different transducer elements and the rectangular diagram is mapped into the sector diagram to guarantee a simulated ultrasound image with high validity and calculation speed.

The advantages of our algorithm are twofold: first, as the tubular structures in the CT image are strengthened by the multiscale enhancement method, the simulated vessel in the ultrasound is more realistic than the commonly used method. Second, as the response coefficient of ultrasound is calculated by the intensity differences of adjacent regions in the ultrasound propagation path, the complexity of the simulation procedure is greatly reduced.

2. Method

The developed method comprises the following four main parts.

- (1) *Multiscale Vascular Enhancement*. In this part, a multiscale method is employed to enhance tubular structures in the CT volume data. Through this process, the intensities unlikely to belong to vascular trees are effectively removed. The output image then used for following processing is a weighted integration of the source and the enhanced images.
- (2) *Thin-Plate Spline Mapping*. As ultrasound is generally presented as a sector diagram with a coordinate system that is different from the rectangular coordinate used for CT images, the thin-plate spline interpolation method is used for the transformation between sector and rectangular diagrams to achieve smooth mapping of both the diagrams.
- (3) *Acoustic Model Construction*. In this part, the acoustic model is constructed via the weighted function of adjacent regions on the ultrasound propagation path.
- (4) *Kaiser Window Analysis*. The ultrasound emitter is generally composed of multiple transducer elements. The Kaiser window filter is utilized to obtain a realistic simulation effect and to simulate fusion effects of all independent elements. In order to guarantee the clarity of the simulated ultrasound, a linear scaling method is applied to the final results to stretch the ultrasound intensity to a scale level of 256. The processing flow diagram is shown in Figure 1.

(1) *Multiscale Vascular Enhancement*. When there is relative motion between the ultrasound source and the receiving body, the received signal frequency will be changed from the actual frequency transmitted from the source. Therefore, the vessels can be clearly imaged in ultrasound. For any CT image, the difference of CT values for vasculature and its neighboring tissues is almost negligible as no material is perfused in the focused part of the vasculature to enhance its visibility and subside the neighboring vessels as background during the whole procedure. Thus, it causes great difficulty in distinguishing the vasculature to be focused on and the neighboring tissues to be removed. Therefore, direct simulation of an ultrasound sector from a CT image cannot achieve realistic blood vessel visualization. In this paper, we utilize the multiscale enhancement method developed in [19] to strengthen vasculatures and then, by calculating intensity difference between adjacent voxels in the ultrasound propagation path, the response coefficient can be quantified.

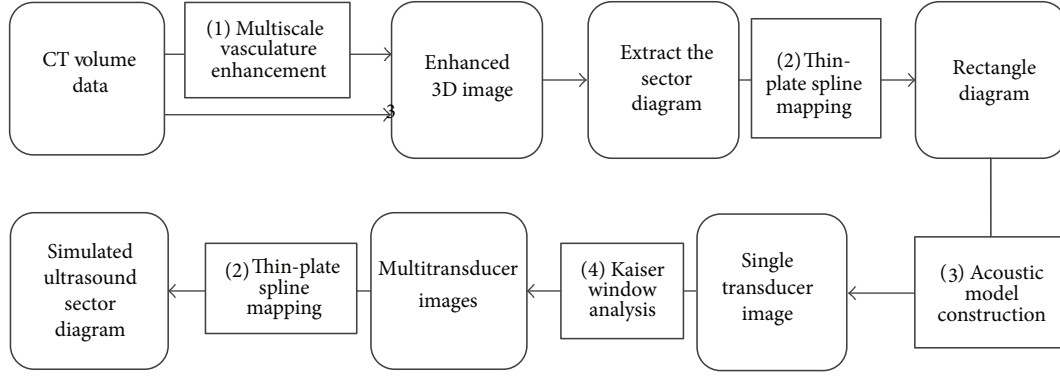


FIGURE 1: Simulation procedures and calculation modules.

The multiscale enhancement approach basically filters the tube like geometrical structures. Since there is a large variation in size of the vessels, so we need to define a measurement scale with a certain range. Basically to examine the local behavior of an image, L , its Taylor expansion in the neighborhood of a point x_0 can be shown as

$$L(x_0 + \delta x_0, s) \approx L(x_0, s) + \delta x_0^T \nabla_{0,s} + \delta x_0^T H_{0,s} \delta x_0, \quad (1)$$

where $\nabla_{0,s}$ and $H_{0,s}$ are the gradient vector and Hessian matrix of the image computed in x_0 at scale s . To calculate these differential operators of L , we use the concepts of linear scale space theory. Here the differentiation is defined as a convolution with derivatives of Gaussians as

$$\frac{\partial}{\partial x} L(x, s) = s^\gamma L(x) * \frac{\partial}{\partial x} G(x, s), \quad (2)$$

where the D -dimensional Gaussian is defined as

$$G(x, s) = \frac{1}{\sqrt{2\pi s^2}^D} e^{-\|x\|^2/2s^2}. \quad (3)$$

The parameter γ defines a family of normalized derivatives and helps in unbiased comparison of response of differential operators at various scales.

The idea behind eigenvalue evaluation of the Hessian is to extract the principal directions in which the local second order structure of the image can be decomposed. Three orthonormal directions are extracted by eigenvalue decomposition that is invariant up to a scaling factor when mapped by the Hessian matrix. Let λ_k be the eigenvalue with the k th smallest magnitude. In particular, a pixel belonging to a vessel region will be denoted by λ_1 being small (ideally zero), λ_2 and λ_3 for a large magnitude and equal sign (the sign states the brightness or darkness of the pixel). To conclude, for an ideal tubular structure in a 3D image as

$$|\lambda_1| \approx 0 \quad |\lambda_1| \ll |\lambda_2| \quad \lambda_2 \approx \lambda_3. \quad (4)$$

The polarity is indicated by signs of λ_2 and λ_3 . In regions with high contrast compared to the background, the norm will become larger since at least one of the eigenvalues will

be large. The following combination of the components can define a vesselness function:

$$v_0(s) = \begin{cases} 0, & \lambda_2 > 0 \text{ or } \lambda_3 > 0 \\ \left(1 - \exp\left(-\frac{\mathfrak{R}_A^2}{2\alpha^2}\right)\right) \\ \quad \times \exp\left(-\frac{\mathfrak{R}_B^2}{2\beta^2}\right) \\ \quad \times \left(1 - \exp\left(-\frac{S^2}{2c^2}\right)\right), & \text{otherwise,} \end{cases} \quad (5)$$

where α , β , and c are thresholds which control the sensitivity of the line filter to the measures \mathfrak{R}_A , \mathfrak{R}_B , and s . The vesselness measure is analyzed at different scales, s . For 2D images, we propose the following vesselness measure which follows from the same reasoning as in 3D:

$$v_0(s) = \begin{cases} 0, & \lambda_2 > 0 \\ \exp\left(-\frac{\mathfrak{R}_B^2}{2\beta^2}\right) \left(1 - \exp\left(-\frac{S^2}{2c^2}\right)\right), & \text{otherwise,} \end{cases} \quad (6)$$

where $\mathfrak{R}_B = \lambda_1/\lambda_2$ is the boldness measure in 2D and accounts for the eccentricity of the second-order ellipse.

(2) *Thin-Plate Spline Mapping*. As ultrasound and CT images are present as polar and rectangular coordinate systems, respectively, transformation between these two diagrams is necessary for the simulation processing. In this paper, the thin-plate spline interpolation method is utilized to achieve these transformations.

The basic idea of the thin-plate spline is that a space transformation can be decomposed into a global affine transformation and a local nonaffine warping component [20]. Assuming that we have two sets of corresponding points

p_i and $q_i, i = 0, 1, \dots, n$, then, the energy function of the thin-plate spline can be defined as

$$E_{\text{TPS}}(f) = \sum_{i=1}^n \|p_i - f(q_i)\|^2 + \lambda \iint \left[\left(\frac{\partial^2 f}{\partial x^2} \right)^2 + 2 \left(\frac{\partial^2 f}{\partial x \partial y} \right)^2 + \left(\frac{\partial^2 f}{\partial y^2} \right)^2 \right] dx dy, \quad (7)$$

where f is mapping function between point sets p_i and q_i . The first term in the previous equation is the approaching probability between these two point sets, whereas the second term is a smoothness constraint, while λ indicates a different degree of warping. When λ is close to zero, corresponding points are matched exactly. For this energy function, a minimizing term $f(q), q \in R^2$ exists for any fixed λ , which can be formulated as:

$$f(q) = q \cdot A + \varphi(q) \cdot W, \quad (8)$$

where A is a 3×3 affine transformation matrix and $\varphi(q)$ is a $1 \times n$ vector decided by the spline kernel, while W is a $n \times 3$ non-affine warping matrix. When we combine (7) and (8), we have

$$E_{\text{TPS}}(A, W) = \|U - V \cdot A - \Psi W\|^2 + \lambda \text{trace}(W^T \Psi W) dx dy, \quad (9)$$

where U and V are concatenated point sets of p and q and Ψ is a $n \times n$ matrix formed from the $\varphi(q)$. Thus, QR decomposition can be utilized to separate the affine and non-affine warping space as follows:

$$M = [Q_1 Q_2] \begin{pmatrix} R_1 \\ 0 \end{pmatrix} = Q_1 R_1, \quad (10)$$

where M is a $m \times n$ matrix with $m \geq n$, Q_1 is a $m \times n$ matrix, Q_2 is $m \times (m-n)$ matrix, and Q_1 and Q_2 both have orthogonal columns, whereas R_1 is an $n \times n$ upper triangular matrix. The final solution for A and W can be obtained as

$$W = Q_2 (Q_2^T \Psi Q_2 + \lambda I_{(N-3)})^{-1} Q_2^T U, \quad (11)$$

$$A = R^{-1} (Q_2^T V - \Psi W).$$

Through thin-plate spline interpolation, the transformation between the polar and rectangular coordinate systems can be achieved. Although the thin-plate spline method is, to an extent, time consuming compared to the commonly used bilinear or trilinear interpolation methods, however, it guarantees comparative homogeneity in both radial and tangential directions. One common problem for the nonparametric mapping between polar and rectangular coordinate systems is that the resolution in tangential direction is homogeneous while it is reducing gradually radial direction

from the center to the out part of the sector. The main merit of the proposed thin-plate spline mapping method is that it can keep maximum uniformity of the whole diagram.

Figure 2 shows the mapping principle between sector and rectangle. The ultrasound image is generally presented as sector, as shown in Figure 2(a), and the intersection angle ϕ is defined as Field of View (FOV) which is usually set as constant once the device is calibrated. The penetration depth of the ultrasound can be defined as the in-depth distance between inner and outer circles with radius of r_l and r_s , which is determined by the strength of acoustic wave. Figure 2(b) shows the rectangle image section extracted from the CT image. In this figure, $\{a_{1,2}, a_{2,2}, \dots, a_{m,2}\}$ and $\{A_{1,2}, A_{2,2}, \dots, A_{m,2}\}$ are the constructed correspondences and m and n represent the number of sampling along radial and tangential directions. It is obvious that resolution of the simulated ultrasound is determined by $m \times n$.

(3) *Acoustic Model for Construction.* Large differences are observed in the acoustic resistances between different tissues. Thus, an ultrasound at interfaces of different tissues usually results in the occurrence of reflection, refraction, and absorption. If the resistance difference between two tissues is greater than 0.1%, the reflection will be produced [21]. The acoustic resistance Z of a certain organ can be calculated as $Z = \rho c$, where ρ is density and c represents propagation speed of the ultrasound.

The reflection coefficient α_{ref} and transmission coefficient α_{tran} on the interface of two organs with acoustic resistance of Z_1 and Z_2 can be calculated by the following equations [22]:

$$\alpha_{\text{ref}}(Z_1, Z_2) = \frac{U_{\text{ref}}}{U} = \left(\frac{Z_2 - Z_1}{Z_2 + Z_1} \right)^2,$$

$$\alpha_{\text{tran}}(Z_1, Z_2) = \frac{U_{\text{tran}}}{U} = \frac{4Z_1 Z_2}{(Z_1 + Z_2)^2} = 1 - \alpha_{\text{ref}}(Z_1, Z_2), \quad (12)$$

where U , U_{ref} , and U_{tran} are wave intensities of input ultrasound, reflected ultrasound, and transmitted ultrasound, respectively.

The reflection is generally produced on the interfaces of two organs. Hence, edge detection is imperative for acquiring boundary information. Currently, several stable edge detection methods exist, such as Roberts, Sobel, Prewitt, and LOG operators, which have been widely used in medical image processing. For these methods, the detection of the edge is based on the analysis of the intensity relationship of neighboring points. Moreover, if a certain angle exists between the propagation and edge directions, reflection will occur. If the propagation direction is parallel to the edge direction, the ultrasound will transmit directly, and no reflection occurs. Hence, the propagation angle must be considered in the calculation of the acoustic response.

However, a considerable amount of random speckles occur in the ultrasound image, and the correct noise generation is important for the realistic simulation of ultrasound images. When the scatter phenomenon of ultrasound is produced inside the human body, the backwaves with different

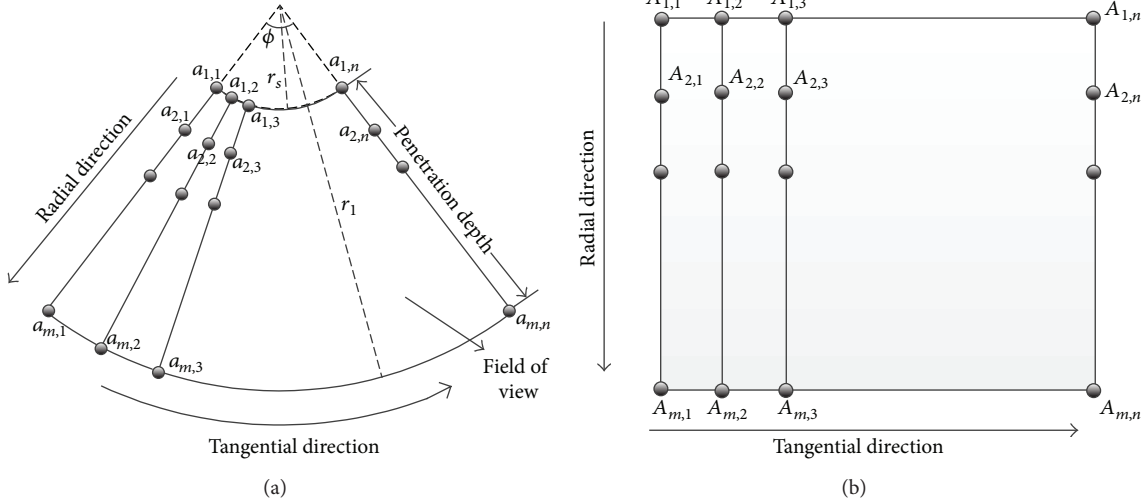


FIGURE 2: Relationship between sector and rectangle mapping.

phases generally interfere with one another. Hence, speckles are generated [23, 24]. Random noises are generated and superimposed onto the simulated image. As for the CT image, several factors, including amount of radiation, performance of data acquisition unit, and image reconstruction procedure, can also introduce noise in the simulated ultrasound [24].

Intensity differences of adjacent regions are used for the calculation of the response coefficient to obtain a realistic simulation of ultrasound. Specifically, the response coefficient of a certain region is determined by consecutive regions on the ultrasound propagation direction. The following three conditions have to be considered.

- (1) Adjacent regions are not on the interface. For such a condition, the calculation sample point is inside the same organ. Hence, the difference in the CT values of these two regions is small, yielding a small response coefficient.
- (2) Adjacent regions are on the edge of the interface. If the propagation direction is parallel to the edge direction, the adjacent regions will both be located on the edge, thus yielding small CT value variations. If the angle between the propagation and edge directions increases gradually, the CT value variation will increase and consequently increase the response coefficient. By this method, the interface effect of the response coefficient can be calculated only by adjacent regions, and the imaging angle between edge and ultrasound propagation directions need not be calculated.
- (3) Adjacent regions are on the noise area. In such situations, the difference in the CT values is usually large, thus yielding a large response coefficient. Therefore, the noises of the ultrasound can be simulated by the intensity difference in the CT image.

Acoustic resistance is generally known to be proportional to the CT value [25]. Hence, the weight α_{ref} of adjacent regions $I(x_1)$ and $I(x_2)$ can be written as

$$\alpha_{\text{ref}} = \left(\frac{I(x_2) - I(x_1)}{I(x_2) + I(x_1)} \right)^2. \quad (13)$$

However, bone-tissue interfaces reflect 43% and air-tissue interfaces reflect 99% of the incident beam [26]. Hence, (13) cannot be applied to tissues like bone and air.

(4) *Kaiser Window Analysis*. For the acoustic response model, the strength of sound wave increases with the decrease of the angle θ between incident sound wave and surface normal at the interface, as can be shown by the Lambert cosine law [27] as follows:

$$U_{\text{out}}(\theta) = \alpha_{\text{ref}} \times U_{\text{in}} \times \cos(\theta), \quad (14)$$

where U_{in} and U_{out} represent acoustic intensities before and after refraction at the medium interface. α_{ref} represents the reflection coefficient and θ represents the intersection angle between input ultrasound and normal vector of the interface. When ultrasound is transmitted in the media, its energy decreases with the propagation distance. Such phenomenon is called ultrasound attenuation. As for ultrasound wave with given frequency, its energy attenuation follows the power law principle, which can be formulated as [28]

$$U(\alpha_{\text{ref}}, d) = U_{\text{in}} \times e^{-2\alpha_{\text{ref}}d}, \quad (15)$$

where d is the propagation distance, while $U(\alpha_{\text{ref}}, d)$ represents the acoustic intensity after it has been propagated in the medium for a distance of d . According to the Lambert cosine law, the intensity of the acoustic response can be calculated as

$$U_{\text{out}}(\theta) = \alpha_{\text{ref}} \times U_{\text{in}} \times \cos(\theta) = \alpha_{\text{ref}} \times U_{\text{in}} \times \left| \vec{r}(x) \cdot \vec{n}(x) \right|, \quad (16)$$

where $\vec{r}(x)$ is the unit vector in the direction of the ultrasound beam, $\vec{n}(x)$ is the surface normal at the interface, $|\cdot|$ is the absolute value operator. Then, the attenuation of the ultrasound can be obtained by the following equation:

$$U_{\text{out}}(\alpha_{\text{ref}}, d, \theta) = \alpha_{\text{ref}} \times U_{\text{in}} \times |\vec{r}(x) \cdot \vec{n}(x)| \times e^{-2\alpha_{\text{ref}}d}. \quad (17)$$

Suppose that multiple independent transducer elements are observed and the strength of each ultrasound is U_0 . The summary of the received ultrasound strength can be calculated as follows:

$$\begin{aligned} U_{\text{total}} &= \sum_{i=1}^n U_i = \sum_{i=1}^n \alpha_{\text{ref}} \times U_{\text{in}} \times |r(x) \cdot n(x)| \times e^{-2\alpha_{\text{ref}}d} \\ &= \sum_{i=1}^n \alpha_{\text{ref}} \times U_{\text{in}} \times \cos(\theta_i) \times e^{-2\alpha_{\text{ref}}(d_0/\cos(\theta_i))}, \end{aligned} \quad (18)$$

where d_0 is the minimum distance among all the transducer element and sampling region x_i , and d is the distance interval of adjacent transducer elements. Meanwhile, θ_i is the angle between transducer element and the sampling region x_i , which can be written as

$$\theta_i = \arctan\left(\frac{n \times d}{d_0}\right), \quad (19)$$

where n is the number of active elements of transducer and ω_i can be parameterized as $\omega_i = \cos(\theta_i) \times e^{-2\alpha_{\text{ref}}(d_0/\cos(\theta_i))}$, which can be calculated by Kaiser window. The discrete probability density of Kaiser Window can be written as

$$\omega(m) = \begin{cases} I_0 \times \left(\pi \alpha \sqrt{1 - \left(\frac{2m}{M} - 1 \right)^2} \right), & 0 \leq m \leq M \\ 0, & \text{otherwise,} \end{cases} \quad (20)$$

where I_0 represents the first zero-order modified Bessel function and α is the parameter to determine shape of the window, while M is an integer with length of $(N + 1)$.

3. Experimental Results

The developed method is applied to a series of CT images obtained from PLA General Hospital to investigate the performance and accuracy of the proposed simulation algorithm. The images were acquired from a 64-slice CT scanner by Philips, and the resolution is $512 \times 512 \times 394$. The algorithm is implemented in the C++ programming language.

3.1. Evaluation of Multiscale Enhancement. Figure 3 shows the effectiveness of the ultrasound simulation with multiscale enhancement, which is compared with the direct simulation of the CT image. Figure 3(a1) is the volume rendering of the original image. The gray scales of vascular trees are very close to their surrounding tissues, especially for small vessel segments and bones. If ultrasound is directly simulated from this image, vessels will mix with the neighboring tissues

and will be difficult to detect visually. Figure 3(b1) is the volume rendering of the vascular structure processed by the multiscale enhancement method. The vascular structures are effectively extracted from which small vessel segments can be visually inspected. Figure 3(c1) is the superimposing of the original image and the enhanced vascular structure. Evidently, the vascular trees are effectively strengthened, and they can easily be separated from the surrounding tissues. Moreover, the vascular structures can be distinguished from bones.

Figures 3(a2), 3(b2), and 3(c2) are selected section slices in the transverse direction of the original CT image, which correspond to Figures 3(a1), 3(b1), and 3(c1), respectively. Figure 3(a3) is the direct simulation result of Figure 3(a1), whereas Figure 3(c3) is the simulation result of the enhanced image in Figure 3(c1). Based on Figure 3(a2), large vascular segments and the liver have comparatively higher gray scales than their neighboring tissues, and small vessels in the liver boundaries mix with liver tissues. If the ultrasound image is directly simulated from this image, such an intensity distribution can result in a large deviation the blood flow. In Figure 3(c2), the vasculatures are filled with low intensity values, which are shown as back circle areas compared with Figure 3(c1). Figures 3(a3) and 3(c3) show the simulated results of Figures 3(a2) and 3(c2), respectively, whereas Figures 3(a3)(1), 3(c3)(1), 3(a3)(2), and 3(c3)(2) show two magnified regions of interest corresponding to the same location in Figures 3(a2) and 3(c2). Evidently, blood vessels are effectively enhanced in Figure 3(c3), which are very close to the real ultrasound images.

Figure 4 shows a comparison of simulated ultrasound images of direct simulation and multiscale enhanced simulation. Figure 4(a) is the direct simulated ultrasound, whereas Figure 4(b) is the simulated result with multiscale enhancement. Vascular structures are clearly enhanced in Figure 4(b), which are presented as a black hole in the image, and the size of the hole indicates the dimension of the vasculature. The details of the enhanced ultrasound image are also clearer than those of the direct simulated image. Figures 4(a1) and 4(b1) show the magnified details of the rectangle strip in Figures 4(a) and 4(b), respectively. Based on the ellipse areas shown in this figure, the differences between these two figures can be clearly observed. Figure 4(c) shows the intensity distribution of the selected strips of Figures 4(a) and 4(b) in the horizontal direction. The intensity difference of these two images reaches nearly 35 gray scale levels, and the location of the maximum exactly corresponds to that of the vascular structures on the x -axis. Clearly, direct use of the CT image as a scattering map results in a repetitive scattering pattern through which hardly any structures are recognizable. However, the tubular structure enhancement method can effectively strengthen vascular structures, and a realistic acoustic transmission pattern is simulated and visualized.

3.2. Multiple Transducer Elements Simulation. The reflected signals of ultrasound are integrated along the active wavefront at a specified depth controlled by the Kaiser window function, which results in a more realistic reflection.

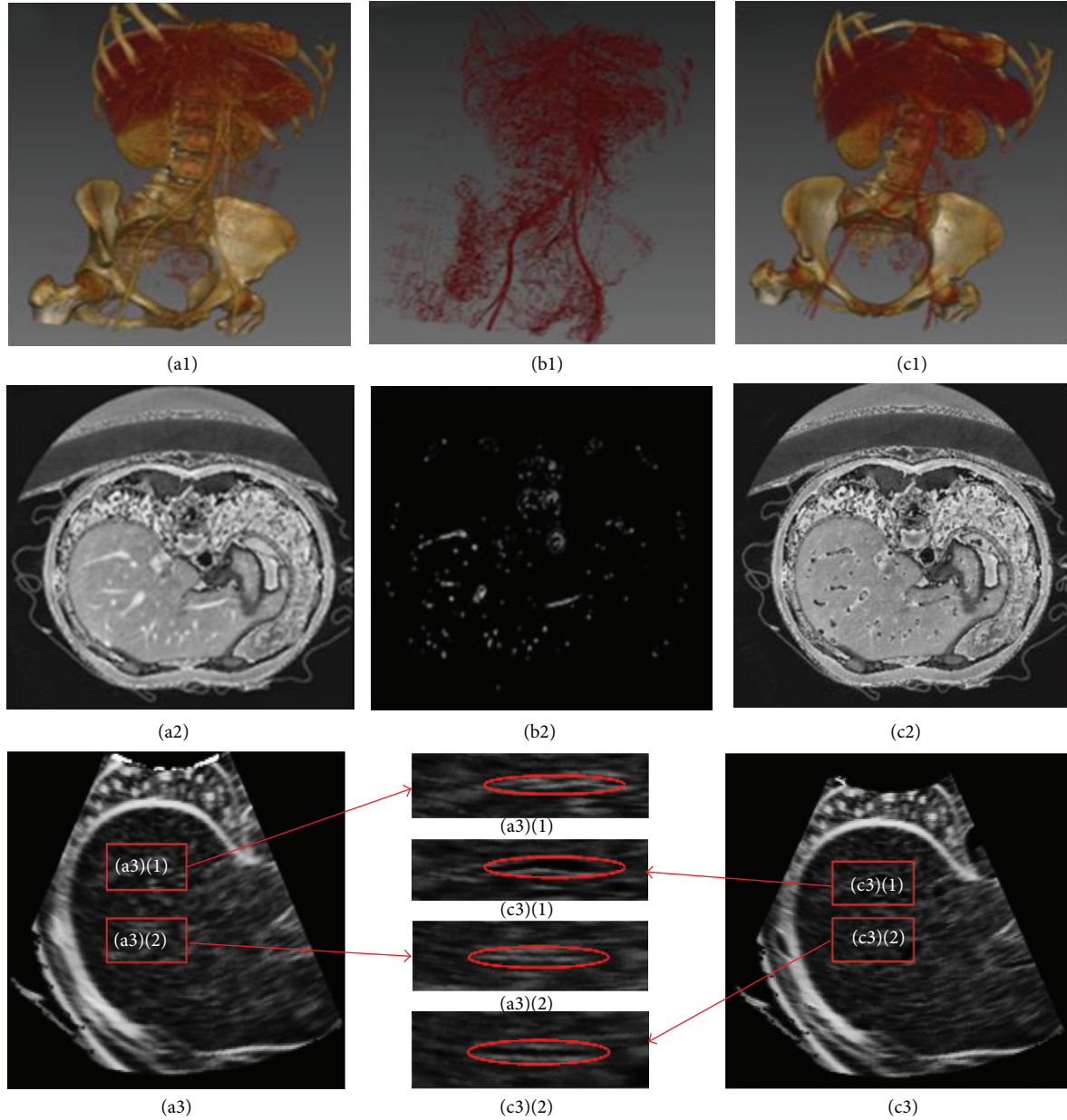


FIGURE 3: Comparison of different ultrasound simulation methods. The first row shows volume rendering of the original CT image, the extracted vascular structure, and the enhanced image, respectively. The second row shows selected liver section in transverse direction of the original CT image, the extracted vascular structure, and the enhanced image, respectively. (a3) and (c3) in the third row show simulated results of (a2) and (c2), respectively, while the middle image in the third row shows two magnified regions of interest corresponding to the same locations in (a2) and (c2).

Figure 5 shows the evaluation results of the multiple transducer element simulation. Figure 5(a) shows an extracted sector section of the CT image, Figure 5(b) gives the rectangle section image transformed by the thin-plate spline, and Figure 5(c) is the simulated ultrasound with one active element based on the acoustic transmission model, whereas Figure 5(d) is the simulated result with multiple active elements using the Kaiser window function. Figures 5(e1) and 5(e2) show two magnified regions of interest in Figure 5(e).

The thin-plate spline is very effective for the transformation of images between sector and rectangular shapes,

for which smooth warping is achieved. Moreover, the highly reflective areas in the ultrasound are located around the boundary of tissues. The vasculatures can be easily identified in both ultrasounds with single Figure 5(c) and multiple Figure 5(d) transducer elements. The difference between Figures 5(c) and 5(d) is that the edges between tissue boundaries of Figure 5(c) are significantly clearer than those of Figure 5(d). The realistic ultrasound is achieved by multiple transducer element simulation. From Figures 5(e1) and 5(e2), the vascular structures in the liver can be identified explicitly.

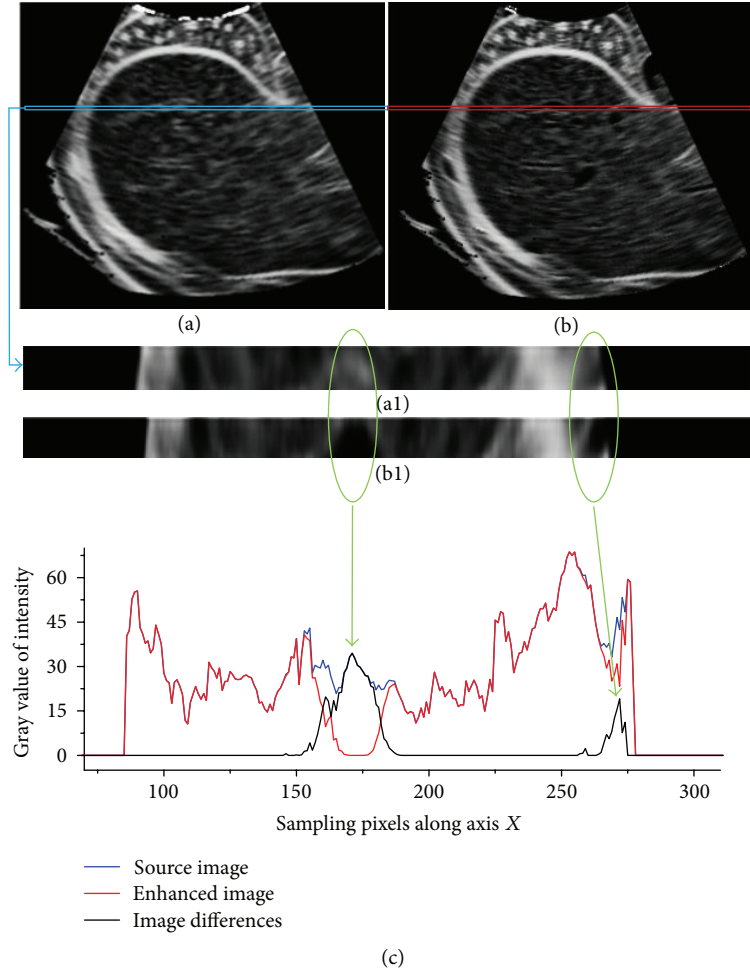


FIGURE 4: Comparison of simulated ultrasound images using direct simulation and multiscale enhancement method. (a) is the directly simulated ultrasound; (b) is the simulated result with multiscale enhancement. (a1) and (b1) show the magnified details of the rectangle strip in (a) and (b), respectively. (c) shows the intensity distribution in horizontal direction.

3.3. Evaluation of Ultrasound Simulation. Although a series of calculations has been applied for the simulation of ultrasound, image generation is still very efficient in terms of computation. The calculation complexity of the proposed method is decided by the sampling rate along radial and tangential directions, and it is not correlated to the FOV and the penetration depth. In order to evaluate the efficiency of the proposed method, three low cost personal PCs with different processing capacity are employed to simulate ultrasound with different sampling rates. The sampling rates are taken as 150×100 , 200×150 , 300×200 , 350×250 , 400×300 , 450×350 , 500×400 , 550×450 , and 600×500 , while the processing platforms are as follows:

- (a) Intel Core i5-2410 4 \times 2.3 GHz, 8 G RAM, Ubuntu 12.10 (64-bit),
- (b) Intel Core i7-860 4 \times 2.8 GHz, 8 G RAM, Ubuntu 12.10 (64-bit),
- (c) Intel Core i7-2600 4 \times 3.4 GHz, 8 G RAM, Ubuntu 12.10 (64-bit).

Figure 6 compares the calculation of the frame rate of the above mentioned platforms and sampling rates. It can be seen that the calculation efficiency is reducing gradually with the increase in the sampling rate for all the platforms. When the sampling rate is 200×100 , the calculation frame rates reaches about 42.2, 37.9, and 33.8 fps; however, when the sampling rate is about 600×500 , the calculation frame rates are about 11.4, 10.5, and 9.6 fps. It is obvious that high performance PC can obtain fast simulation speeds.

In order to investigate the performance of the proposed ultrasound simulation algorithm, it is applied to the realistic brain phantom created from polyvinyl alcohol cryogel (PVA-C) by Chen et al. [28]. PVA-C is a material widely used in validation of image processing methods for its mechanical similarities to soft tissues. The phantom was cast into a mold designed using the left hemisphere of the Colin27 brain dataset and contains deep sulci, a complete insular region, and an anatomically accurate left ventricle. The author released the CT, MRI, and ultrasound images of the phantom. All the volume data is with the size of $339 \times 299 \times 115$, and

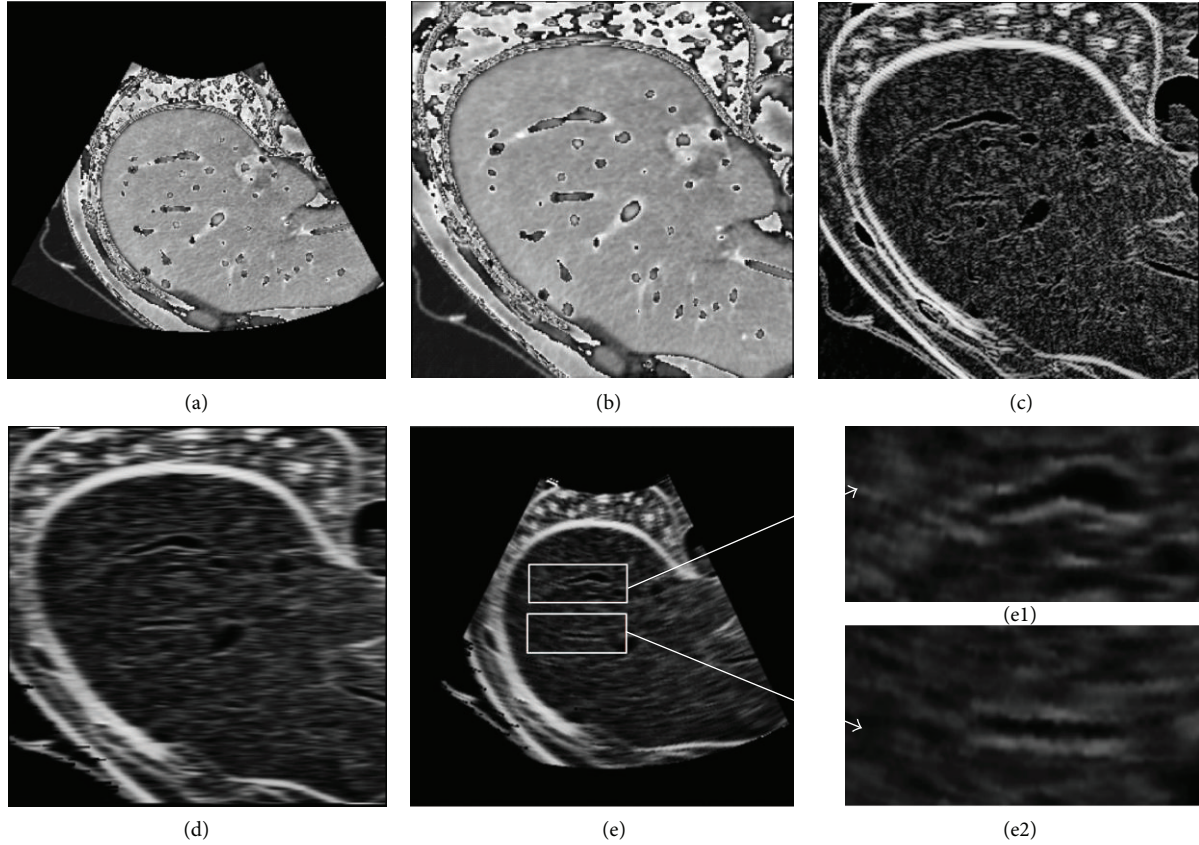


FIGURE 5: Evaluation results of multiple transducer elements simulation. (a) is the extracted sector section of the CT image. (b) is the rectangle mapping of (a). (c) is the simulated ultrasound of single transducer element. (d) is the simulated ultrasound of multiple transducer elements. (e) is the sector mapping of (d). (e1) and (e2) are the magnified regions of interest in (e).

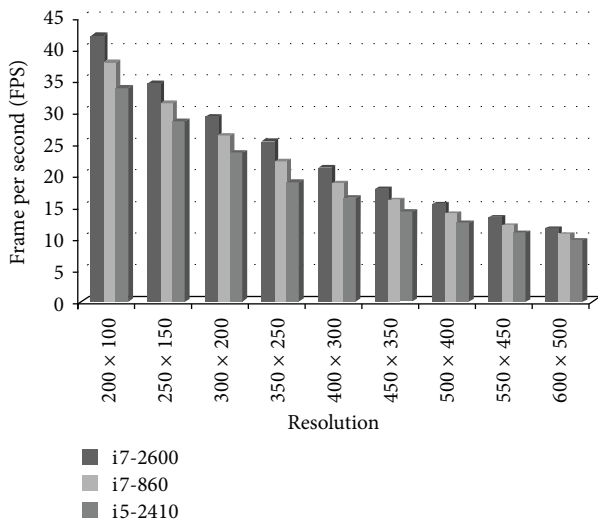


FIGURE 6: Comparison of the simulation speeds on different processing platforms.

corresponding imaging angles of ultrasound. As ultrasound and the CT images from the same imaging view can be obtained simultaneously, the fidelity of the proposed algorithm can be effectively evaluated by comparing the simulated

ultrasound with the corresponding phantom. Figure 7(a) provides photos of the elastic Colin27 based brain phantom mold and the PVA-C phantom. Figure 7(b) gives the volume rendering of the CT image of the phantom. Figures 7(c1) to 7(c4) give the CT image slice from two different angles, while Figures 7(d1)–7(d4) provide the realistic ultrasound image of the phantom corresponding to the CT image slices. Figures 7(e1)–7(e4) give the simulation results of the CT slices by the algorithm proposed in this paper. It can be seen that our method is very effective, which obtained realistic simulation of the ultrasound image.

3.4. Visualization System. In this paper, an application system is developed for displaying the simulated ultrasound in 2D and 3D using different visualization techniques. Figure 8 shows the screen shot of the visualization area of the developed system. The three leftmost images in this figure illustrate the axial plane in Figure 8(a), coronal plane in Figure 8(b), and sagittal plane in Figure 8(c) on the normal direction of the ultrasound transducer. The top right figure shows the volume rendering of the original CT image in Figure 8(d), whereas Figure 8(e) shows the extracted section plane of the CT image, and Figure 8(f) is the simulated ultrasound. Based on this system, the ultrasound image is generated according to the location and direction of the transducer.

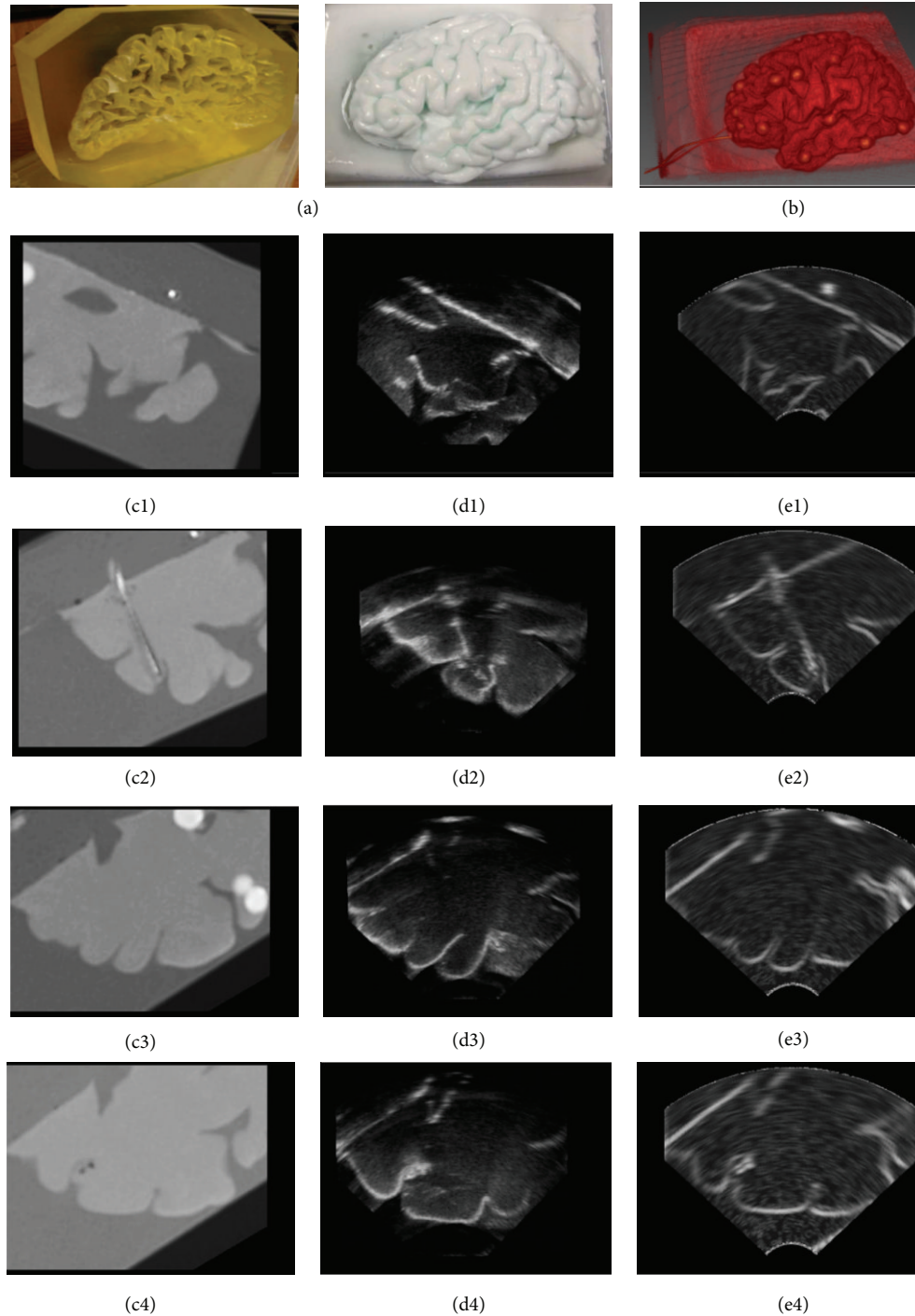


FIGURE 7: Evaluation of simulated ultrasound on phantom images. (a) Photos of the phantom. (b) Volume rendering of the CT image. ((c1)–(c4)) CT slices. ((d1)–(d4)) Ultrasound slices. ((e1)–(e4)) Simulated ultrasound sections corresponding to the CT slices.

The ultrasound and volume rendering of the CT image can be displayed with the three orthographic views of the CT image. Based on this system, the ultrasound image is fast generated, and the parameters, including ultrasound simulation and visualization, can be adjusted from user interface interaction.

The developed simulation system comprises four main visualization function modules, as follows. (1) The position

and orientation of the virtual probe can be interactively set by dragging the mouse in the 3D or the three orthogonal views, whereas the FOV, minimum, and maximum PD can be adjusted in the control panel. (2) The transparency and color mapping of volume rendering can be adjusted by controlling the multipoint thresholds on the histogram distribution. (3) The window level and window width for the CT slice in

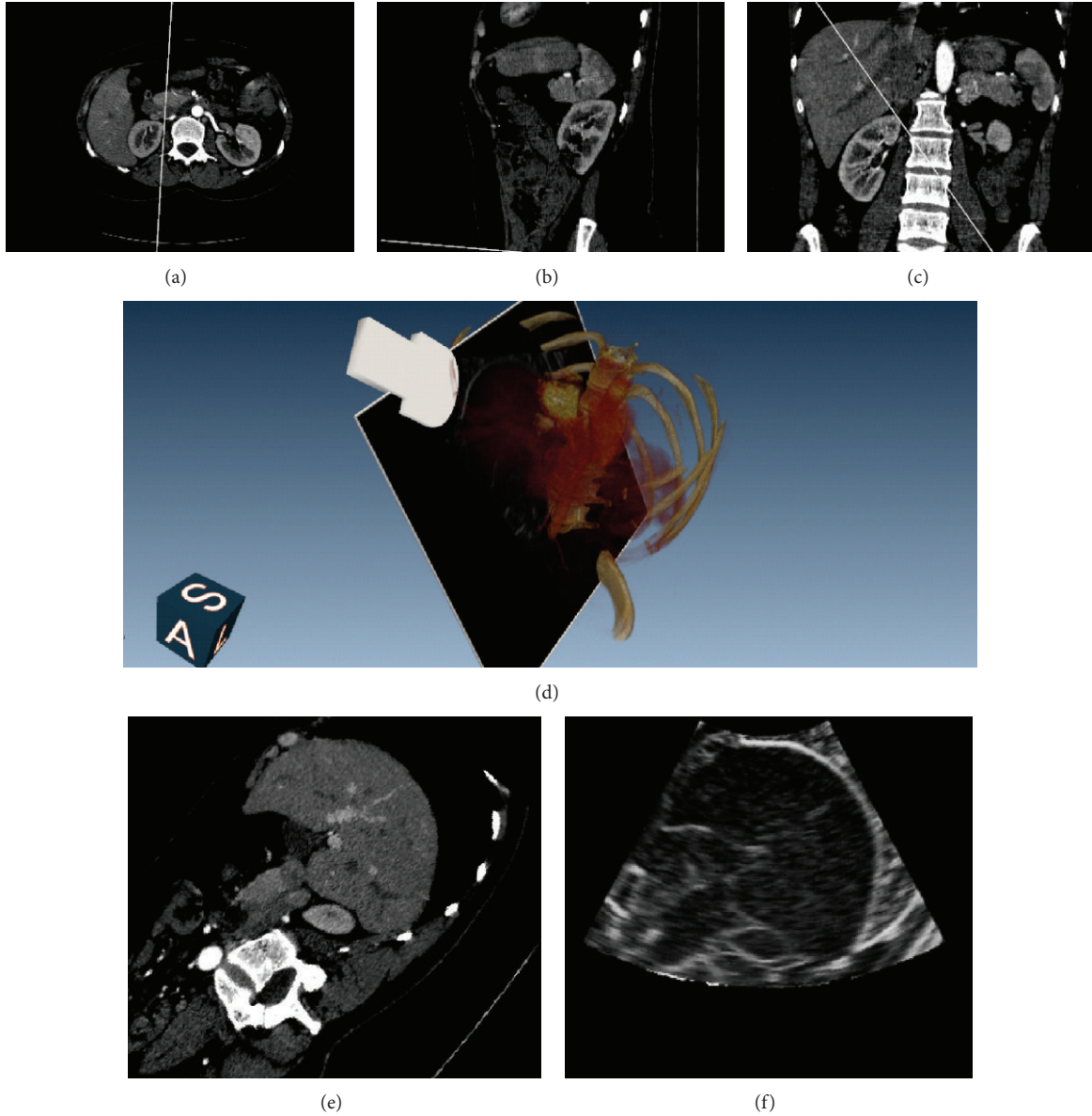


FIGURE 8: Screen-shot of the simulation system. (a), (b), and (c) are the axial plane, coronal plane and sagittal plane of CT image, respectively. (d) is the volume rendering of the CT image blended with the extracted image section on the direction and location of the virtual transducer. (e) is the extracted section of CT image. (f) is the simulated ultrasound image.

different views can be adjusted simultaneously using the slider bar. (4) Each view in the display window can be maximized to full screen model and reset to its default.

Figure 9 gives the final simulation results of three sections of abdominal CT images. The first row shows the extracted sector CT image, while the second row gives the corresponding simulated ultrasound. It can be seen that the internal structure of the liver can be visualized clearly. In the CT slices, the spines can be visually detected in the left bottom parts, as marked in the circles. In the simulated images, it can be seen that lower parts away from the spines are displayed as black empty areas. Obviously, the acoustic wave is absorbed by the bones and cannot be transmitted to the lower parts of

the simulated images. Our algorithm effectively simulated the ultrasonic propagation phenomenon.

4. Conclusion and Discussion

The ultrasound simulation technique not only provides a cheap and efficient way of training doctors in the study of the anatomic structure of human body but can also be used to validate the registration efficiency of the ultrasound navigation system. In this paper, a novel framework is proposed for fast ultrasound simulation and visualization. A multiscale method is utilized to enhance the tubular structure

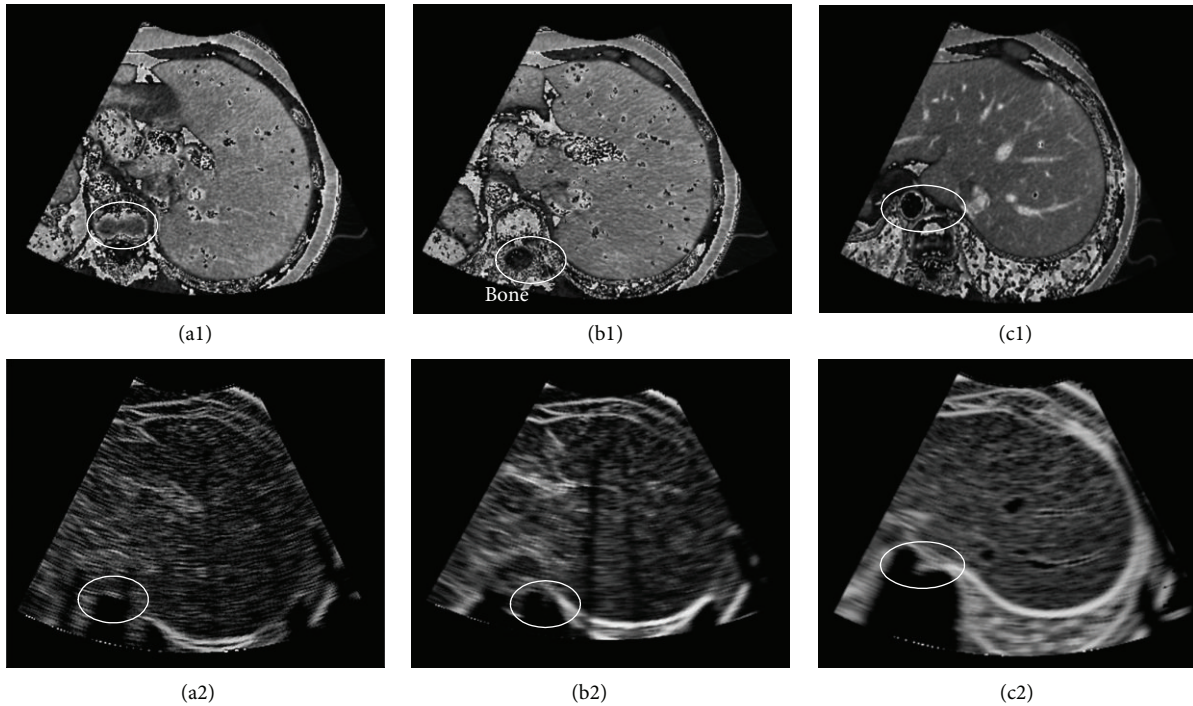


FIGURE 9: Simulation results of the proposed algorithm. The first row is the sector area of the CT slice. The second row is the simulated ultrasound.

of the CT image and to obtain a realistic simulation of the vascular structure. Seamless transformations between sector and rectangle shapes are then achieved using the thin-plate spline interpolation method. The parameters of acoustic response are based on the intensity difference ratio of adjacent regions for acoustic wave propagation in a piecewise homogenous medium and are fast calculated. Moreover, the detected edge information on different tissues is combined with random noises to simulate the acoustic response rate of the interesting region. Speckle noise and blurring are also added to the simulated ultrasound, resulting in an image that can be fast updated according to the user-defined parameters. Finally, the Kaiser window function is employed to simulate integration effects of multiple transducer elements. Based on the experimental results, realistic simulation results are obtained. Aside from soft tissues and bones, vasculatures can be clearly observed in the simulated ultrasound. Based on the efficiency evaluation experiments, the proposed simulation method is also very fast. The average frame rate of the proposed ultrasound simulator is approximately 20 fps ($SM = 300$, $FOV = 75^\circ$), which is better than the 16 fps rate commonly used in clinical radiology. However, the quantitative evaluation of the ultrasound simulation techniques is very difficult so far because of three main reasons: first, it is difficult to obtain the accurate imaging angle of the handheld ultrasound probe. Second, it is very difficult to control the pressure degree on soft tissues during the imaging procedures, for which a different pressure will lead to a different imaging depth. Third, the imaging quality of the ultrasound is strictly correlated with the adjustable parameters of the transducer elements. Hence, it is very difficult to obtain the ultrasound with predefined imaging parameters, which

hence can be evaluated from the anatomic structures in CT image. Up to now, the commonly used evaluation method for ultrasound simulation is the visual comparison by physicians in clinical practice. In this paper, the effectiveness of the developed method is quantified on realistic brain phantoms. And the experimental results are assessed by experts from the ultrasonic department at the General Hospital of People's Liberation Army, China.

The interesting application of the proposed method is its use in training for different ultrasound examinations or ultrasound-guided procedures. During a training session, the simulated ultrasound can be displayed with the model constructed from the CT image to provide an anatomical context to the trainee. Vascular enhancement and scattering image simulation are time consuming and require a cluster of CPUs to be practical. Hence, GPU implementation of the algorithm will considerably accelerate the simulation speed, which will meet the higher requirements of fine-resolution simulation. In this paper, all acquisition parameters can be interactively adjusted during simulation processing, including ultrasound frequency, ultrasound intensity, FOV, PD, as well as speckle noise size. Hence, the proposed simulation method is highly convenient for the simulation of different imaging conditions.

Conflict of Interests

The authors declare that they have no conflict of interests.

Acknowledgments

This work was supported by the National Basic Research Program of China (2010CB732505, 2013CB328806), Key

Projects in the National Science & Technology Pillar Program (2013BAI01B01), and the Plan of Excellent Talent in Beijing (2010D009011000004).

References

- [1] H. Maul, A. Scharf, P. Baier et al., "Ultrasound simulators: experience with the SonoTrainer and comparative review of other training systems," *Ultrasound in Obstetrics and Gynecology*, vol. 24, no. 5, pp. 581–585, 2004.
- [2] K. Cleary and T. M. Peters, "Image-guided interventions: technology review and clinical applications," *Annual Review of Biomedical Engineering*, vol. 12, pp. 119–142, 2010.
- [3] S. Beller, M. Hünerbein, T. Lange et al., "Image—guided surgery of liver metastases by three-dimensional ultrasound—based optoelectronic navigation," *British Journal of Surgery*, vol. 94, no. 7, pp. 866–875, 2007.
- [4] C. Forest, O. Comas, C. Vaysière, L. Soler, and J. Marescaux, "Ultrasound and needle insertion simulators built on real patient-based data," *Studies in Health Technology and Informatics*, vol. 125, pp. 136–139, 2007.
- [5] M. M. Knudson and A. C. Sisley, "Training residents using simulation technology: experience with ultrasound for trauma," *Journal of Trauma*, vol. 48, no. 4, pp. 659–665, 2000.
- [6] C. Terkamp, G. Kirchner, J. Wedemeyer et al., "Simulation of abdomen sonography. Evaluation of a new ultrasound simulator," *Ultraschall in der Medizin*, vol. 24, no. 4, pp. 239–244, 2003.
- [7] M. P. Laguna, T. M. De Reijke, and J. J. De La Rosette, "How far will simulators be involved into training?" *Current Urology Reports*, vol. 10, no. 2, pp. 97–105, 2009.
- [8] D. Henry, J. Troccaz, J. Bosson, and O. Pichot, "Ultrasound imaging simulation: application to the diagnosis of deep venous thromboses of lower limbs," in *Proceedings of the Medical Image Computing and Computer-Assisted Intervention (MICCAI '98)*, pp. 1032–1040, 1998.
- [9] M. Weidenbach, C. Wick, S. Pieper et al., "Augmented reality simulator for training in two-dimensional echocardiography," *Computers and Biomedical Research*, vol. 33, no. 1, pp. 11–22, 2000.
- [10] R. Shams, R. Hartley, and N. Navab, "Real-time simulation of medical ultrasound from CT images," in *Proceedings of the Medical Image Computing and Computer-Assisted Intervention (MICCAI '08)*, pp. 734–741, 2008.
- [11] O. Kutter, R. Shams, and N. Navab, "Visualization and GPU-accelerated simulation of medical ultrasound from CT images," *Computer Methods and Programs in Biomedicine*, vol. 94, no. 3, pp. 250–266, 2009.
- [12] T. Reichl, J. Passenger, O. Acosta, and O. Salvado, "Ultrasound goes GPU: real-time simulation using CUDA," in *Proceedings of the Medical Imaging: Biomedical Applications in Molecular, Structural, and Functional Imaging*, vol. 7261, Lake Buena Vista, Fla, USA, February 2009.
- [13] A. Hostettler, C. Forest, A. Forgione, L. Soler, and J. Marescaux, "Real-time ultrasonography simulator based on 3D CT-scan images," *Studies in Health Technology and Informatics*, vol. 111, pp. 191–193, 2005.
- [14] S. Mansurova, P. M. Zarate, P. Rodriguez, S. Stepanov, S. Köber, and K. Meerholz, "Non-steady-state photoelectromotive force effect under linear and periodical phase modulation: application to detection of Doppler frequency shift," *Optics Letters*, vol. 37, no. 3, pp. 383–385, 2012.
- [15] A. M. Bazen and S. H. Gerez, "Fingerprint matching by thin-plate spline modelling of elastic deformations," *Pattern Recognition*, vol. 36, no. 8, pp. 1859–1867, 2003.
- [16] A. Rosas and M. Bastir, "Thin-plate spline analysis of allometry and sexual dimorphism in the human craniofacial complex," *American Journal of Physical Anthropology*, vol. 117, no. 3, pp. 236–245, 2002.
- [17] Y. P. Lin and P. Vaidyanathan, "A Kaiser window approach for the design of prototype filters of cosine modulated filterbanks," *IEEE Signal Processing Letters*, vol. 5, no. 6, pp. 132–134, 1998.
- [18] A. Frangi, W. Niessen, K. Vincken, and M. A. Viergever, "Multiscale vessel enhancement filtering," in *Proceedings of the Medical Image Computing and Computer-Assisted Intervention (MICCAI '98)*, pp. 130–137, 1998.
- [19] Y. Wang, Y. Shen, J. Zhou et al., "Dual-beam-reflection phenomenon due to leaky modes in a photonic band gap," *Optics Communications*, vol. 284, no. 5, pp. 1123–1126, 2011.
- [20] H. Chui and A. Rangarajan, "A new point matching algorithm for non-rigid registration," *Computer Vision and Image Understanding*, vol. 89, no. 2-3, pp. 114–141, 2003.
- [21] K. Thangavel, R. Manavalan, and I. L. Arوقيaraj, "Removal of speckle noise from ultrasound medical image based on special filters: comparative study," *ICGST-GVIP Journal*, vol. 9, pp. 25–32, 2009.
- [22] F. Palhano Xavier de Fontes, G. Andrade Barroso, P. Coupé, and P. Hellier, "Real time ultrasound image denoising," *Journal of Real-Time Image Processing*, vol. 6, no. 1, pp. 15–22, 2011.
- [23] J. M. Sanches, J. C. Nascimento, and J. S. Marques, "Proceedings of the Medical image noise reduction using the Sylvester-Lyapunov equation," *IEEE Transactions on Image Processing*, vol. 17, no. 9, pp. 1522–1539, 2008.
- [24] W. Wein, A. Khamene, D. A. Clevert et al., "Simulation and fully automatic multimodal registration of medical ultrasound," in *Proceedings of the Medical Image Computing and Computer-Assisted Intervention (MICCAI '07)*, pp. 136–143, 2007.
- [25] K. K. Shung and G. A. Thieme, *Ultrasonic Scattering in Biological Tissues*, CRC, 1993.
- [26] B. Li, S. Wang, and Y. Huang, "Aluminum diffuser of Lambert scattering and high reflectivity based on abrasion and sodium hydroxide corrosion," *Journal of Modern Optics*, vol. 57, no. 13, pp. 1189–1193, 2010.
- [27] H. Roitner and P. Burgholzer, "Efficient modeling and compensation of ultrasound attenuation losses in photoacoustic imaging," *Inverse Problems*, vol. 27, no. 1, Article ID 015003, 2011.
- [28] S. J. S. Chen, P. Hellier, J. Y. Gauvrit, M. Marchal, X. Morandi, and D. L. Collins, "An anthropomorphic polyvinyl alcohol triple-modality brain phantom based on Colin27," in *Proceedings of the Medical Image Computing and Computer-Assisted Intervention (MICCAI '10)*, pp. 92–100, Springer, 2010.

Research Article

Automatic Sex Determination of Skulls Based on a Statistical Shape Model

Li Luo,¹ Mengyang Wang,¹ Yun Tian,¹ Fuqing Duan,¹ Zhongke Wu,¹
Mingquan Zhou,¹ and Yves Rozenholc²

¹ College of Information Science and Technology, Beijing Normal University, Beijing 100875, China

² Laboratoire MAP5, UMR CNRS 8145, University Paris Descartes, 45 rue des Saints-Pères, 75006 Paris, France

Correspondence should be addressed to Fuqing Duan; fqduan@bnu.edu.cn

Received 11 July 2013; Accepted 4 October 2013

Academic Editor: Yunmei Chen

Copyright © 2013 Li Luo et al. This is an open access article distributed under the Creative Commons Attribution License, which permits unrestricted use, distribution, and reproduction in any medium, provided the original work is properly cited.

Sex determination from skeletons is an important research subject in forensic medicine. Previous skeletal sex assessments are through subjective visual analysis by anthropologists or metric analysis of sexually dimorphic features. In this work, we present an automatic sex determination method for 3D digital skulls, in which a statistical shape model for skulls is constructed, which projects the high-dimensional skull data into a low-dimensional shape space, and Fisher discriminant analysis is used to classify skulls in the shape space. This method combines the advantages of metrical and morphological methods. It is easy to use without professional qualification and tedious manual measurement. With a group of Chinese skulls including 127 males and 81 females, we choose 92 males and 58 females to establish the discriminant model and validate the model with the other skulls. The correct rate is 95.7% and 91.4% for females and males, respectively. Leave-one-out test also shows that the method has a high accuracy.

1. Introduction

Sex identification from skeletons is a vital work for a forensic anthropological analysis. Previous studies [1–4] indicate that pelvis is the most reliable indicator of sex assessment, and skull is the second one. However, not all forensic cases provide a complete skeleton due to breakage or postmortem destruction, while the skull can be well preserved in most cases since it is composed of hard tissue. So the skull is the most commonly used skeleton part in forensic anthropological analysis.

Traditional skeletal sex assessments principally rely on visual assessments of sexually dimorphic traits. Rogers [5] achieves an accuracy of 89.1% for a historic skeletal collection by using visual morphological traits. By scoring the visual assessments of five cranial traits (glabella, mental, orbit, nuchal, and mastoid), Walker [6] achieves 90% accuracy for modern American skulls via a quadratic discriminant analysis model incorporating scores. According to Daubert [7] and Mohan [8] criteria, Williams and Rogers [9] assess 21 skull characteristics of 50 white European Americans (25 males and 25 females). For a characteristic, if the intraobserver error

is no more than 10% and the accuracy is above 80% when it is used separately to identify the sex, the characteristic is defined as a high quality characteristic. They get six high quality characteristics like eyebrow, orbit, and so forth, and the accuracy reaches 94% by utilizing visual assessments of all these six characteristics. Visual assessments depend heavily on physical anthropologists' understanding of population differences in sexual dimorphism. The visual assessment results reported in the paper [10] show that Krogman and Iscan achieve 92% accuracy using the Todd collection, while Stewart only obtains 77% accuracy using some American black skulls from the Terry collection. Ramsthaler et al. [11] use kappa statistics to quantify the disagreement in sex classification performed by two different observers after visual assessment, and the agreement only reaches 90.8%. Moreover, visual assessment of the morphological traits is likely to be inaccurate when performed by an inexperienced observer due to its great subjectivity. With the progress of the digital imaging technology in medicine, discriminant analysis for skeletal measurements is increasingly used for sex estimation.

Since radiograph can provide architectural and morphological details of the skull, some researchers [12–15] use skull radiograph for sex identification. Hsiao et al. [12] consider the lateral radiographs of 50 male and 50 female adult skulls from Taiwan. They use 18 cephalometric variables, which are derived from some cephalometric points on the lateral radiographs, to build the discriminant function, and claim a coincidence rate of 100%. But they do not mention the generalization ability of the discriminant function, that is, the classification ability for new samples. Veyre-Goulet et al. [15] validate the method of Hsiao by using the lateral radiographic data of 114 Europeans. They find that the result using 8 cephalometric variables is the same as the one using 18 variables, and the coincidence rate is 95.6%. They think that different cephalometric variables can be used for different races. Inoue et al. [14] compute the gradients and distances of 39 measuring points in the lateral contour of the skull and establish the discriminant function through these variables by using 50 female and 50 male skulls from Japan as specimens. 21 other specimens are tested, and the mean correct rate is 86%. They conclude that gradient has higher ability in reflecting gender differences than distances.

Other researchers use some variables measured from 3D skulls to establish discriminant functions. Spradley and Jantz [16] construct multivariate discriminant models using the skull data from the Forensic Anthropology Data Bank. They measure different variables for different races, and the highest identification rate is no more than 90%. Jantz and Ousley [17] issue the computer-aided software called Fordisc for skeleton analysis. This software measures skeleton characteristics by the human-computer interactive way and utilize the data from American Forensic Data Bank to establish the discriminant function. Guyomarc'h and Bruzek [18] compare the sex identification effects of the software for different races such as Thailand and France, and the correct recognition rate is between 52.2% and 77.8%. Ramsthaler et al. [19] test this software by using 98 Caucasian German skulls, and the correct rate is 86%. These studies show that the craniofacial morphology has great diversities among different races. For Chinese, Li [20] manually extracts the mid-sagittal frontal arc on dried skulls from northeast China, and the Fourier coefficients of the arc are used for multivariate stepwise discriminant analysis. The recognition rate for 31 test skulls is 84.21% and 83.33% for males and females, respectively. Shui [21] measures 14 metric variables and utilizes 94 skulls from north China to establish stepwise fisher discriminant functions. The recognition rate for 39 test skulls reaches 87%.

Discriminant analysis for skeletal measurements requires a high measurement precision. However, the accurate measurement of the skull is quite difficult. Williams and Rogers [9] show that, for most measure variables, usually the measurement error among different observers is above 10%. Moreover, the skull size changes with varying ages. In this work, we propose an automatic sex determination method for 3D digital skulls. A statistical shape model is established to describe statistical features of the skull morphology, and Fisher discriminant analysis of the shape parameters is used to classify skulls. The advantages of this method is as follows: Firstly, it needs no professional qualification and tedious

manual measurement; Secondly, it is less influenced by the variation of the skull size; Finally, it can get a high recognition rate.

2. Materials and Methods

2.1. Materials. This study has been approved by the Institutional Review Board (IRB) of Image Center for Brain Research, National Key Laboratory of Cognitive Neuroscience and Learning, Beijing Normal University. It is carried out on a database of 208 whole skull CT scans on voluntary persons that mostly come from Han ethnic group in North of China, age 19–75 years for females and 21–67 years for males. There are 81 females and 127 males. The CT images were obtained by a clinical multislice CT scanner system (Siemens Sensation 16) in the Xianyang hospital located in western China. The images of each subject are restored in DICOM format with a size of approximately $512 \times 512 \times 250$. Each 3D skull surface is extracted from the CT images and represented as a triangle mesh including about 150,000 vertices. All the skulls are substantially complete; that is, each skull contains all the bones from calvarias to jaw and has the full mouth of teeth.

To eliminate the inconsistency in position, pose, and scale caused by data acquirement, all the samples are transformed into a uniform coordinate system. The uniform coordinate system is determined by four skull landmarks, left porion, right porion, left (or right) orbitale, and glabella (denoted as L_p, R_p, L_o, G). From three points, L_p, R_p, L_o , the Frankfurt plane is determined [22]. The coordinate origin (denotes as O) is the intersection point of the line L_pR_p and the plane that contains point G and orthogonally intersects with line L_pR_p . We take the line OR_p as x -axis. The z -axis is the line through the point O and with the direction being the normal of the Frankfurt plane. Then y -axis is obtained by the cross product of z - and x -axis. Once the uniform coordinate system is defined, all the prototypic skulls are transformed into it. Finally, the scale of all the samples is standardized by setting the distance between L_p and R_p to unit; that is, each vertex (x, y, z) of the skull is scaled by $(x/|L_p - R_p|, y/|L_p - R_p|, z/|L_p - R_p|)$. One skull in the uniform coordinate system is shown in Figure 1.

2.2. Statistical Shape Model Construction. Statistical shape model is a widely used technique in medical image analysis. It can efficiently describe the shape variance and ensure that only statistically likely shapes are represented. Principal Component Analysis (PCA) [23] is a powerful tool to build statistical shape models, and it finds the major and minor modes of shape variation across the training data. In order to build the statistical model, a dense point correspondence has to be established across the training set, that is, building a point-to-point correspondence for all training samples according to human anatomy characteristics. There are many nonrigid registration methods [24–26] for dense mesh or point cloud objects, and here we adopt the method presented by Hu et al. [25]. As in [25], the back part of the reference skull is cut away (as shown in Figure 2) considering that there

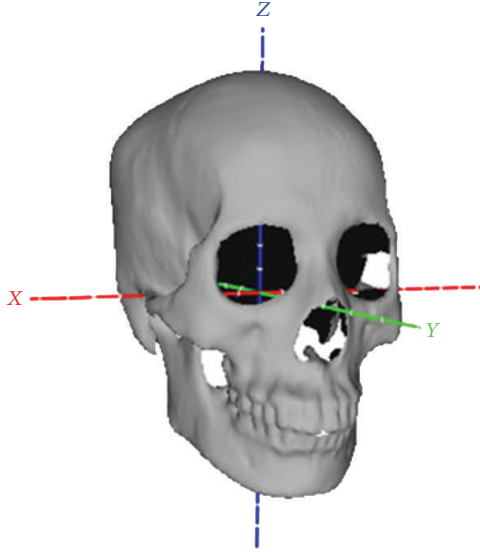


FIGURE 1: One skull in the uniform coordinate system.



FIGURE 2: The back part of the reference skull is cut away.

are too many vertices in the whole skull, and the sexually dimorphic traits are mainly on the front part of skulls. So all of the aligned training skulls only keep the front part corresponding to the reference.

By concatenating coordinates of all the vertices, a skull can be represented as a high dimension vector. Thus we construct a dataset of skulls $\{\mathbf{S}_i = (x_{i1}^S, y_{i1}^S, z_{i1}^S, \dots, x_{im}^S, y_{im}^S, z_{im}^S)^T \mid i = 1, 2, \dots, N\}$, where each coordinate index labels corresponding points across the training set.

From the skull dataset, the mean skull data $\bar{\mathbf{S}}$ and covariance matrix Σ of the mean normalized skulls are calculated. PCA essentially transforms the mean normalized shape data into a subspace spanned by the orthogonal unit eigenvectors \mathbf{U}_k , $k = 1, 2, \dots, N - 1$, of the covariance matrix in descending order according to their associated eigenvalues

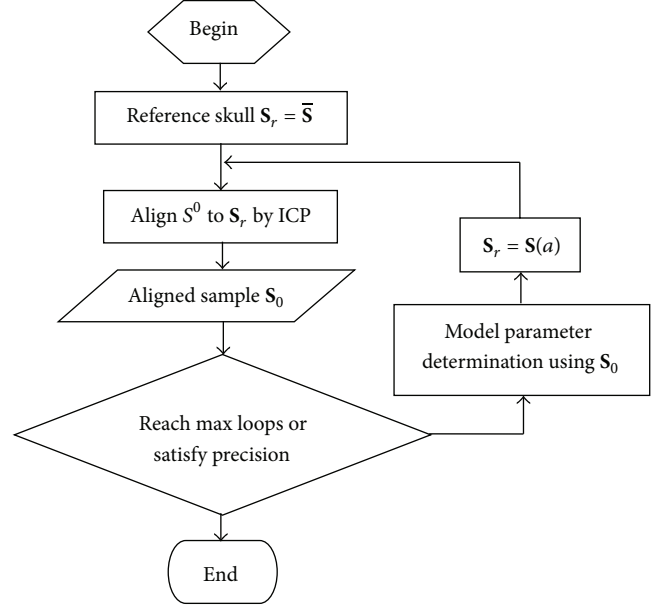


FIGURE 3: Model matching procedure.

λ_k , which represent variation modes of the data. Then the skull statistical shape model is constructed as in the following parameterized model:

$$\mathbf{S}(\mathbf{a}) = \bar{\mathbf{S}} + \sum_{k=1}^M a_k \mathbf{U}_k, \quad (1)$$

where the number M is the mode number, usually determined by a variance contribution rate calculated from the cumulative eigenvalues, and the combination coefficient $\mathbf{a} = (a_1, a_2, \dots, a_M)^T$ is the model parameter. Apparently this statistical shape model assumes that the shape vectors \mathbf{S} obey a normal distribution with mean $\bar{\mathbf{S}}$ and covariance matrix Σ , so the parameter \mathbf{a} for a plausible skull meets a normal distribution with zero mean and covariance matrix $\text{diag}(\lambda_1, \lambda_2, \dots, \lambda_M)$.

2.3. Statistical Shape Model Matching. Model matching is to determine the model parameter for a given skull. If the skull data \mathbf{S}_0 is aligned, the model parameters can be determined by PCA transform. According to the statistical models (1), let $\mathbf{P}_s = [\mathbf{U}_1, \mathbf{U}_2, \dots, \mathbf{U}_M]$ denote the PCA transform matrix for skulls, and the model parameter can be determined as follows:

$$\mathbf{a} = \mathbf{P}_s^T (\mathbf{S}_0 - \bar{\mathbf{S}}). \quad (2)$$

So in fact the model matching is a procedure of the skull registration. Given an unknown prototypic skull data \mathbf{S}^0 , it is firstly transformed into the uniform coordinate system as Section 2.1 describes. Figure 3 shows a statistical shape model based registration algorithm. As shown in Figure 3, a dynamic reference, denoted as \mathbf{S}_r , is updated by the statistical shape model in each loop, whose model parameter is determined by the PCA transform of the corresponding aligned sample

S_0 of last iteration. The initial reference is selected as the mean shape, and an ICP algorithm [27] is used to align a target to the reference. Apparently, the dynamic reference will be closer and closer to the target skull along with the iterating, so the iteration will converge. When the aligned sample does not change, the iteration stops.

2.4. Fisher Discriminant Analysis in the Shape Parameter Space. Fisher discriminant analysis is increasingly used for skull sex determination. It projects samples from a high-dimensional feature space into one axis called Fisher vector, in which optimal linear classification can be achieved. Different from previous methods, we perform Fisher discriminant analysis not for skull measurements, but for shape parameters of skulls.

According to the statistical shape model (1), a skull is represented as a feature vector $\mathbf{a} = (a_1, a_2, \dots, a_M)^T$. Let \mathbf{m}_i , n^i , $i = 1, 2$, denote the mean and the number of the training samples of the i th class, and let \mathbf{X}_j^i be the feature vector of the j th sample of the i th class. Then within-class scatter matrix and between-class scatter matrix can be defined as follows:

$$\mathbf{S}_w = \sum_{i=1}^2 \left(\sum_{j=1}^{n^i} (\mathbf{X}_j^i - \mathbf{m}_i) (\mathbf{X}_j^i - \mathbf{m}_i)^T \right), \quad (3)$$

$$\mathbf{S}_b = (\mathbf{m}_1 - \mathbf{m}_2) (\mathbf{m}_1 - \mathbf{m}_2)^T.$$

The Fisher criterion is that the samples of the same class are aggregated in the Fisher vector space, while the samples of different class are separated as much as possible. So the objective function is defined as follows:

$$\mathbf{J}_F(\mathbf{w}) = \frac{\mathbf{w}^T \mathbf{S}_b \mathbf{w}}{\mathbf{w}^T \mathbf{S}_w \mathbf{w}}. \quad (4)$$

By Lagrange Multiplier, the Fisher vector to this maximization problem is as follows:

$$\mathbf{w} = \mathbf{S}_w^{-1} (\mathbf{m}_1 - \mathbf{m}_2). \quad (5)$$

Then each skull feature vector \mathbf{a} can be projected to the Fisher vector, in which two classes of samples can be well separated:

$$t = \mathbf{W}^T \mathbf{a}. \quad (6)$$

Finally, a threshold is selected by using some prior knowledge, for example,

$$t_0 = \mathbf{W}^T \frac{(\mathbf{m}_1 + \mathbf{m}_2)}{2}. \quad (7)$$

Given an unknown skull, the procedure of the sex determination is as follows.

Step 1. Perform the statistical shape model matching to determine the shape parameter as Figure 3 describes.

Step 2. Project the shape parameter to the Fisher vector, and get the projection value t .

Step 3. If the value is larger than the threshold, the skull gender is male. Otherwise, it is female.

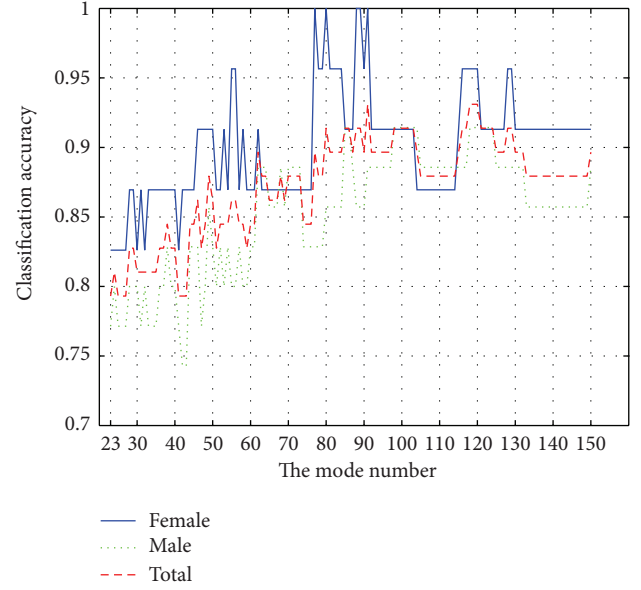


FIGURE 4: Variation of the correct classification rate of the test samples with the mode number.

3. Results

The used data are the 208 whole skull CT scans described in Section 2. We chose about three-fourths of the 208 skulls according to the age distribution as training samples, including 92 males and 58 females, and other skulls as test samples. In order to determine an appropriate mode number (M in (1)) to build the statistical shape model, we use the trial and error technique and analyze the variation of the classification accuracy of the test samples with varying the mode number by experiments. It is well known that, in PCA, generally only some eigenvectors corresponding to large eigenvalues of the covariance matrix represent modes of variation of the data, while others represent noises. We vary the mode number from 23 to 150, corresponding to variance contribution rate from 96% to 100%, and the correct classification rates for test samples are shown in Figure 4, while the rate of training samples is 100% when the mode number is larger than 80. From Figure 4 we can see that the correct classification rate of females is always higher than that of males, both of the correct rates for females and males are above 86% when the mode number is greater than 80, and the total correct rate for all test samples reaches maximum with the mode number being 91, 118, 119, and 120. Since the correct rate is stable with the mode number varying from 118 to 120, we use 119 modes to build the statistical shape model.

Figure 5(a) shows the classification of the training samples with the mode number being 119, and the classification accuracy of the training samples is 100%. Figure 5(b) shows the classification of the test samples. One female and 3 males are misclassified, and the correct rate is 95.7% and 91.4% for females and males, respectively. We also classify the whole 208 samples using leave-one-out strategy. That is, repeatedly 207 samples are chosen as training samples, and the residual

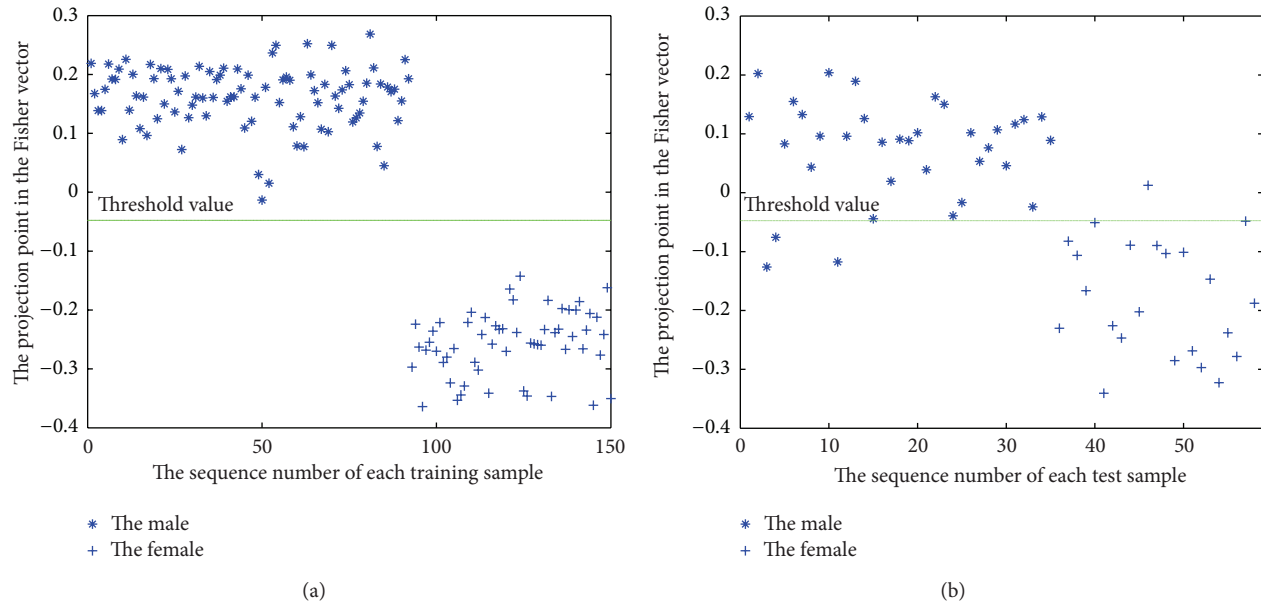


FIGURE 5: Classification of training samples (a) and test samples (b).

one is used as test sample. The mode number is still 119, which maybe is not the optimal selection. The correct classification rate is 91.3% and 90.1% for males and females, respectively. Compared with the accuracy of 87% by Shui [21], which is a metric analysis method and uses a subset of our 208 skulls to establish the discriminant functions, this method highly improves the accuracy.

4. Discussion

Traditional morphological methods depend heavily on physical anthropologists' subjective understanding of population differences in sexual dimorphism. Different observers usually have a significant difference when performing the visual assessment of the morphological traits, especially for those inexperienced observers. On the other hand, discriminant analysis for skeletal measurements depends less on the examiner's professional qualification and experience, but it requires a high measurement precision, which is not easy to realize. Majority of scientists contend that the combination of metrical and morphological methods is the best way [28]. In this work, we use 3D dense point cloud data to build the statistical shape model, and in a sense, the model parameters metrically describe the skull morphology. So the method combines the advantages of metrical and morphological methods. Different from previous methods, what this method measures is not distance- or volume-related variables, but global shape variations.

Previous studies [18] show that the performance of sex determination outside the reference population group for which the discriminant function has been developed is poor. We do not know whether this method also has this problem due to lack of skull samples of another population, but there indeed exists the problem of selection of training samples. The more complete the training samples are, the better

the performance is. That is, the training samples should depict shape variations as much as possible. We think that only if other populations have similar shape variations, the discriminant model we build is applicable. That just is the reason that the correct classification rate of females is uniformly higher than that of males, as shown in Figure 4. When the statistical shape model and the discriminant function have been established, sex determination of an unknown skull becomes easy to perform, and needs no professional qualification and tedious manual measurement. Moreover, although we use CT scans to construct 3D point cloud model of the skull in this work, the statistical shape model we build also can deal with 3D models constructed in any way such as laser scan 3D camera.

Acknowledgments

This work was partially supported by the National Natural Science Foundation of China (no. 61272363) and Program for New Century Excellent Talents in University (NCET-13-0051).

References

- [1] W. M. Bass, *Human Osteology: A Laboratory and Field Manual*, Missouri Archaeological Society Columbia, 5th edition, 2005.
- [2] D. L. France, "Observation and metric analysis of sex in the skeleton," in *Forensic Osteology: Advances in the Identification of Human Remains*, K. J. Reichs, Ed., pp. 163–186, Charles C. Thomas, Springfield, Ill, USA, 1998.
- [3] R. B. Pickering and D. C. Bachman, *The Use of Forensic Anthropology*, CRC Press, Boca Raton, Fla, USA, 1997.
- [4] D. H. Ubelaker and C. G. Volk, "A test of the Phenice method for the estimation of sex," *Journal of Forensic Sciences*, vol. 47, no. 1, pp. 19–24, 2002.

- [5] T. L. Rogers, "Determining the sex of human remains through cranial morphology," *Journal of Forensic Sciences*, vol. 50, no. 3, pp. 493–500, 2005.
- [6] P. L. Walker, "Sexing skulls using discriminant function analysis of visually assessed traits," *American Journal of Physical Anthropology*, vol. 136, no. 1, pp. 39–50, 2008.
- [7] Regina vJ-LJ, S.C.R. File No. 26830, 2000.
- [8] United States Supreme Court in *Daubert v. Merrell Dow Pharmaceuticals Inc.* 509 U.S. 579, 1993.
- [9] B. A. Williams and T. L. Rogers, "Evaluating the accuracy and precision of cranial morphological traits for sex determination," *Journal of Forensic Sciences*, vol. 51, no. 4, pp. 729–735, 2006.
- [10] W. M. Krogman and M. Y. Iscan, *The Human Skeleton in Forensic Medicine*, Charles C. Thomas, Springfield, Ill, USA, 1986.
- [11] F. Ramsthaler, M. Kettner, A. Gehl, and M. A. Verhoff, "Digital forensic osteology: morphological sexing of skeletal remains using volume-rendered cranial CT scans," *Forensic Science International*, vol. 195, no. 1–3, pp. 148–152, 2010.
- [12] T.-H. Hsiao, H.-P. Chang, and K.-M. Liu, "Sex determination by discriminant function analysis of lateral radiographic cephalometry," *Journal of Forensic Sciences*, vol. 41, no. 5, pp. 792–795, 1996.
- [13] T.-H. Hsiao, S.-M. Tsai, S.-T. Chou et al., "Sex determination using discriminant function analysis in children and adolescents: a lateral cephalometric study," *International Journal of Legal Medicine*, vol. 124, no. 2, pp. 155–160, 2010.
- [14] M. Inoue, T. Inoue, Y. Fushimi, and K. Okada, "Sex determination by discriminant function analysis of lateral cranial form," *Forensic Science International*, vol. 57, no. 2, pp. 109–117, 1992.
- [15] S. A. Veyre-Goulet, C. Mercier, O. Robin, and C. Guérin, "Recent human sexual dimorphism study using cephalometric plots on lateral telerradiography and discriminant function analysis," *Journal of Forensic Sciences*, vol. 53, no. 4, pp. 786–789, 2008.
- [16] M. K. Spradley and R. L. Jantz, "Sex estimation in forensic anthropology: skull versus postcranial elements," *Journal of Forensic Sciences*, vol. 56, no. 2, pp. 289–296, 2011.
- [17] R. L. Jantz and S. D. Ousley, *FORDISC 3: Computerized Forensic Discriminate Functions*, Version 3.0, University of Tennessee, Knoxville, Tenn, USA, 2005.
- [18] P. Guyomarc'h and J. Bruzek, "Accuracy and reliability in sex determination from skulls: a comparison of Fordisc 3.0 and the discriminant function analysis," *Forensic Science International*, vol. 208, no. 1–3, pp. 180.e1–180.e6, 2011.
- [19] F. Ramsthaler, K. Kreutz, and M. A. Verhoff, "Accuracy of metric sex analysis of skeletal remains using Fordisc based on a recent skull collection," *International Journal of Legal Medicine*, vol. 121, no. 6, pp. 477–482, 2007.
- [20] C. B. Li, "Study on sex difference of adult human skull in the northest china by stepwise discriminant analysis," *Journal of China Medical University*, vol. 1, no. 21, pp. 28–31, 1992.
- [21] W. Y. Shui, *Research and application of craniofacial morphology [dissertation]*, Beijing Normal University, 2011.
- [22] F. Q. Duan, S. Yang, D. H. Huang et al., "Craniofacial reconstruction based on multi-linear subspace analysis," *Multimedia Tools and Applications*, 2013.
- [23] X.-H. Liu, Y. Sun, and Y. Wu, "Reduction of hyperspectral dimensions and construction of discriminating models for identifying wetland plant species," *Spectroscopy and Spectral Analysis*, vol. 32, no. 2, pp. 459–464, 2012 (Chinese).
- [24] Q. Q. Deng, M. Q. Zhou, W. Y. Shui, Z. Wu, Y. Ji, and R. Bai, "A novel skull registration based on global and local deformations for craniofacial reconstruction," *Forensic Science International*, vol. 208, no. 1–3, pp. 95–102, 2011.
- [25] Y. Hu, F. Duan, B. Yin et al., "A hierarchical dense deformable model for 3D face reconstruction from skull," *Multimedia Tools and Applications*, vol. 64, pp. 345–364, 2013.
- [26] Y. Hu, F. Duan, M. Zhou et al., "Craniofacial reconstruction based on a hierarchical dense deformable model," *EURASIP Journal on Advances in Signal Processing*, vol. 2012, article 217, 14 pages, 2012.
- [27] P. J. Besl and N. D. McKay, "A method for registration of 3-D shapes," *IEEE Transactions on Pattern Analysis and Machine Intelligence*, vol. 14, no. 2, pp. 239–256, 1992.
- [28] B. Sejrnsen, N. Lynnerup, and M. Hejmadi, "An historical skull collection and its use in forensic odontology and anthropology," *Journal of Forensic Odonto-Stomatology*, vol. 23, no. 2, pp. 40–44, 2005.

Research Article

An Approach for the Visualization of Temperature Distribution in Tissues According to Changes in Ultrasonic Backscattered Energy

Jingjing Xia,¹ Qiang Li,¹ Hao-Li Liu,² Wen-Shiang Chen,³ and Po-Hsiang Tsui^{4,5}

¹ School of Electronic Information Engineering, Tianjin University, Tianjin 300072, China

² Department of Electrical Engineering, Chang-Gung University, Taoyuan 33302, Taiwan

³ Department of Physical Medicine and Rehabilitation, National Taiwan University Hospital and College of Medicine, Taipei 10002, Taiwan

⁴ Department of Medical Imaging and Radiological Sciences, College of Medicine, Chang-Gung University, Taoyuan 33302, Taiwan

⁵ Healthy Aging Research Center, Chang-Gung University, Taoyuan 33302, Taiwan

Correspondence should be addressed to Po-Hsiang Tsui; tsuiph@mail.cgu.edu.tw

Received 15 May 2013; Accepted 10 September 2013

Academic Editor: Huafeng Liu

Copyright © 2013 Jingjing Xia et al. This is an open access article distributed under the Creative Commons Attribution License, which permits unrestricted use, distribution, and reproduction in any medium, provided the original work is properly cited.

Previous studies developed ultrasound temperature-imaging methods based on changes in backscattered energy (CBE) to monitor variations in temperature during hyperthermia. In conventional CBE imaging, tracking and compensation of the echo shift due to temperature increase need to be done. Moreover, the CBE image does not enable visualization of the temperature distribution in tissues during nonuniform heating, which limits its clinical application in guidance of tissue ablation treatment. In this study, we investigated a CBE imaging method based on the sliding window technique and the polynomial approximation of the integrated CBE (ICBE_{pa} image) to overcome the difficulties of conventional CBE imaging. We conducted experiments with tissue samples of pork tenderloin ablated by microwave irradiation to validate the feasibility of the proposed method. During ablation, the raw backscattered signals were acquired using an ultrasound scanner for B-mode and ICBE_{pa} imaging. The experimental results showed that the proposed ICBE_{pa} image can visualize the temperature distribution in a tissue with a very good contrast. Moreover, tracking and compensation of the echo shift were not necessary when using the ICBE_{pa} image to visualize the temperature profile. The experimental findings suggested that the ICBE_{pa} image, a new CBE imaging method, has a great potential in CBE-based imaging of hyperthermia and other thermal therapies.

1. Introduction

Previous studies have shown that hyperthermia complements chemotherapy and radiotherapy, increasing the success of cancer treatment [1–3]. When using hyperthermia, monitoring temperature is essential to ensure accurate and appropriate thermal dosage. The development of temperature-imaging techniques to measure the distribution of temperature has, therefore, been a long-term critical research goal.

Magnetic resonance imaging (MRI) is currently the standard imaging method used to monitor temperature changes in tissues [4, 5]. Previous studies have shown that MRI can provide satisfactory spatial resolution with a temperature

accuracy of 1°C. However, imaging temperature variations in heated regions using MRI might be difficult in practice because of the requirements for significant capital investment and the development of compatible heating therapies [6]. Compared to MRI, ultrasound imaging provides a convenient and powerful tool because of low cost, use of nonionizing radiation, simple signal processing, and real-time capability. Ultrasound imaging might, therefore, provide a more appropriate option for the clinical monitoring of temperature distributions.

The frequently used acoustic parameters for the monitoring of temperature include (1) echo shifts caused by changes in tissue thermal expansion and speed of sound [7, 8],

(2) variations in acoustic attenuation [9], and (3) changes in the backscattered energy (CBE) of ultrasound [10, 11]. Each method has specific temperature sensitivities, applications, and limitations. Previous studies identified that the CBE, in comparison with echo shifts and attenuation, is nearly monotonic in the clinical hyperthermia temperature range [10–12]. Considering the clinical value of imaging tools that visually display temperature profiles in tissues, investigators further proposed the CBE image based on a parametric mapping of CBEs as an ultrasound temperature-imaging method for the monitoring of regions undergoing heating [6, 13, 14]. The recent literature has confirmed the usefulness of the CBE image for detecting variations in tissue temperatures.

In practice, use of the CBE image for temperature estimation may have some difficulties. First, the CBE image is a ratio map obtained from the envelope image divided by the reference envelope image on a pixel-to-pixel basis [13]. Because temperature change induces the displacement of image features [13], the tracking of pixels between images obtained at adjacent temperatures is necessary to obtain the correct CBE at each pixel. Motion tracking and compensation are typically the most computationally intensive components of temperature imaging and hinder its real-time implementation [7, 8, 15, 16]. On the other hand, increasing temperature might also increase the degree of acoustic nonlinearity [17]. In this condition, local waveforms of the received radio-frequency (RF) signals can differ, resulting in greater error when performing pixel-by-pixel division between two images following motion tracking and compensation [18]. In addition, the CBE image cannot clearly illustrate the contours of temperature distribution in a tissue during nonuniform heating by high-intensity focused ultrasound (HIFU) or microwave ablation. This is because the CBE image behaves in the same manner as a speckle image, reducing sensitivity and contrast for illustration of the temperature profile.

Clinical application of CBE imaging during hyperthermia and other thermal therapies might, therefore, require a different imaging method for guidance of the tissue ablation process based on the CBE concept. This study investigated a new CBE imaging method based on the mathematic polynomial approximation of the integrated CBE (ICBE_{pa}) estimated using the sliding window technique, which have resolved the limitations of the conventional CBE image.

In the next section, we introduce the theoretical background of the CBE image and present the concept and details of the new CBE imaging method. Then, we describe the experimental procedures used to validate the feasibility of the proposed method. The results are presented for discussion. The impact and contributions of this study are summarized in conclusion.

2. Methods

2.1. Conventional CBE Imaging Method. Previous studies have extensively investigated the temperature dependence of the CBE and the CBE imaging algorithm [6, 10–14]. According to the above literatures, we briefly review the principle of the CBE. Changes in backscattered energy with temperature

are primarily caused by thermal effects on the backscatter coefficient. The temperature dependence of the backscattered energy can be simplified by normalizing it to the baseline value obtained at a reference temperature (typically 37°C), removing the influence of factors with little or no temperature dependence. The CBE, as a function of temperature for a single scatterer, can then be approximated as the ratio of the temperature-dependent backscatter coefficients (η values) at temperature T and reference temperature T_R :

$$\frac{\eta(T)}{\eta(T_R)} = \left(\left(\frac{\rho_m c(T)_m^2 - \rho_s c(T)_s^2}{\rho_s c(T)_s^2} \right)^2 + \frac{1}{3} \left(\frac{3\rho_s - 3\rho_m}{2\rho_s + \rho_m} \right)^2 \right) \times \left(\left(\frac{\rho_m c(T_R)_m^2 - \rho_s c(T_R)_s^2}{\rho_s c(T_R)_s^2} \right)^2 + \frac{1}{3} \left(\frac{3\rho_s - 3\rho_m}{2\rho_s + \rho_m} \right)^2 \right)^{-1}, \quad (1)$$

where ρ is the mass density, $c(T)$ is the temperature-dependent sound speed, and the m and s subscripts refer to the medium and scatterer, respectively. From the model described in (1), it can be predicted that the backscattered energy contributed by lipid-based scatterers would increase with increasing temperature, whereas that corresponding to aqueous scatterers would decrease [10–12].

The algorithmic procedure used to form the CBE temperature image has been described previously [13, 14]. In brief, the speckle motions (echo shift) caused by changes in sound speed and tissue thermal expansion were tracked and compensated by maximizing the cross-correlation between images obtained at adjacent temperatures. Optimization and image resampling were performed to eliminate the dependence of the image on the spatial sampling period. Envelope data of the compensated images at each temperature were obtained using Hilbert transform. Envelope values were squared to determine the backscattered energy. The CBE image was then obtained by calculating the ratio of the backscattered energy at each temperature relative to the reference at each pixel.

2.2. Proposed CBE Imaging Method. The proposed algorithm for CBE imaging first used a square window within the envelope image at temperature T to collect the regional backscattered envelopes $h(T)$. If $E[\cdot]$ denotes the statistical mean, then the regional CBE value (in decibels; dB), calculated using the data acquired by the window (CBE_w), compared to the reference temperature T_R , can be calculated using

$$\text{CBE}_w = 10 \cdot \log_{10} \left(\frac{E[h(T)^2]}{E[h(T_R)^2]} \right). \quad (2)$$

The regional CBE_w was assigned as the new pixel located in the center of the window. The described process was repeated with the window moving throughout the entire envelope image in steps of a certain number of pixels determined by the window overlap ratio (WOR), yielding the CBE_w image as the map of regional CBE_w values.

The absolute value map of the CBE_w image was then used as the integrated CBE (ICBE) image. The ICBE map needs further processing for visualization of temperature distributions and heat transfer in ablated tissue during nonuniform heating. Previous studies have extensively used the mathematic polynomial approximation to fit experimental data and predict temperature distribution and heat conduction behavior [19–21]. This study applied the polynomial approximation during ICBE image processing. Suppose that the original ICBE image prior to smoothing is $X_{i,j}$, where i and j are indices of the image depth and width, respectively. We assumed that the function in each direction was a polynomial of order p . Because p is much smaller than the number of pixels in the axial and lateral directions, the $X_{i,j}$ data were used to determine the optimal polynomial using the least-squares method. $X_{i,j}$ was replaced with the value calculated by the optimal polynomial. This approximation was performed along each line in the axial and lateral direction, with $f_p(\cdot; V)$ being the optimal polynomial of order p reconstructed from the vector $V = (V_1, V_2, \dots, V_n)$ located at indices $1, 2, \dots, n$. After applying polynomial approximations in the lateral and axial directions, image $\bar{X}_{i,j}$ was constructed using the following two procedures:

$$\begin{aligned} X_{i,j}^* &= f_p(i; X_{1:n_d,j}), \quad \text{for each } j, \\ \bar{X}_{i,j} &= f_p(j; X_{i,1:n_w}^*), \quad \text{for each } i, \end{aligned} \quad (3)$$

where n_d and n_w are the numbers of pixels in the axial (depth) and lateral (width) directions, respectively, $X_{1:n_d,j}$ is the vector $X_{1,j}, X_{2,j}, \dots, X_{n_d,j}$, $X_{i,j}^*$ is the intermediate image, and $\bar{X}_{i,j}$ is the $ICBE_{pa}$ image.

3. Experimental Verification

3.1. Ablation Experiments. The feasibility of the proposed method to monitor the distribution of temperature during nonuniform heating was evaluated by conducting tissue ablation experiments on excised tissues. The tissue sample was prepared from pork tenderloin extracted from the psoas major muscle along the central spine. Tissue ablation was conducted using a microwave delivery system (UMC-1, Chinese PLA General Hospital, Institute 207 of the Aerospace Industry Company, Beijing, China) that operates at a frequency of 2.45 GHz and has electrical power ranging from 1 to 99 W. The tenderloin sample was preheated by a temperature-regulated water tank to an initial reference temperature of 37°C. The microwave antenna was then inserted into the sample for irradiation. Ablation treatment performed at 2 W for 420 s produced significant and stable increases in temperature. A commercial ultrasound scanner (Model 2000, Terason, Burlington, MA, USA) that can output raw RF signals digitized at a sampling rate of 30 MHz was used to image the tissue during heating. A wideband linear array probe (Model 10L5, Terason) with a central frequency of approximately 7 MHz was used. A pulse echo test of the transducer showed that the pulse length was 0.7 mm. The image raw data were acquired every 20 s. Each image consisted of

128 scan lines of backscattered signals, and Hilbert transform was applied to each scan line to obtain the corresponding envelope image. The temperature as a function of ablation time was measured using a thermocouple that was attached to the microwave antenna. Measurements of five tissue samples were performed. The experimental setup is shown in Figure 1.

3.2. Data Analysis. The envelope signals obtained from tissue samples were used for B-mode and CBE imaging. The B-mode image formation was based on the log-compressed envelopes with a dynamic range of 60 dB. A sliding square window with side lengths corresponding to one pulse length (0.7 mm) was selected to construct the CBE_w , ICBE, and $ICBE_{pa}$ images. To evaluate the performances of the new CBE image in temperature estimation, the image data were used to calculate the pixel magnitude as a function of heating time. Moreover, the contrast-to-noise ratio (CNR) was calculated as an estimate of the contrast resolution, defined as

$$CNR = \frac{|\mu_{\text{ablation region}} - \mu_{\text{background}}|}{\sigma_{\text{ablation region}} + \sigma_{\text{background}}}, \quad (4)$$

where μ and σ are the mean and standard deviation of the pixel values in the images, respectively. The above quantitative data analyses were based on data acquired from the regions of interest (ROI) located in the background and the ablation zone. The sizes of the ROI were 5 mm \times 5 mm.

4. Results

Figure 2 shows the temperature as a function of ablation time and the typical image for the cross-section of pork tenderloin after microwave ablation. The temperature in the ablation region surrounding the antenna increased from approximately 37°C to 46°C during heating. In the end of ablation, a tissue denaturation region with a roughly circular shape with a diameter of about 1 cm was formed in the tissue background. Figure 3 shows typical B-scans of pork tenderloin obtained during microwave ablation and the corresponding CBE_w images (a WOR of 80% was used). The brightness of the red-blue interlaced shading in the CBE_w image gradually increased with increasing temperature. Figure 4 shows the results of the ICBE image and the average ICBE as a function of heating time. The brightness of the ICBE image increased during heating, corresponding to the average ICBE value increase from 0 dB to 4 dB.

Figure 5(a) shows the results of the $ICBE_{pa}$ images (using order 7). We observed that the brightness of the $ICBE_{pa}$ image gradually increased during heating for 420 s, with the average $ICBE_{pa}$ value increasing from 0 dB to approximately 2 dB, as shown in Figure 5(b). This demonstrated that the $ICBE_{pa}$ image can visualize the temperature distribution in the tissue. To evaluate the enhancement of the contrast after applying polynomial approximation, the curves of the CNR were plotted as a function of heating time in Figure 6. The dynamic range of the CNR during the heating for the ICBE image was approximately 1.6. In contrast, the dynamic range of the CNR for the $ICBE_{pa}$ image was 13.4. The $ICBE_{pa}$ image,

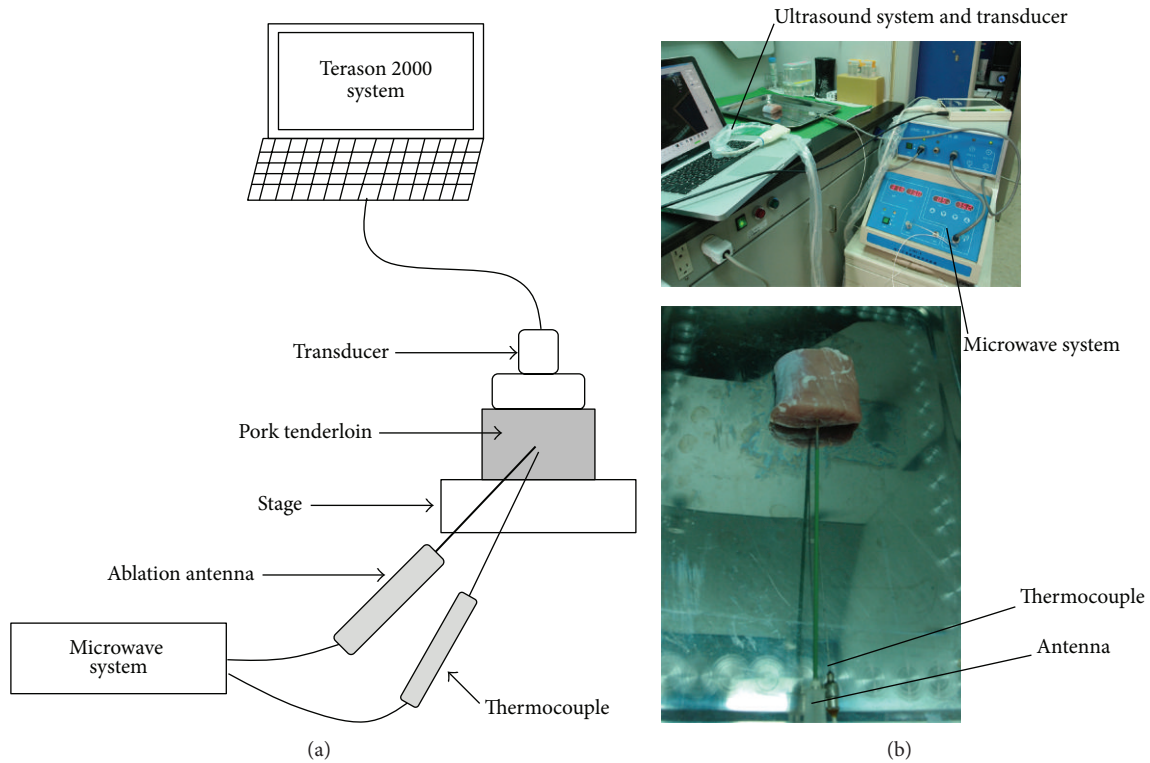


FIGURE 1: (a) Schematic diagram of the experimental setup. (b) A real representation of the experimental setup.

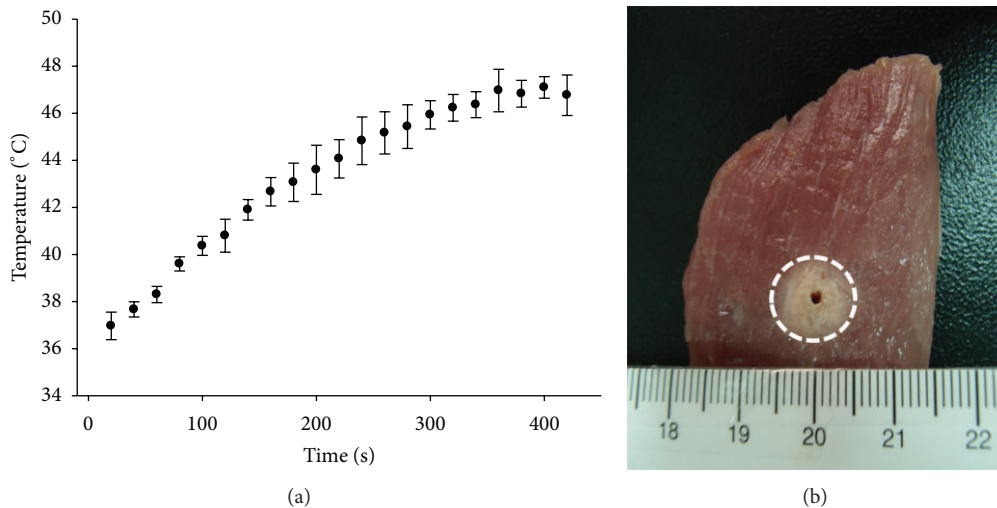


FIGURE 2: Temperature measurement during microwave ablation and the typical image of tissue section after ablation.

thus, allows the temperature profile to be visualized with excellent image contrast.

Figure 7 shows examples of the CBE_w , $ICBE$, and $ICBE_{pa}$ images postheating for 400 s, using WORs of 20%, 50%, and 80%, respectively. We observed that a lower WOR degraded the resolutions of the CBE_w and $ICBE$ images because of the use of fewer pixels to form the image. However, the features and patterns of the $ICBE_{pa}$ image did not exhibit significant changes, with the $ICBE_{pa}$ image still well-describing the contour of the temperature distribution. Figure 8 displays

$ICBE_{pa}$ images of pork tenderloin obtained postheating for 400 s, using polynomial approximations of different orders. Compared with the cross-sections of pork tenderloin shown in Figure 2, the $ICBE_{pa}$ image might overestimate the temperature distribution when using lower order polynomial approximations. The $ICBE_{pa}$ image might reflect the actual temperature distribution when using polynomial approximations of orders of 6 to 7, whereas using higher order polynomial approximations might underestimate the range of the temperature distribution.

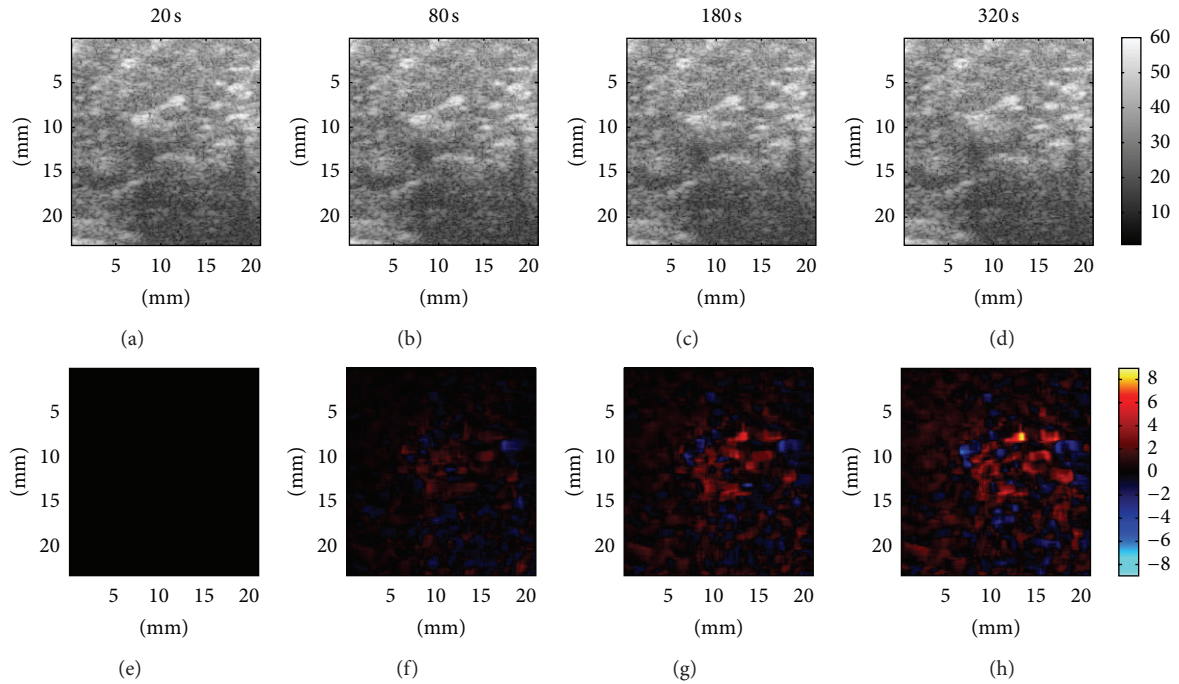


FIGURE 3: ((a)–(d)) Typical B-mode images of pork tenderloin obtained at different heating times and the corresponding ((e)–(h)) CBE_w images.

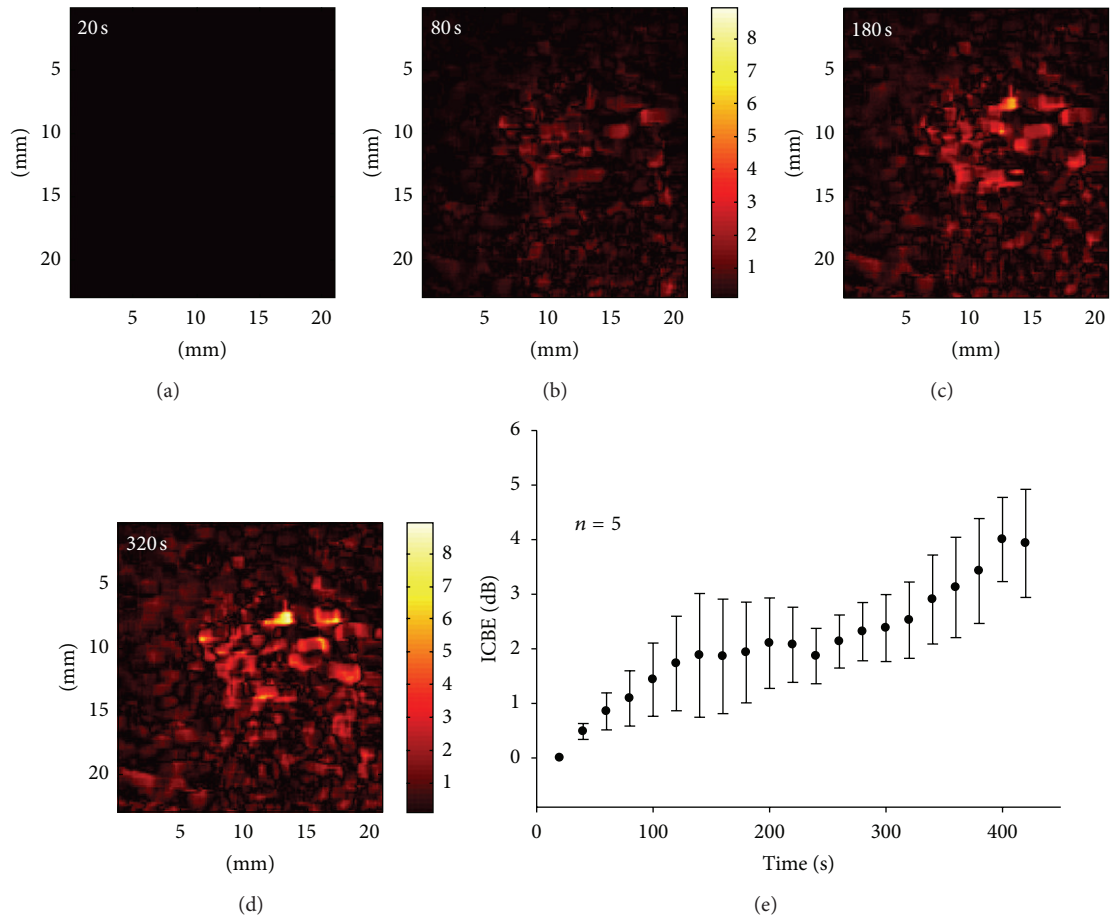


FIGURE 4: ((a)–(d)) Typical ICBE images obtained at different heating times; (e) ICBE values as a function of heating time.

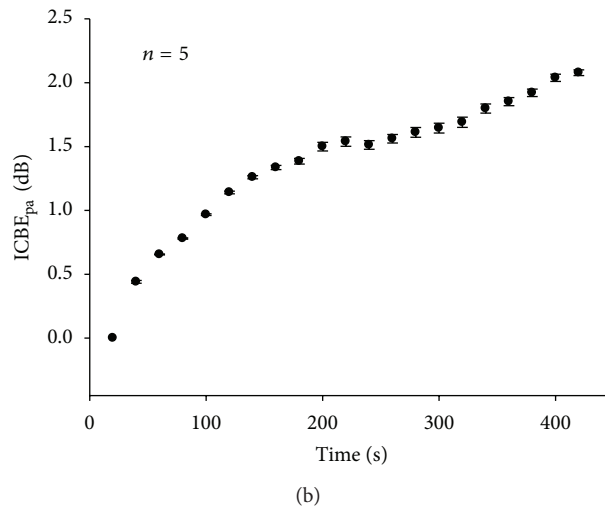
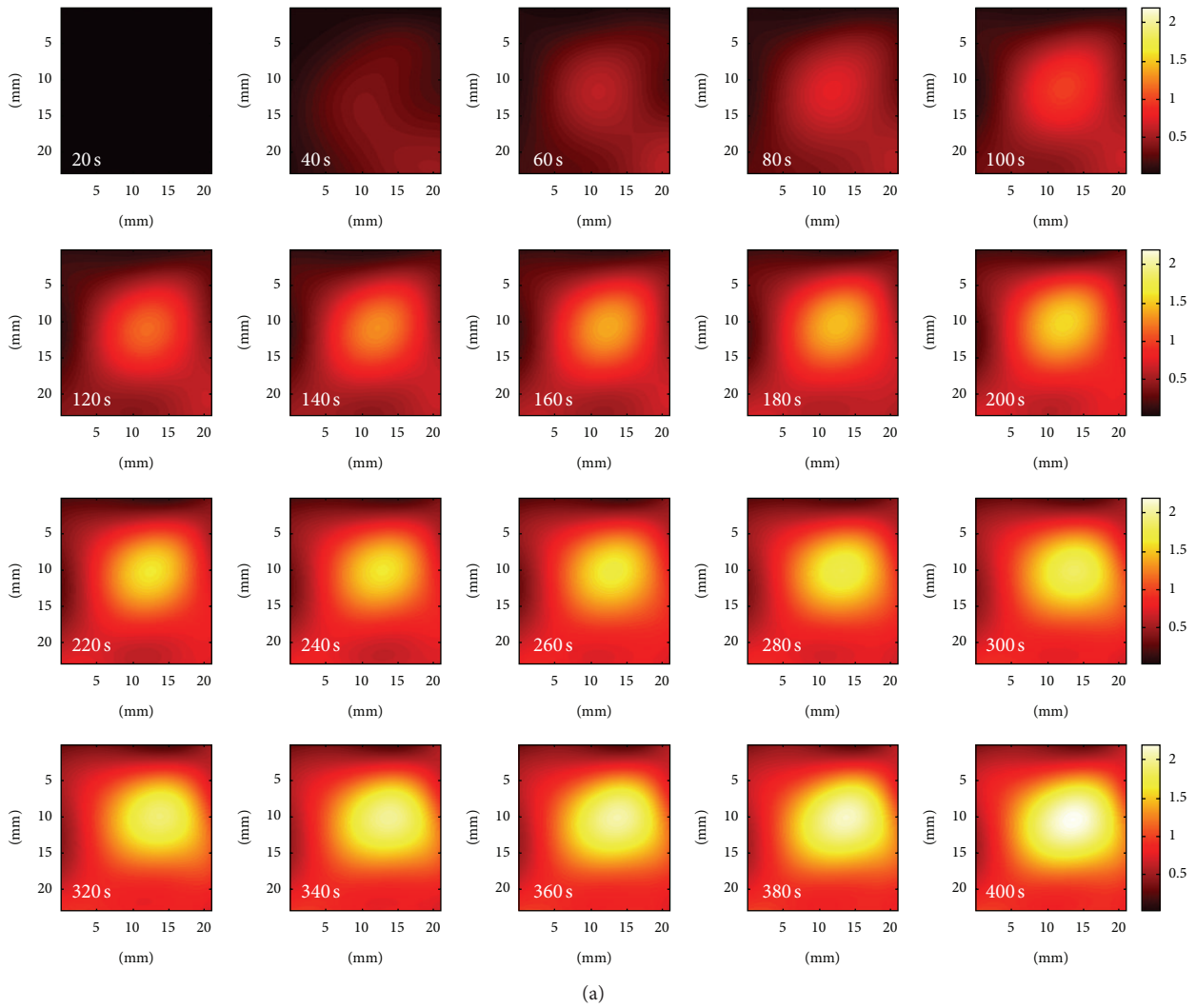


FIGURE 5: (a) Examples of $ICBE_{pa}$ images of pork tenderloin obtained at different heating times; (b) $ICBE_{pa}$ values obtained in the tissue ablation experiments as a function of heating time.

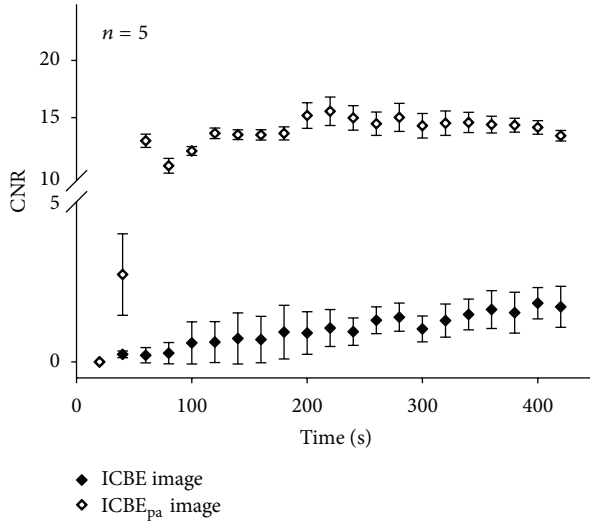


FIGURE 6: Contrast-to-noise ratios as functions of heating times for ICBE and ICBE_{pa} images.

5. Discussion

5.1. The Significance of This Study. Implementing real-time temperature imaging based on the CBE concept in different clinical applications requires the development of a new CBE imaging method to overcome the limitations of conventional CBE imaging. In our opinion, CBE imaging for clinical purposes should have two essential features: (i) reduced dependency of the image performance on echo shift tracking and compensation, with no requirement for echo shift compensation being the objective, and (ii) the ability to visualize the contour of temperature distribution during nonuniform heating, enabling its application in guidance of tissue ablation. The current results have demonstrated that the proposed CBE imaging method fulfills the above two requirements.

5.2. Window Size for Constructing the Proposed CBE Imaging. In our proposed CBE imaging method, the algorithm replaces the pixel-to-pixel calculation with a “region-to-region” calculation. The reason is that using data within a windowed region reflected average trend of backscattered energy, which may reduce the influence of echo shifts and waveform distortion due to heating tissues. Under this assumption, how to select an appropriate window size for regional CBE computation is a key determination to implement visualization of temperature distributions in the absence of echo shift tracking and compensation. According to the analysis by Seip and Ebbini [22], the movement of a scatterer caused by thermal expansion when the temperature increases from 37°C to 50°C is typically less than 2 μm. Over this temperature range, the maximum speckle motion caused by changes in the sound speed for different types of tissues is approximately 0.5 mm in the axial and lateral directions [13]. In this study, the side length of the square window used for regional CBE computation was determined by the pulse length of the used transducer, which

is larger than the maximum echo shift between 37°C and 50°C revealed in the previous study. In this circumstance, the resolution of the CBE image constructed using the sliding window technique is actually not enough to describe the behavior of echo shift. This may be the reason why our CBE imaging methodology can work without echo shift tracking and compensation.

5.3. Polynomial Approximation of the CBE Image. The idea for the proposed algorithmic procedure is similar to the concept of ultrasound Doppler imaging. We can better understand the spirit of the new CBE imaging method from the comparison with Doppler ultrasound. The Doppler shift signals in color Doppler ultrasound imaging are presented in color and superimposed on grayscale images to reflect blood flow information associated with velocity and direction. Limitations of the color Doppler ultrasound image include angle dependence, aliasing, and insensitivity to slow flows [23]. These limitations are less significant in power Doppler images that include positive and negative components of the Doppler shift signals [23, 24].

As discussed, the ultrasound CBE increases with increasing temperature for lipid-based scatterers and decreases with increasing temperature for aqueous scatterers. Similar to the shadings of color Doppler ultrasound corresponding to different flow directions, the conventional CBE image typically also has two shadings: one for lipid-based scatterers (increasing CBE) and the other for aqueous scatterers (decreasing CBE). However, these two shading types can be ambiguous if CBE imaging is performed without echo shift tracking and compensation. This shading ambiguity could be treated as the aliasing effect of the CBE image, which is similar to the aliasing effect caused by an insufficient pulse repetition rate in color Doppler ultrasound. Like the concept of power Doppler ultrasound, the ICBE image is formed by integrating the positive and negative CBE values as the strengths. In this condition, the ICBE image cannot reflect the properties of scatterers in a tissue (lipid-based or aqueous). Nevertheless, it may be treated as an aliasing-independent CBE image to provide a better sensitivity and contrast for the depiction of temperature distribution in a nonuniform heating region.

However, we found that the speckle-like features in the ICBE image still hinder improving the performance of temperature profile visualization. The ICBE image has the ability to describe the temperature distribution in ablated tissues, but it did not have a relatively high CNR. In the contrary, the speckle-free ICBE_{pa} image had a larger CNR, demonstrating that the polynomial approximation provides the ICBE image with the ability to highlight the region and location of ablation by reflecting temperature information with very good contrast.

5.4. Considerations on Performing Polynomial Approximation of the CBE Image. Some aspects of the algorithmic parameters for construction of the ICBE_{pa} image require further discussion to point out some considerations in practice. At first, our results demonstrated that the WOR did not significantly affect the ICBE_{pa} image. This suggested that constructing

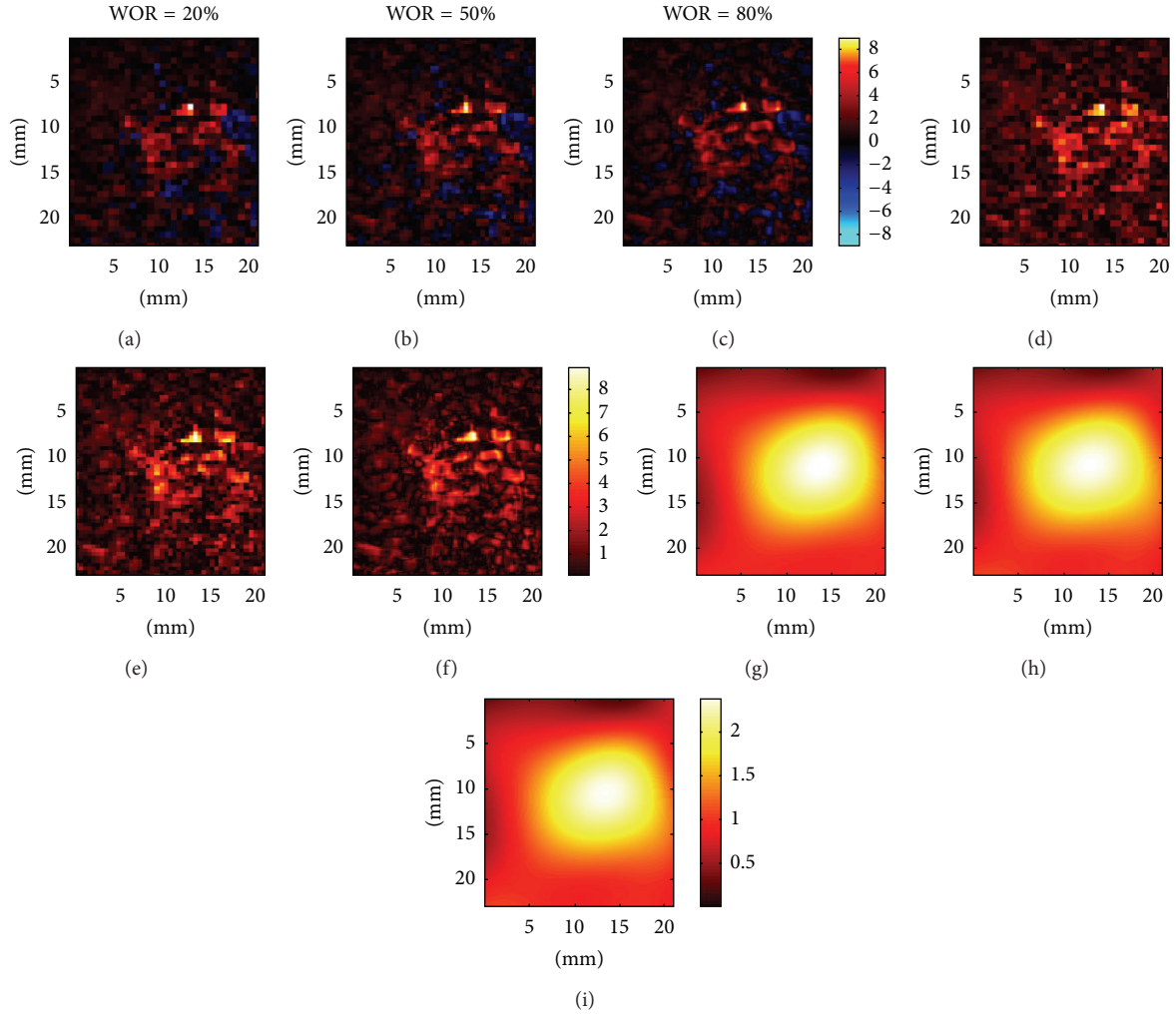


FIGURE 7: Examples of ((a)–(c)) CBE_w , ((d)–(f)) ICBE, and ((g)–(i)) $ICBE_{pa}$ images of pork tenderloin postheating for 400 s, constructed using WORs of 20%, 50%, and 80%, respectively.

the $ICBE_{pa}$ temperature image using a lower WOR is feasible to reduce the computational load. Second, the order selection of conducting polynomial approximation would affect the accuracy of estimations of the effective range and size of the temperature profile for the transfer of heat in ablated tissue [25]. This difficulty can be confirmed by our experimental results, indicating that using an inappropriate order for the polynomial approximation can result in overestimation or underestimation of the temperature profile. Some previous studies have also shown that using a polynomial might not be robust to outliers, which can cause fitting errors in ultrasound data [26, 27]. Future studies should aim to explore the optimal polynomial approximation for producing clinical $ICBE_{pa}$ images.

5.5. Limitations and Future Work. For temperature elevations higher than 45°C , the major limitation of ultrasound temperature estimation comes from the irreversible changes in the acoustic properties of tissue caused by necrosis. This may explain why the image parameter and the temperature

do not have a linear relationship. On the other hand, the proposed CBE image is dedicated to the visualization of the temperature distribution in a tissue. Absolute temperature values are unavailable from the reading of the proposed CBE image. However, this limitation may be overcome by establishing a calibration table for further applications of temperature measurements.

It is worth noting that the construction of the proposed CBE imaging method just needs raw RF signals acquired from a standard pulse-echo ultrasound system and does not require echo shift compensation. This implies that the algorithm of the proposed CBE imaging method can be combined with most commercial ultrasound systems, making it possible to implement real-time temperature imaging. However, the frame rate of real-time temperature imaging is difficult to estimate in the current stage, because the computational efficiency may depend on system specifications and programming skills. In future developments, we would suggest using hardware and parallel processing techniques as the algorithmic kernel to make the frame rate of temperature imaging close to that of ultrasound B-scan.

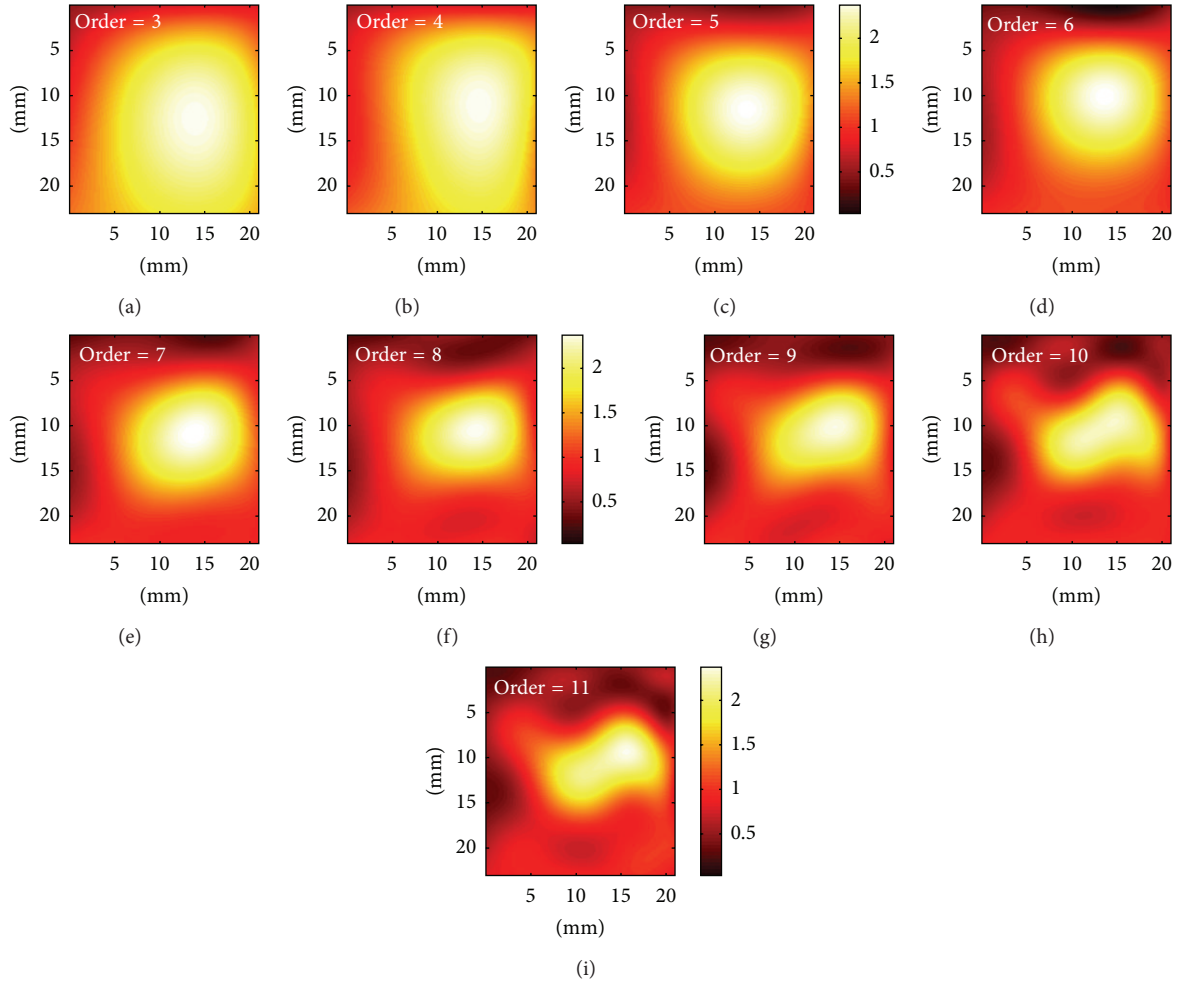


FIGURE 8: ((a)–(i)) Examples of $ICBE_{pa}$ images of pork tenderloin postheating for 400 s, constructed using polynomial approximations of different orders.

6. Conclusion

In this study, we have proposed a new CBE imaging method based on the combination of the sliding window technique and the polynomial approximation (i.e., $ICBE_{pa}$ image) to successfully implement the visualization of temperature distribution in the ablated tissue. The $ICBE_{pa}$ approach is an aliasing-independent and speckle-free temperature image that visualizes temperature profile with no requirement for echo shift tracking and compensation, indicating the potential clinical application of CBE imaging in guidance of tissue ablation and other thermal therapies.

Acknowledgments

This work was supported in part by the National Science Council (Taiwan) under Grant no. NSC100-2628-E-182-003-MY2 and the Chang Gung Memorial Hospital (Linkou, Taiwan) under Grant no. CMRPD1C0161. This work was also supported by the Chang Gung Medical Research Program (CMRP) for Proton Therapy Basic Research (Grant no. CMRPD1C0661).

References

- [1] S.-H. Wang, C.-W. Wei, S.-H. Jee, and P.-C. Li, “Quantitative thermal imaging for plasmonic photothermal therapy,” *Journal of Medical and Biological Engineering*, vol. 31, no. 6, pp. 387–393, 2011.
- [2] E. L. Jones, J. R. Oleson, L. R. Prosnitz et al., “Randomized trial of hyperthermia and radiation for superficial tumors,” *Journal of Clinical Oncology*, vol. 23, no. 13, pp. 3079–3085, 2005.
- [3] E. G. Moros, P. M. Corry, and C. G. Orton, “Thermoradiotherapy is underutilized for the treatment of cancer,” *Medical Physics*, vol. 34, no. 1, pp. 1–4, 2007.
- [4] J. Gellermann, W. Włodarczyk, A. Feussner et al., “Methods and potentials of magnetic resonance imaging for monitoring radiofrequency hyperthermia in a hybrid system,” *International Journal of Hyperthermia*, vol. 21, no. 6, pp. 497–513, 2005.
- [5] B. D. De Senneville, B. Quesson, and C. T. W. Moonen, “Magnetic resonance temperature imaging,” *International Journal of Hyperthermia*, vol. 21, no. 6, pp. 515–531, 2005.
- [6] R. M. Arthur, D. Basu, Y. Guo, J. W. Trobaugh, and E. G. Moros, “3-D in vitro estimation of temperature using the change in backscattered ultrasonic energy,” *IEEE Transactions*

- on *Ultrasonics, Ferroelectrics, and Frequency Control*, vol. 57, no. 8, pp. 1724–1733, 2010.
- [7] R. Maass-Moreno and C. A. Damianou, “Noninvasive temperature estimation in tissue via ultrasound echo-shifts. Part I. Analytical model,” *Journal of the Acoustical Society of America*, vol. 100, no. 4, pp. 2514–2521, 1996.
- [8] R. Maass-Moreno, C. A. Damianou, and N. T. Sanghvi, “Non-invasive temperature estimation in tissue via ultrasound echo-shifts. Part II. In vitro study,” *Journal of the Acoustical Society of America*, vol. 100, no. 4, pp. 2522–2523, 1996.
- [9] C. A. Damianou, N. T. Sanghvi, F. J. Fry, and R. Maass-Moreno, “Dependence of ultrasonic attenuation and absorption in dog soft tissues on temperature and thermal dose,” *Journal of the Acoustical Society of America*, vol. 102, no. 1, pp. 628–634, 1997.
- [10] W. L. Straube and R. Martin Arthur, “Theoretical estimation of the temperature dependence of backscattered ultrasonic power for noninvasive thermometry,” *Ultrasound in Medicine and Biology*, vol. 20, no. 9, pp. 915–922, 1994.
- [11] R. M. Arthur, W. L. Straube, J. D. Starman, and E. G. Moros, “Noninvasive temperature estimation based on the energy of backscattered ultrasound,” *Medical Physics*, vol. 30, no. 6, pp. 1021–1029, 2003.
- [12] R. M. Arthur, W. L. Straube, J. W. Trobaugh, and E. G. Moros, “Non-invasive estimation of hyperthermia temperatures with ultrasound,” *International Journal of Hyperthermia*, vol. 21, no. 6, pp. 589–600, 2005.
- [13] R. M. Arthur, J. W. Trobaugh, W. L. Straube, and E. G. Moros, “Temperature dependence of ultrasonic backscattered energy in motion-compensated images,” *IEEE Transactions on Ultrasonics, Ferroelectrics, and Frequency Control*, vol. 52, no. 10, pp. 1644–1652, 2005.
- [14] J. W. Trobaugh, R. M. Arthur, W. L. Straube, and E. G. Moros, “A simulation model for ultrasonic temperature imaging using change in backscattered energy,” *Ultrasound in Medicine and Biology*, vol. 34, no. 2, pp. 289–298, 2008.
- [15] C. Simon, P. Vanbaren, and E. S. Ebbini, “Two-dimensional temperature estimation using diagnostic ultrasound,” *IEEE Transactions on Ultrasonics, Ferroelectrics, and Frequency Control*, vol. 45, no. 4, pp. 1088–1099, 1998.
- [16] H.-L. Liu, M.-L. Li, T.-C. Shih et al., “Instantaneous frequency-based ultrasonic temperature estimation during focused ultrasound thermal therapy,” *Ultrasound in Medicine and Biology*, vol. 35, no. 10, pp. 1647–1661, 2009.
- [17] X. Liu, X. Gong, C. Yin, J. Li, and D. Zhang, “Noninvasive estimation of temperature elevations in biological tissues using acoustic nonlinearity parameter imaging,” *Ultrasound in Medicine and Biology*, vol. 34, no. 3, pp. 414–424, 2008.
- [18] P.-H. Tsui, Y.-T. Chien, H.-L. Liu, Y.-C. Shu, and W.-S. Chen, “Using ultrasound CBE imaging without echo shift compensation for temperature estimation,” *Ultrasonics*, vol. 52, pp. 925–935, 2012.
- [19] I. C. Enoch, E. Ozil, and R. C. Birkebak, “Polynomial approximation solution of heat transfer by conduction and radiation in a one-dimensional absorbing, emitting, and scattering medium,” *Numerical Heat Transfer*, vol. 5, no. 3, pp. 353–358, 1982.
- [20] P. Keshavarz and M. Taheri, “An improved lumped analysis for transient heat conduction by using the polynomial approximation method,” *Heat and Mass Transfer*, vol. 43, no. 11, pp. 1151–1156, 2007.
- [21] R. Kubota, N. Suetake, E. Uchino, G. Hashimoto, T. Hiro, and M. Matsuzaki, “polynomial-based boundary extraction of plaque in intravascular ultrasound image by using its local statistical information,” *ICIC Express Letters*, vol. 2, pp. 387–393, 2008.
- [22] R. Seip and E. S. Ebbini, “Noninvasive estimation of tissue temperature response to heating fields using diagnostic ultrasound,” *IEEE Transactions on Biomedical Engineering*, vol. 42, no. 8, pp. 828–839, 1995.
- [23] U. M. Hamper, M. R. DeJong, C. I. Caskey, and S. Sheth, “Power doppler imaging: clinical experience and correlation with color doppler US and other imaging modalities,” *Radiographics*, vol. 17, no. 2, pp. 499–513, 1997.
- [24] K. K. Shung, “Diagnostic ultrasound: past, present, and future,” *Journal of Medical and Biological Engineering*, vol. 31, no. 6, pp. 371–374, 2011.
- [25] P. H. Tsui, Y. C. Shu, W. S. Chen, H. L. Liu, I. T. Hsiao, and Y. T. Chien, “Ultrasound temperature estimation based on probability variation of backscatter data,” *Medical Physics*, vol. 39, pp. 2369–2385, 2012.
- [26] G. Ye, J. A. Noble, and P. P. Smith, “A model-based displacement outlier removal algorithm for ultrasonic temperature estimation,” *IEEE Ultrasonics Symposium Proceedings*, pp. 2080–2083, 2008.
- [27] G. Ye, P. P. Smith, and J. A. Noble, “Model-based ultrasound temperature visualization during and following hifu exposure,” *Ultrasound in Medicine and Biology*, vol. 36, no. 2, pp. 234–249, 2010.

Research Article

Automatic Vasculature Identification in Coronary Angiograms by Adaptive Geometrical Tracking

Ruoxiu Xiao,¹ Jian Yang,¹ Mahima Goyal,² Yue Liu,¹ and Yongtian Wang¹

¹ Key Laboratory of Photoelectronic Imaging Technology and System, Ministry of Education of China, School of Optics and Electronics, Beijing Institute of Technology, Beijing 10081, China

² Amity School of Engineering & Technology, Amity University, Noida, Uttar Pradesh 201303, India

Correspondence should be addressed to Jian Yang; jyang@bit.edu.cn

Received 19 July 2013; Accepted 3 September 2013

Academic Editor: Yunmei Chen

Copyright © 2013 Ruoxiu Xiao et al. This is an open access article distributed under the Creative Commons Attribution License, which permits unrestricted use, distribution, and reproduction in any medium, provided the original work is properly cited.

As the uneven distribution of contrast agents and the perspective projection principle of X-ray, the vasculatures in angiographic image are with low contrast and are generally superposed with other organic tissues; therefore, it is very difficult to identify the vasculature and quantitatively estimate the blood flow directly from angiographic images. In this paper, we propose a fully automatic algorithm named adaptive geometrical vessel tracking (AGVT) for coronary artery identification in X-ray angiograms. Initially, the ridge enhancement (RE) image is obtained utilizing multiscale Hessian information. Then, automatic initialization procedures including seed points detection, and initial directions determination are performed on the RE image. The extracted ridge points can be adjusted to the geometrical centerline points adaptively through diameter estimation. Bifurcations are identified by discriminating connecting relationship of the tracked ridge points. Finally, all the tracked centerlines are merged and smoothed by classifying the connecting components on the vascular structures. Synthetic angiographic images and clinical angiograms are used to evaluate the performance of the proposed algorithm. The proposed algorithm is compared with other two vascular tracking techniques in terms of the efficiency and accuracy, which demonstrate successful applications of the proposed segmentation and extraction scheme in vasculature identification.

1. Introduction

World Health Organization's survey of "The top ten causes of death" acknowledged the fact that coronary artery diseases (CADs) are the leading cause of human deaths worldwide. CADs were responsible for 7.25 million deaths in 2008, which accounted for 12.8% of the total deaths worldwide, and this number of deaths has been increasing ever since [1]. The X-ray angiography is an effective technique for imaging of the coronary artery and is considered as the "golden standard" for clinical observation of coronary anatomy and identification of vascular stenosis [2]. Therefore, it is widely used in clinical diagnosis and monitoring of disease. The coronary artery obtained from the X-ray angiograms can provide useful parameters for quantitative assessment and diagnosis of cardiovascular disease. Furthermore, the extraction of coronary arteries from the sequence of angiographic images is an important basis for heart motion analysis [3–5] and

3D vascular reconstruction [6–9]. However, fully automatic, robust, and accurate extraction of coronary artery from angiograms is still a challenging task so far. The main difficulties for the accurate vascular structure extraction or identification in angiograms are as follows: (1) the irregular gray level distribution of blood vessel due to the uneven perfusion of the contrast agent; (2) the nonvascular structures background interference including bones, catheters, and soft tissues; (3) the diversity of direction and width of the vessels; and (4) the commonly existing motion artifacts due to the heart motion and the presence of some pathological lesions.

In the past two decades, a few methods have been studied for the extraction of the blood vessels in angiographic images, such as morphology based methods [10], tracking based methods [11–16], multiscale based, methods [17, 18], edge detection methods, and registration based methods [19, 20]. Among them, the tracking-based methods proved to be very effective, which can detect coronary artery according to the

local response of the angiograms and do not need to scan the whole image. Also, the methods extract the parameters including centerlines, diameter, or bifurcations using an adjustable pattern element to fit incremental section tracking procedures.

For conventional tracking-based algorithm, adapted diameter measurement [11] often suffers from artifacts due to nonuniform contrast distribution of the contrast materials. Diameter measurement approaches have been applied to the single segment and the full vascular network and can produce acceptable quality in the coronary artery extraction [21]. And also, certain new template-based techniques have been introduced [14–16] to fit the coronary artery structure in the tracking procedure, such as rectangular or circular templates [15], Gabor filters [14], and Gaussian kernels [16]. The template-based model construction is known to be complicated and time consuming. Most of them need to create massive templates according to the variation of diameter and direction of coronary artery.

To reduce the calculation complexity, an alternative solution of intensity ridge detection is utilized to approximate the medial axes of the coronary artery. Aylward and Bullitt [12] proposed a centerline tracking algorithm based on ridge detection in multi-scale space, which is constructed by extracting the ridge using eigen decomposition of the Hessian matrix. Zamani Boroujeni et al. [13] employed a ridge scanning scheme for reliable identification of the vessel points and calculating the magnitude by adaptive look-ahead distance method. However, due to the effects of low image quality and noise, ridgeline cannot be exactly located at the geometrical center of coronary artery.

In this paper, an adaptive geometrical vessel tracking (AGVT) algorithm is proposed for the automatic extraction of coronary artery from angiograms. There are two main contributions of this study. First, an automatic initialization algorithm including location and direction of the seed point is proposed. Second, ridge points are recursively detected in consecutive scanlines, which are then adjusted to the geometrical centers according to the estimated diameters. The proposed method does not require any human intervention beforehand and can simultaneously estimate the parameters for quantitative analysis of vasculature including centerlines, diameter, and bifurcations.

2. Methods

The proposed AGVT algorithm is composed of three main steps: ridge enhancement, seeds determination, and adaptive tracking. The brief description of the calculation procedures is as follows.

- (1) Ridge enhancement: the angiogram is first convoluted with a Gaussian kernel with different standard deviation. For each scale of convolution, the blood vessel is enhanced by combination of eigenvalue response of the Hessian matrix, and the maximum responses for each level of scale space are extracted as the RE image. The enhancement procedure guarantees that

the background is suppressed and the vascular structures are highlighted in the RE image.

- (2) Seeds determination: the seed points are detected by scanning of local maximum, for which the intensity is brighter than other points in the local area. The forward and backward tracking directions of the seeds are designed to detect the neighboring ridge points.
- (3) Adaptive tracking: rough centerlines are extracted through sequentially detecting ridge point in RE image, which are then further refined adaptively to the geometric center according to the distance between the vascular boundaries and current calculating point. If the bifurcation is identified by discriminating connecting relationship of the tracked ridge points, the tracking will be divided into two paths for each branch. Termination criteria are assigned to ensure that the tracking is within the region of coronary artery without repetition. Finally, all the detected centerlines are merged and smoothed, and also false tracking results are removed.

2.1. Ridge Enhancement. In this paper, we use a multiscale vascular enhancement filter (MVEF) [22] to obtain the RE image. It enhances all the tubular targets along the centerline and fades out the background. Suppose the $H(p)$ is the Hessian matrix of a point p on image I ; then, the Hessian matrix of the each pixel can be calculated as follows:

$$H(p) = \begin{pmatrix} I_{xx}(p) & I_{xy}(p) \\ I_{yx}(p) & I_{yy}(p) \end{pmatrix}, \quad (1)$$

where subscripts x and y denote the second order derivate along x or y direction. The eigenvalues of the matrix are denoted by λ_1 and λ_2 ($\lambda_1 \leq \lambda_2$). According to the analysis of [22], different eigenvalues of the Hessian matrix are corresponding to different types of structure, such as plate-like, blob-like, tubular, and noises.

In order to detect different size of vessels, Gaussian kernel with different standard deviation is usually convolved with the angiogram [23, 24]. For a certain scale σ , the intensity differential of the point p is expressed as follows:

$$\frac{\partial}{\partial x} I(p, \sigma) = \sigma^\gamma I(p) * \frac{\partial}{\partial x} G(0, \sigma), \quad (2)$$

where γ is the normalization coefficient as defined in [24] and $G(0, \sigma)$ denotes a Gaussian function with the mean of 0 and standard deviation of σ . The σ of the Gaussian kernel is designed as a variant value to enhance different scale of vessels. In implementation, σ is usually designed as a value between the maximum and minimum size of the vascular diameter to be enhanced. The enhancement response of each pixel in scale space is computed, and the maximum response is then utilized as the final enhancement result.

TABLE 1: Quantitative comparison of Aylward, Boroujeni and the proposed algorithms.

Vessels	Aylward algorithm				Boroujeni algorithm				Proposed algorithm			
	Max	Min	Mean	RMS	Max	Min	Mean	RMS	Max	Min	Mean	RMS
V1	1.68	0.04	0.48	0.62	2.28	0.00	0.40	0.60	0.59	0.02	0.27	0.30
V2	2.71	0.02	1.06	1.30	2.82	0.00	0.39	0.65	0.67	0.01	0.28	0.32
V3	3.66	0.06	0.84	1.10	1.19	0.00	0.32	0.44	1.09	0.01	0.28	0.37
V4	3.69	0.03	1.24	1.50	2.21	0.02	0.40	0.64	0.55	0.01	0.21	0.25
V5	2.60	0.26	1.64	1.80	0.96	0.02	0.48	0.55	0.91	0.01	0.41	0.48
V6	2.52	0.24	1.62	1.70	2.10	0.00	0.63	0.80	1.31	0.01	0.41	0.53
V7	3.43	0.04	1.60	1.75	1.94	0.04	0.34	0.49	1.33	0.06	0.29	0.38
V8	3.27	0.02	1.38	1.57	2.07	0.02	0.52	0.86	1.64	0.09	0.47	0.62
V9	3.99	0.22	1.61	1.97	2.67	0.01	0.87	0.87	1.31	0.01	0.41	0.53
Mean	3.06	0.10	1.27	1.48	2.03	0.01	0.48	0.66	1.04	0.03	0.34	0.42

The enhancement response $V(p)$ of pixel p can be calculated as follows:

$$V(p, \sigma) = \begin{cases} 0, & \text{if } \lambda_2 < 0 \\ \exp\left(-\frac{\lambda_1^2}{2\alpha^2\lambda_2^2}\right) \left[1 - \exp\left(-\frac{\lambda_1^2 + \lambda_2^2}{2\beta^2}\right)\right] & \text{otherwise,} \end{cases}$$

$$V(p) = \max_{\sigma_{\min} \leq \sigma \leq \sigma_{\max}} V(p, \sigma), \quad (3)$$

where α and β are control parameters, while $[\sigma_{\min}, \sigma_{\max}]$ is the size of the scale space.

2.2. Seeds Determination

2.2.1. Seed Points. After the ridge enhancement, the local maximum points in the gray level space of the RE image are located on the ridgelines, and they are detected as the initial positions for the tracking. According to [25], if a point (x, y) is a local maximum, then its gradient is equal to zero and its Hessian matrix is negative. However, the points satisfied with these two conditions are usually with float coordinates. Therefore, the seed points need to be interpolated according to their neighboring coordinates.

For any pixel (x, y) and its neighbor pixels $(x+1, y)$, $(x, y+1)$, $(x+1, y+1)$, if there is a point (ξ, η) ($x < \xi < x+1$, $y < \eta < y+1$) that meets the conditions that $\nabla(\xi, \eta) = 0$ and $\lambda_1(\xi, \eta) < 0$, $\lambda_2(\xi, \eta) < 0$, then (ξ, η) is a local maximum on the image. According to the bilinear interpolation equation

$$f(\xi, \eta) = [x+1-\xi \quad x-\xi] \times \begin{bmatrix} f(x, y) & f(x, y+1) \\ f(x+1, y) & f(x+1, y+1) \end{bmatrix} \times \begin{bmatrix} y+1-\eta \\ y-\eta \end{bmatrix}, \quad (4)$$

we have

$$\begin{aligned} \nabla(\xi, \eta) &= [x+1-\xi \quad x-\xi] \\ &\times \begin{bmatrix} \nabla(x, y) & \nabla(x, y+1) \\ \nabla(x+1, y) & \nabla(x+1, y+1) \end{bmatrix} \\ &\times \begin{bmatrix} y+1-\eta \\ y-\eta \end{bmatrix} = 0, \\ \lambda_i(\xi, \eta) &= [x+1-\xi \quad x-\xi] \\ &\times \begin{bmatrix} \lambda_i(x, y) & \lambda_i(x, y+1) \\ \lambda_i(x+1, y) & \lambda_i(x+1, y+1) \end{bmatrix} \\ &\times \begin{bmatrix} y+1-\eta \\ y-\eta \end{bmatrix} < 0, \quad (i = 1, 2). \end{aligned} \quad (5)$$

The solutions of (5) are implicit; hence, the approximate solutions can be solved by calculating the continuity of the image and its differential information. If a point satisfied the following equations:

$$\begin{aligned} \nabla(x, y) \nabla(x+1, y+1) &< 0 \text{ or} \\ \nabla(x+1, y) \nabla(x, y+1) &< 0, \end{aligned} \quad (6)$$

$$\lambda_i(x+m, y+n) < 0, \quad (i = 1, 2, m = 0, 1, n = 0, 1)$$

there will be a point (ξ, η) ($x < \xi < x+1$, $y < \eta < y+1$), which satisfies the conditions $\nabla(\xi, \eta) = 0$ and $\lambda_1(\xi, \eta) < 0$, $\lambda_2(\xi, \eta) < 0$. Due to the continuity of image, (x, y) is an approximate solution of (ξ, η) .

Since there are still numerous noises with low gray value in RE image, the extracted seed points are refined by an intensity threshold τ . If the intensity value of a candidate seed point is below the predefined threshold, it will be discarded.

2.2.2. Tracking Directions. In this section, the initial tracking directions of the detected seed points are obtained in RE image. Suppose that p is a detected seed point, while p^+ and p^- are its neighboring forward (with greater abscissa value) and backward (with smaller abscissa value) points. Then

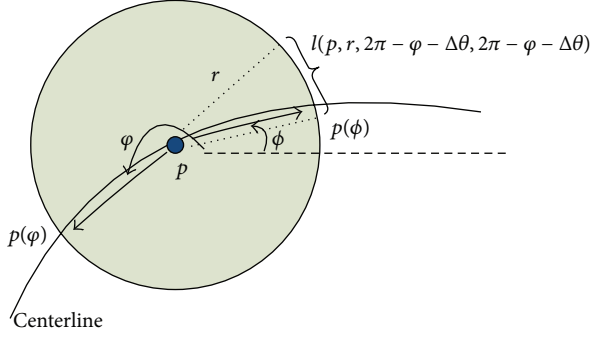


FIGURE 1: Determination of the forward and backward tracking directions for a seed point.

the forward tracking direction $\mathbf{u}(p^+)$ and backward tracking direction $\mathbf{u}(p^-)$ of p can be formulated as

$$\begin{aligned}\mathbf{u}(p^+) &= \frac{p^+ - p}{\|p^+ - p\|}, \\ \mathbf{u}(p^-) &= \frac{p^- - p}{\|p^- - p\|}.\end{aligned}\quad (7)$$

As shown in Figure 1, for a seed point p with coordinate (x_p, y_p) , we define a circle with radius r centered at p , and the points $p(\theta)$ ($p(\theta) = p(x_\theta, y_\theta)$) on the circle can be expressed as parametric equations as follows:

$$x_\theta = x_p + r \cos(\theta), \quad y_\theta = y_p + r \sin(\theta), \quad 0 \leq \theta < 2\pi. \quad (8)$$

As there are two intersections between the circle and the centerline, the intersection points $p(\varphi)$ and $p(\phi)$ hence can be detected by calculating gray level difference along the path of the circle. Here, the point $p(\varphi)$ can be detected by finding the maximum on the circle as follows:

$$\varphi = \arg \max_{\theta \in [0, 2\pi]} I(p(\theta)). \quad (9)$$

Obviously, $p(\varphi)$ is one of the points p^+ or p^- , while $p(\phi)$ can be detected by finding the local maximum on the local arc defined by φ :

$$\phi = \arg \max_{\theta \in [2\pi - \varphi - \Delta\theta, 2\pi - \varphi + \Delta\theta]} I(p(\theta)), \quad (10)$$

where φ and ϕ represent the forward and backward tracking angle of pixel p . $[2\pi - \varphi - \Delta\theta, 2\pi - \varphi + \Delta\theta]$ represents the searching interval. The condition of $\cos(\varphi) \geq 0$ means that $p(\varphi)$ is located at the right side of p .

Since noise is widely scattered over RE image, it is necessary to refine the seed points from the noise. Here, a rectangle with size of $Lx \times Ly$ is constructed on the center of each seed point. Then, if the average intensity within the defined rectangle is below a predefined threshold τ , this seed point is removed.

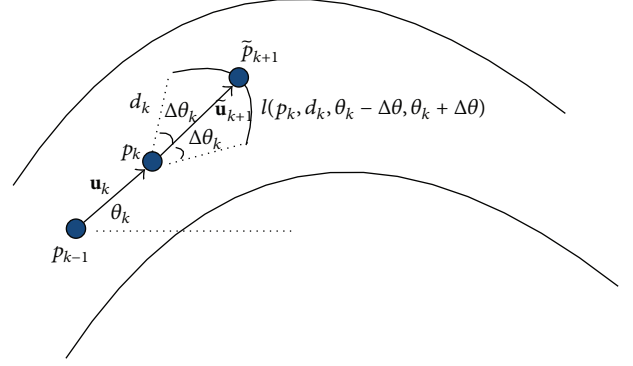


FIGURE 2: The process of ridge tracking.

2.2.3. Adaptive Tracking

(a) *Centerline Updating and Diameter Measurement.* Due to the nonuniform distribution of injected contrast, the ridge-line of vessel cannot be accurately located at the geometrical center of the vessel in angiographic image. Hence, in this paper, we first extract the ridge point in RE image and then adjust it to the geometrical center by geometric symmetry property of the boundaries of the vascular structures.

Figure 2 illustrates the process of ridge tracking. The location and tracking angle of current centerline point are denoted by p_k and θ_k ; then, the relationship between the tracking direction \mathbf{u}_k and tracking angle θ_k is defined as follows:

$$\mathbf{u}_k = (\cos \theta_k, \sin \theta_k). \quad (11)$$

To detect the ridge point \tilde{p}_{k+1} , the intensities of the pixels located on arc $l(p_k, d_k, \theta_k - \Delta\theta, \theta_k + \Delta\theta)$ are enumerated and compared. And the local maximum with intensity equal to the ridge point \tilde{p}_{k+1} can be found as follows:

$$I(\tilde{p}_{k+1}) = \max_{p \in l(d_k, \theta_k - \Delta\theta, \theta_k + \Delta\theta)} I(p), \quad (12)$$

where $2\Delta\theta_k$ is the search scope and d_k is the calculating step size.

Then, the initial tracking direction $\tilde{\mathbf{u}}_{k+1}$ can be defined by p_k and \tilde{p}_{k+1} as follows:

$$\tilde{\mathbf{u}}_{k+1} = \frac{\tilde{p}_{k+1} - p_k}{\|\tilde{p}_{k+1} - p_k\|}. \quad (13)$$

Let \tilde{p}_{k+1} and \hat{p}_{k+1} represent the detected ridge point and its corresponding geometrical centerline point. As shown in Figure 3, the intensity profile $\tilde{g}_{k+1}(s)$ is defined by the scanline of \tilde{p}_{k+1} , which is perpendicular to $\tilde{\mathbf{u}}_{k+1}$. And s is denoted by the curve parameter of $\tilde{g}_{k+1}(s)$.

Hence, two estimated edge points $\tilde{g}_{k+1}(s^+)$ and $\tilde{g}_{k+1}(s^-)$ can be detected according to the gradient information of $\tilde{g}_{k+1}(s)$:

$$\begin{aligned}|\nabla[\tilde{g}_{k+1}(s^+)]| &= \max_{0 < s < D} |\nabla[\tilde{g}_{k+1}(s)]|, \\ |\nabla[\tilde{g}_{k+1}(s^-)]| &= \max_{-D < s < 0} |\nabla[\tilde{g}_{k+1}(s)]|,\end{aligned}\quad (14)$$

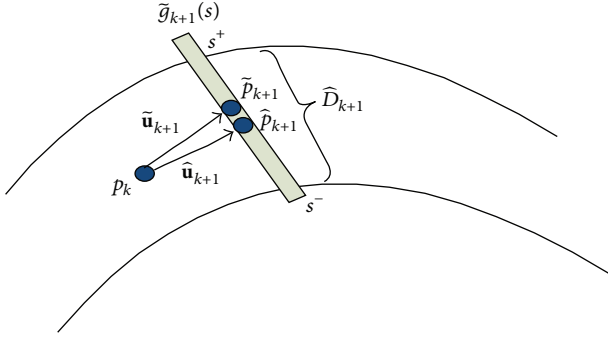


FIGURE 3: Centerline point adjustment and diameter measurement.

where the parameter D is defined as the search size, while $+$ and $-$ denote the upward and downward direction of \tilde{p}_{k+1} , respectively.

Then, we count the average gray value of the vessel points and background to obtain the two corresponding edge points $\tilde{g}_{k+1}(s^+)$ and $\tilde{g}_{k+1}(s^-)$. The average gray value \tilde{V}_{k+1} of the vessel points in the profile $\tilde{g}_{k+1}(s)$ is calculated as follows:

$$\tilde{V}_{k+1} = \frac{1}{\tilde{s}^+ - \tilde{s}^-} \sum_{\tilde{s}^- < s < \tilde{s}^+} \tilde{g}_{k+1}(s). \quad (15)$$

And the average gray value of background \tilde{B}_{k+1} in $\tilde{g}_{k+1}(s)$ is calculated as follows:

$$\tilde{B}_{k+1} = \frac{1}{2D - (\tilde{s}^+ - \tilde{s}^-)} \left(\sum_{-D < s < \tilde{s}^-} \tilde{g}_{k+1}(s) + \sum_{\tilde{s}^+ < s < D} \tilde{g}_{k+1}(s) \right). \quad (16)$$

The two edge points $\tilde{g}_{k+1}(s^+)$ and $\tilde{g}_{k+1}(s^-)$ with gray value less than $(1/2)(\tilde{V}_{k+1} + \tilde{B}_{k+1})$ on either side of \tilde{p}_{k+1} are identified. Then, the geometrical centerline point \hat{p}_{k+1} corresponding to \tilde{p}_{k+1} can be calculated as follows:

$$\hat{p}_{k+1} = \tilde{g}_{k+1} \left(\frac{\tilde{s}^+ + \tilde{s}^-}{2} \right). \quad (17)$$

According to (13), the adjusted tracking direction $\hat{\mathbf{u}}_{k+1}$ of \hat{p}_{k+1} can be then updated as

$$\hat{\mathbf{u}}_{k+1} = \frac{\hat{p}_{k+1} - p_k}{\|\hat{p}_{k+1} - p_k\|}. \quad (18)$$

Once the positions of the two edge points $\tilde{g}_{k+1}(s^+)$ and $\tilde{g}_{k+1}(s^-)$ are determined, the diameter \hat{D}_{k+1} of the centerline point \hat{p}_{k+1} can be measured as

$$\hat{D}_{k+1} = |\hat{s}^+ - \hat{s}^-|. \quad (19)$$

(b) *Bifurcations Identification.* As shown in Figure 4, p_{k-1} and p_k are two detected centerline points in the previous tracking process. If p_k is a bifurcation, then two ridge points \tilde{p}_{k+1}^1 and \tilde{p}_{k+1}^2 can be found on RE image at each branch of the

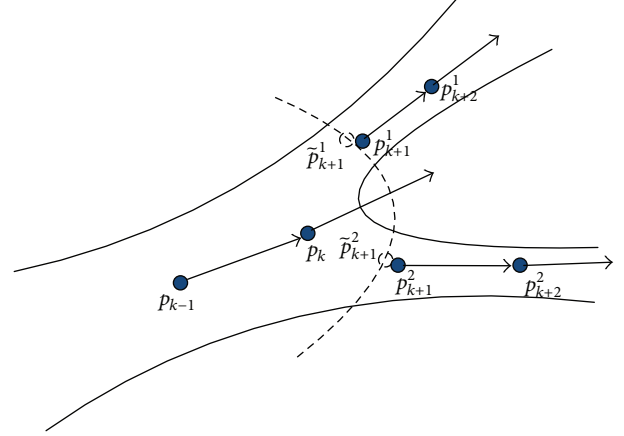


FIGURE 4: Bifurcation identification.

vessel due to the process of MVEF. According to the adaptive tracking described in the previous section, we are able to get two geometrical centerline points p_{k+1}^1 and p_{k+1}^2 . Thereafter, the tracking process is proceeded in the two directions of $\mathbf{u}_{k+1}^1 = (p_{k+1}^2 - p_k) / \|p_{k+1}^2 - p_k\|$ and $\mathbf{u}_{k+1}^2 = (p_{k+1}^1 - p_k) / \|p_{k+1}^1 - p_k\|$.

(c) *Termination Criteria.* The tracking procedure starts from a randomly selected seed point and then iteratively extends to the other seed points. Three termination rules are defined to prevent the tracking path from going out of the image range, or being repeatedly calculated.

- (1) If the detected centerline point goes beyond the scope of the image.
- (2) If the detected centerline point goes beyond the scope of the vessel.
- (3) If the detected centerline point intersects an extracted centerline.

Condition (1) is designed to guarantee that both abscissa value and ordinate value of current calculating point are within the border of the image while condition (2) is designed to ensure that the gray value of current calculating pixel is within the range of the vascular boundaries. Condition (3) is devised to determine if current calculating pixel is being detected or not.

A seed point tracking process is stopped immediately if any of the above three conditions occurs, and a new seed point tracking procedure will be launched. By setting these three conditions, it can be guaranteed that the tracking procedure will be carried out in the region of the blood vessels without repetition.

(d) *Vasculature Refinement.* After all discrete incremental sections are obtained from the angiographic image, vasculature refinement needs to be done to remove the false tracking noise, such as hair-like noise and discrete small edges. All the discrete centerlines are merged into several connected centerline sets, and the short false tracking results are removed by a predefined length threshold. Then, the vessel

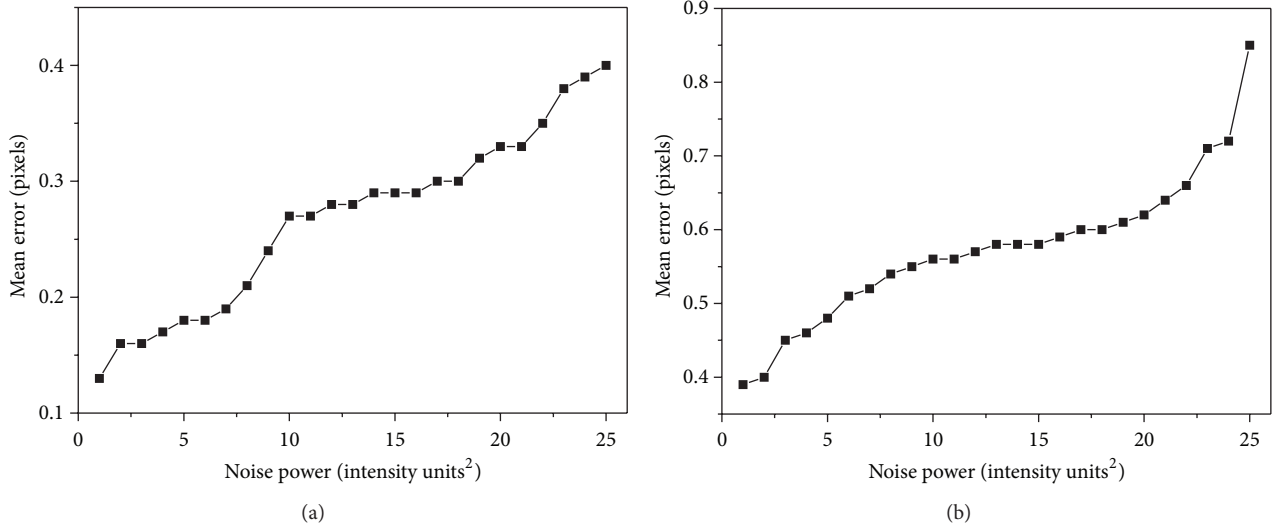


FIGURE 5: Error distribution. (a) Centerline error. (b) Diameter error.

structure with the largest connected components is reserved as the tracking result. To avoid “jagged” tracking phenomenon, the cardinal spline interpolation [26] is used to preserve the smoothness of the tracked paths.

3. Results and Discussion

To validate the performance of the proposed vascular extraction method, series of experiments are designed and tested on both synthetic data and real clinical angiograms. And the comparative evaluation of the results demonstrates the efficiency of the proposed method over the several existing methods. Our tracking algorithm is implemented in Microsoft Visual Studio 2010 on an Intel Core i7 PC (with CPU 3.5 G and 16 G memory), and all the simulated angiographic images are with the resolution of 512×512 .

3.1. Synthetic Data. In order to quantitatively evaluate the performance of the proposed method, a series of angiograms with defined vascular structures are designed and simulated. The angiograms are simulated by projecting 3D synthetic cylindrical segments onto the image plane according to the perspective projection model [27] of the angiography system as developed in [13, 28, 29]. In order to simplify the simulation procedure, the background image is acquired prior to the injection of contrasting substance, so there is no visible vessel or catheter in the obtained image.

The projection intensity of vessel segment model adopted for the simulation comes from [27], which can be defined as follows:

$$p(x) = 2\mu\sqrt{r^2 - x^2}, \quad |x| \leq r, \quad (20)$$

where x is the distance between current point and tentative centerline point, r is the radius of vessel, μ is the linear attenuation coefficient, and $p(x)$ is the intensity of the projected point.

To test the proposed algorithm over noise interference, 25 angiograms containing a single vessel segment with different additive Gaussian noise are generated. The proposed algorithm then proceeds on the simulated image, and the extracted centerline and diameter are compared with the predefined vessel, and the error distributions over different noise scale for the centerline and diameter estimation are shown in Figures 5(a) and 5(b), respectively. From Figure 5 it can be seen that with the adding of noise power, the mean error of the centerline and diameter estimations increase gradually. Specifically, the mean error for centerline estimation ranges from 0.13 pixels to 0.33 pixels for noise power between 1 and 20; while for the diameter, the estimated errors range from 0.39 pixels to 0.62 pixels for noise power between 1 and 20. For noise power of 25, the image is considerably corrupted; however, the tracking centerline and diameter estimation errors are less than 0.4 and 0.9 pixels. It is obvious that the proposed method is every effective and robust even under terrible image qualities.

In order to simulate the vascular stenosis, the diameter is adjusted by a designed exponentially decaying function as formulated as follows [29]:

$$D(l) = D_0 \exp(-al) - \frac{c}{\sigma} \exp\left[-\left(\frac{\pi(l-\mu)^2}{(\sigma c)^2}\right)\right], \quad (21)$$

$$c = D_0 \exp(-a\mu),$$

where D_0 is an initial diameter and a is taper coefficient. μ and σ are Gaussian function parameters. For this calculation, at the stenosis part ($l = \mu$), 100% stenosis can be simulated by setting $\sigma = 1$. Stenosis rate of vessel can computed as follows:

$$\text{stenosis} = \frac{1}{\sigma}. \quad (22)$$

According to (21) and (22), nine types of arterial segments with stenosis are generated, as shown in Figure 6, and

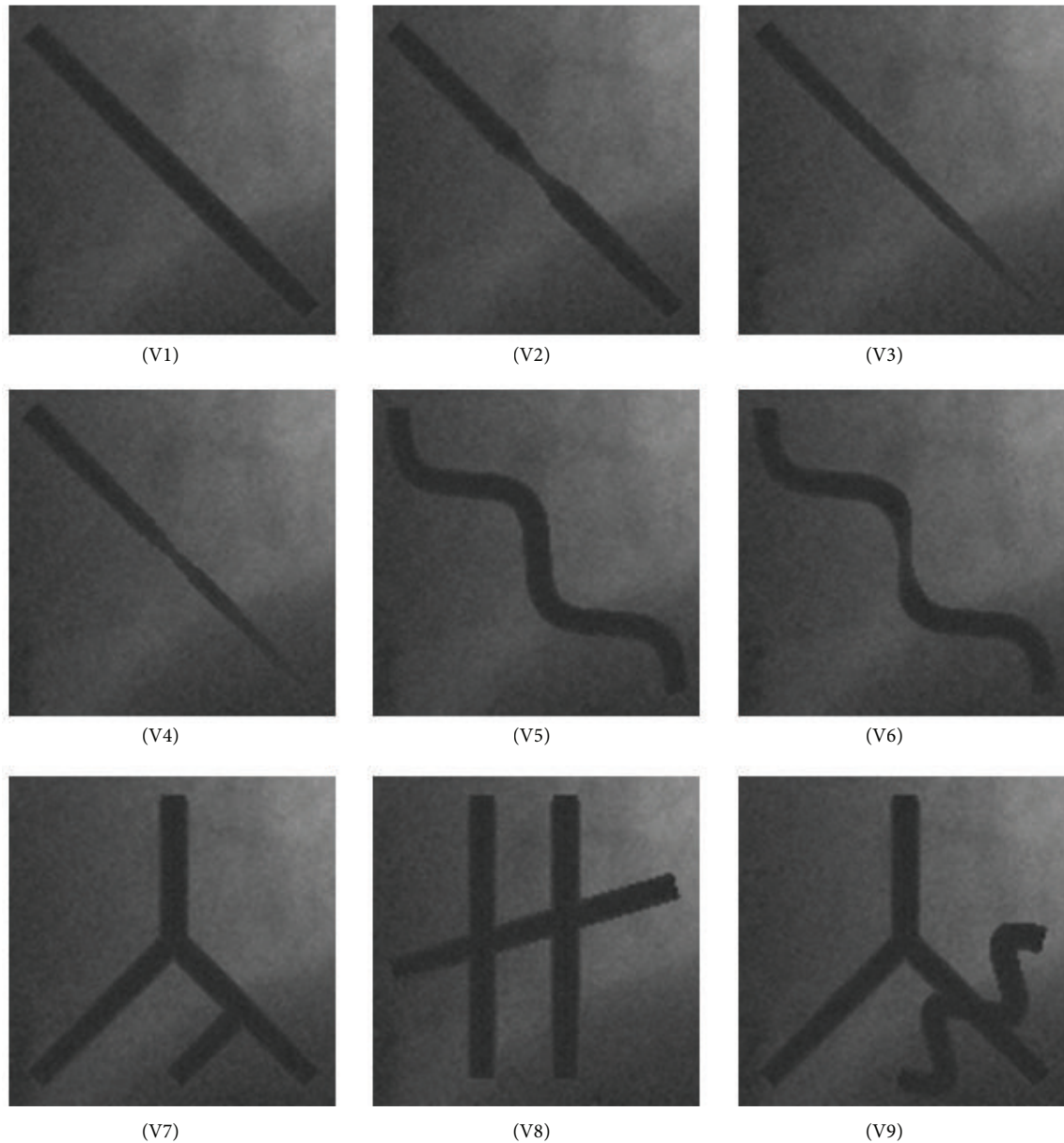


FIGURE 6: Nine types of synthetic arterial segments.

the performance of the proposed algorithm is compared with the other two existing centerline tracking algorithms. To simplify the following description, nine types of arterial segments named V1 to V9 are designed as follows.

(1) V1: vessel with rough parallel boundaries; (2) V2: vessel with the diameter decreased gradually; (3) V3: vessel with curved boundaries, for which the centerline of the vessel is computed by connecting two periods sine functions; (4) V4: V1 with 50% stenosis; (5) V5: V2 with 50% stenosis; (6) V6: V3 with 50% stenosis; (7) V7: vessels with bifurcations; (8) V8: vessels with overlaps; (9) V9: vessels with bifurcation and overlap.

The tracking results of the three algorithms are listed in Table 1, which contains the maximum, minimum, mean, and RMS (root mean square) of the estimated centerline

error. The mean errors are 0.34, 1.27, and 0.48 pixels for the proposed algorithm, Aylward, and Boroujeni algorithms, respectively. The proposed method represents 73.22% and 29.17% improvement over Aylward and Boroujeni algorithms. For the most complex structure V9, the mean tracking error for the proposed algorithm is 0.41 pixels, while it is 1.61 pixels and 0.87 pixels for Aylward and Boroujeni algorithms. The proposed method represents 74.53% and 39.87% improvement over Aylward algorithm and Boroujeni algorithm. Obviously, the proposed algorithm provides a more accurate scheme for coronary artery extraction and identification in X-ray angiograms.

The above experiments are repeatedly tested on 45 groups of synthetic images, for which each type of the vessel structure is randomly generated for five times. For these experiments,

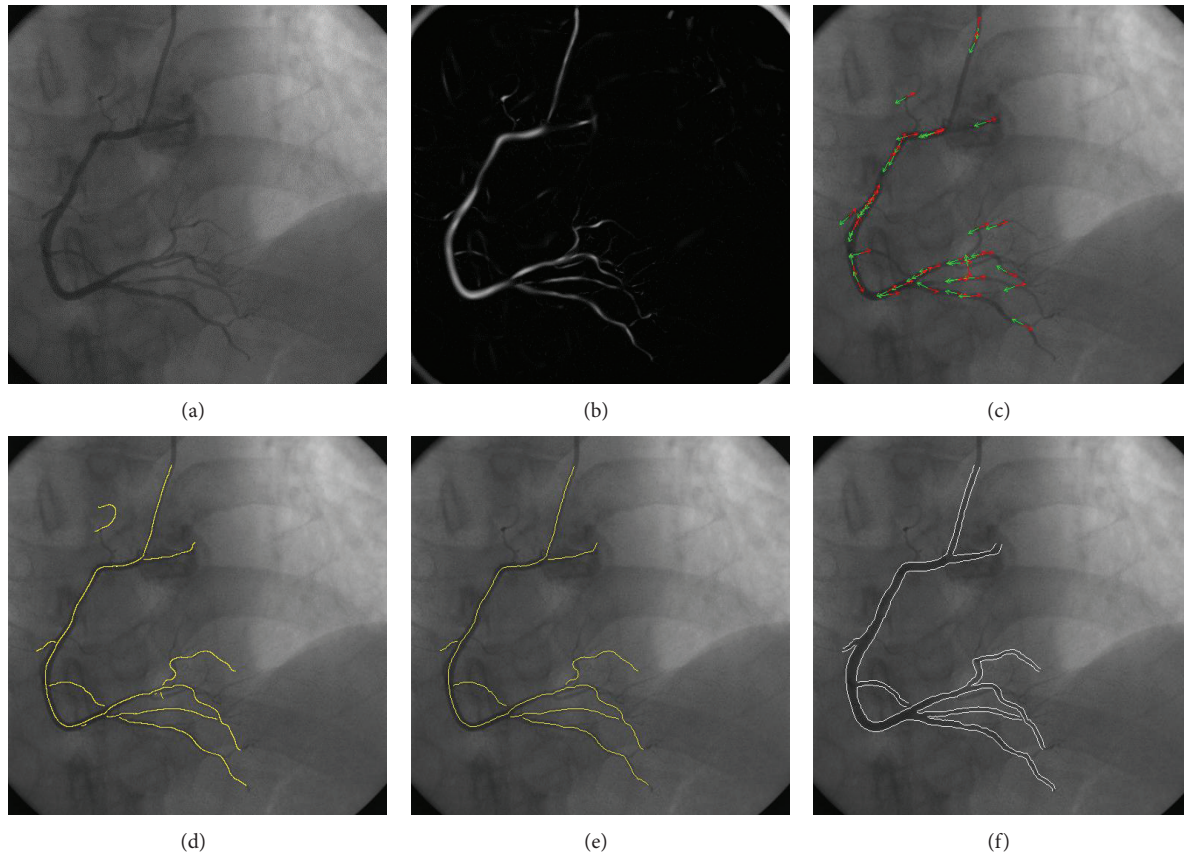


FIGURE 7: Experimental results of the proposed algorithm on a routine coronary angiogram. (a) The original image. (b) MVEF enhancement. (c) Seed determination. (d) Tracking results of (c). (e) Vasculature refinement of (d). (f) Boundaries of coronary artery.

the average computational times are 3.66 s, 3.82 s, and 3.85 s for Aylward, Boroujeni, and the proposed algorithms, respectively. It shows that all these three algorithms take roughly the same computational time for the vessel extraction in angiograms. The computation efficiency can be further improved by integrating GPU based implementations in the future.

3.2. Clinical Angiograms. In order to investigate the applicability and efficiency of the proposed algorithm, the proposed method is also applied to 20 coronary angiograms which were randomly selected from a database routinely acquired from the Philips Digital Imaging System at the Beijing Chaoyang Red-Cross Hospital during invasive catheterization procedures. Here, the experimental result of a random angiogram (Figure 7(a)) is selected to illustrate each step of the calculation. Figure 7(b) is the RE image obtained through the ridge enhancement operation of Figure 7(a), while Figure 7(c) shows the extracted seed points and initial tracking directions, where the red arrows represent the forward directions, while the green arrows depict the backward directions. Figure 7(d) shows the tracking results of Figure 7(c), and Figure 7(e) gives the vasculature refinement results of Figure 7(d). Figure 7(f) shows the boundaries of the extracted vessels. It can be seen from the images that through the process of MVEF, vessel is highlighted and the

background is suppressed in RE image, and it serves as useful auxiliary information for the followed tracking steps. Through the seed determination of the proposed algorithm, it provides a set of seed points on the vascular centerline, and their directions are roughly parallel to the path of the vessels. From the figures, it can be seen that the proposed AGVT algorithm can extract main structure of coronary artery. Figure 8 shows four representative tracking results from these 20 angiograms, and we can see that the main structure of the coronary arteries can also be extracted by the proposed algorithm.

Figure 9(a) shows a section of curved vessel for which the gray distribution is irregular. Figures 9(b), 9(c), and 9(d) show the tracking results of Aylward, Boroujeni, and the proposed algorithms, respectively. It can be seen that the tracking result of Aylward algorithm is more likely to change with the variation of gray level, which hence is more dependent on the gray level distribution of the angiogram. For Boroujeni algorithm, the detected centerline jitters significantly because it tracks the ridgeline rather than the geometrical center of the vascular structures. The proposed algorithm works better than the other algorithms as it adaptively extracts the geometrical centerline of the coronary artery and is more robust in processing irregular vascular segments.

Despite the advances of the proposed algorithm demonstrated in this paper, Figure 10 shows two challenging

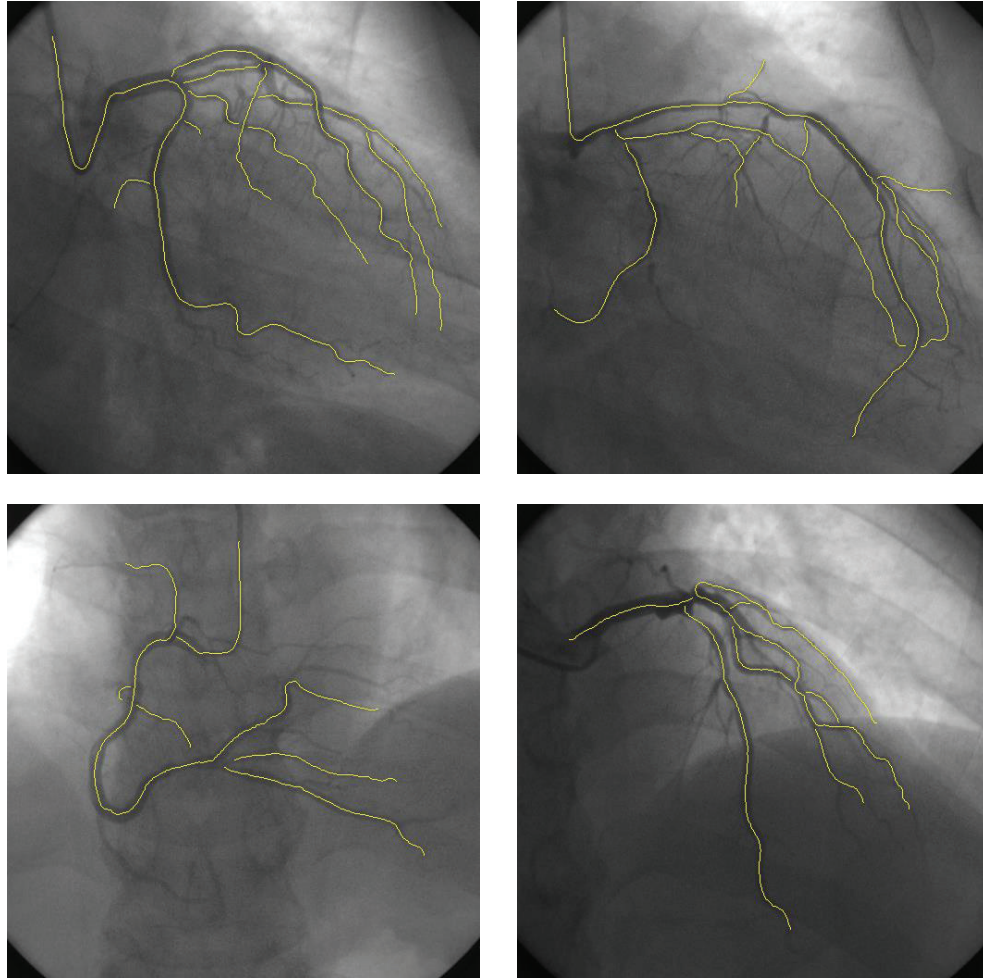


FIGURE 8: The other four examples of the tracked results for the proposed method.

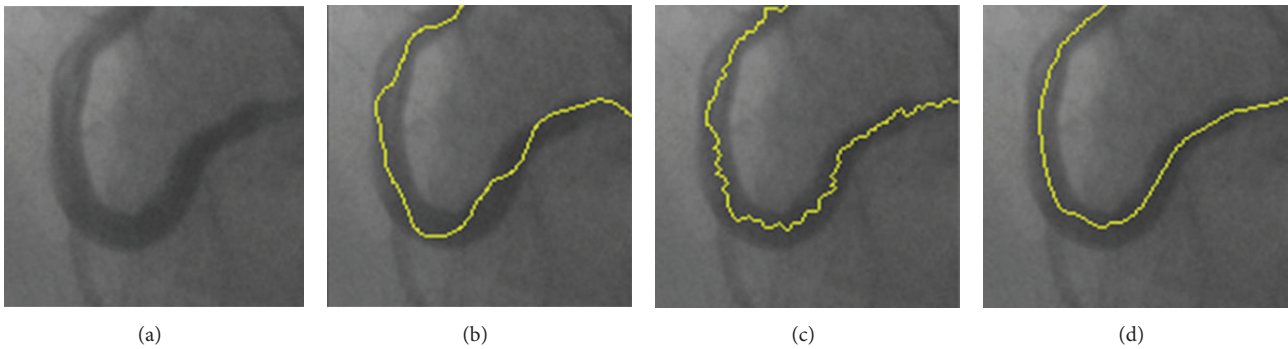


FIGURE 9: Partial enlargement of the vasculature extraction results. (a) The original image. (b) Results of Aylward algorithm. (c) Results of Boroujeni algorithm. (d) Results of the proposed algorithm.

angiograms from the set of 20 angiograms on which the proposed algorithm is only partially successful. It can be seen from Figure 10 that the proposed algorithm is failed for areas with overflowing (a) or incomplete filling (b) of the contrast agents in the angiograms. Up to know, segmentation of the vessels in such an angiogram is still a very challenge task.

4. Conclusions

The major contribution of this proposed algorithm is providing an automatic AGVT framework for coronary artery extraction by putting forward three major key steps named ridge enhancement, seed determination, and adaptive

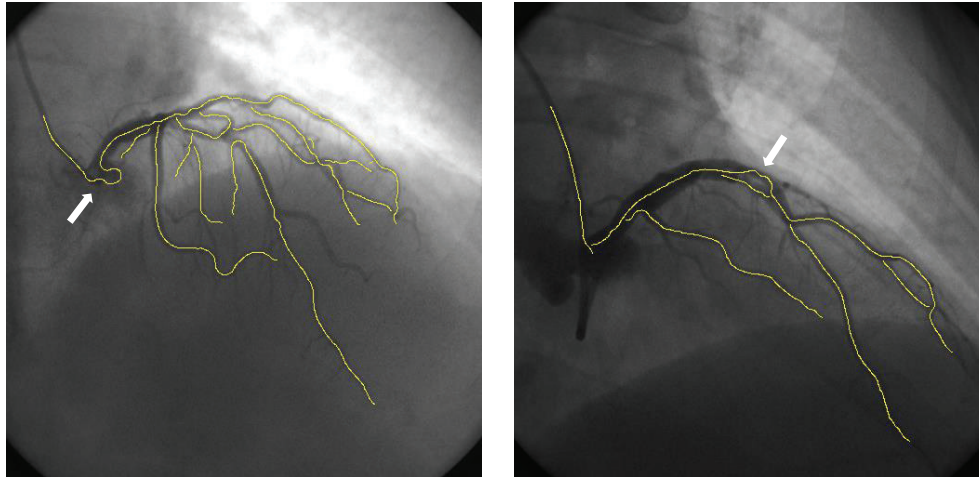


FIGURE 10: Two examples of challenging angiograms on which the proposed algorithms partially failed. The white arrows point to the partial failure tracking areas.

tracking. The proposed algorithm makes three key advances. First, considerable validated seed points and their tracking directions are automatically detected from angiograms, and it ensures the tracking affected without the interference of human factors. Second, it tracks coronary artery from angiograms without constructing templates, and, hence, the calculation complexity is greatly reduced. Third, the extracted ridge points are adaptively adjusted to the corresponding geometrical center, and it has been shown to work well with angiograms of low image quality. From the experiments on synthetic data and real angiograms, it can be stated that the proposed AGVT algorithm is more accurate and stable than the current widely used algorithms.

Conflict of Interests

The authors declare that they have no competing interests.

Acknowledgments

This work was supported by the National Basic Research Program of China (2010CB732505, 2013CB328806), the Key Projects in the National Science & Technology Pillar Program (2013BAI01B01), the National Science Foundation Program of China (61179020), and the Plan of Excellent Talent in Beijing (2010D009011000004).

References

- [1] World Health Organization, "The top ten causes of death-Fact sheet N310," October 2008.
- [2] A. M. Neubauer, J. A. Garcia, J. C. Messenger et al., "Clinical feasibility of a fully automated 3D reconstruction of rotational coronary X-ray angiograms," *Circulation*, vol. 3, no. 1, pp. 71–79, 2010.
- [3] G. Shechter, J. R. Resar, and E. R. McVeigh, "Displacement and velocity of the coronary arteries: cardiac and respiratory motion," *IEEE Transactions on Medical Imaging*, vol. 25, no. 3, pp. 369–375, 2006.
- [4] S. Zheng and Y. Qi, "Motion estimation of 3D coronary vessel skeletons from X-ray angiographic sequences," *Computerized Medical Imaging and Graphics*, vol. 35, no. 5, pp. 353–364, 2011.
- [5] D. Schäfer, J. Borgert, V. Rasche, and M. Grass, "Motion-compensated and gated cone beam filtered back-projection for 3-D rotational X-ray angiography," *IEEE Transactions on Medical Imaging*, vol. 25, no. 7, pp. 898–906, 2006.
- [6] R. Liao, D. Luc, Y. Sun, and K. Kirchberg, "3-D reconstruction of the coronary artery tree from multiple views of a rotational X-ray angiography," *The International Journal of Cardiovascular Imaging*, vol. 26, no. 7, pp. 733–749, 2010.
- [7] J. Yang, Y. Wang, Y. Liu, S. Tang, and W. Chen, "Novel approach for 3-D reconstruction of coronary arteries from two uncalibrated angiographic images," *IEEE Transactions on Image Processing*, vol. 18, no. 7, pp. 1563–1572, 2009.
- [8] C. Blondel, G. Malandain, R. Vaillant, and N. Ayache, "Reconstruction of coronary arteries from a single rotational X-ray projection sequence," *IEEE Transactions on Medical Imaging*, vol. 25, no. 5, pp. 653–663, 2006.
- [9] U. Jandt, D. Schäfer, M. Grass, and V. Rasche, "Automatic generation of 3D coronary artery centerlines using rotational X-ray angiography," *Medical Image Analysis*, vol. 13, no. 6, pp. 846–858, 2009.
- [10] Y. Qian, S. Eiho, N. Sugimoto, and M. Fujita, "Automatic extraction of coronary artery tree on coronary angiograms by morphological operators," *Computers in Cardiology*, pp. 765–768, 1998.
- [11] Y. Sun, "Automated identification of vessel contours in coronary arteriograms by an adaptive tracking algorithm," *IEEE Transactions on Medical Imaging*, vol. 8, no. 1, pp. 78–88, 1989.
- [12] S. R. Aylward and E. Bullitt, "Initialization, noise, singularities, and scale in height ridge traversal for tubular object centerline extraction," *IEEE Transactions on Medical Imaging*, vol. 21, no. 2, pp. 61–75, 2002.
- [13] F. Zamani Boroujeni, R. W. O. Rahmat, N. Mustapha, L. S. Affendey, and O. Maskon, "Coronary artery center-line extraction using second order local features," *Computational and Mathematical Methods in Medicine*, vol. 2012, Article ID 940981, 20 pages, 2012.

- [14] Z. Shoujun, Y. Jian, W. Yongtian, and C. Wufan, "Automatic segmentation of coronary angiograms based on fuzzy inferring and probabilistic tracking," *BioMedical Engineering Online*, vol. 9, article 40, 2010.
- [15] K. Haris, S. N. Efstratiadis, N. Maglaveras, C. Pappas, J. Gourasas, and G. Louridas, "Model-based morphological segmentation and labeling of coronary angiograms," *IEEE Transactions on Medical Imaging*, vol. 18, no. 10, pp. 1003–1015, 1999.
- [16] R. Poli and G. Valli, "An algorithm for real-time vessel enhancement and detection," *Computer Methods and Programs in Biomedicine*, vol. 52, no. 1, pp. 1–22, 1997.
- [17] O. Wink, W. J. Niessen, and M. A. Viergever, "Multiscale vessel tracking," *IEEE Transactions on Medical Imaging*, vol. 23, no. 1, pp. 130–133, 2004.
- [18] M. Sofka and C. V. Stewart, "Retinal vessel centerline extraction using multiscale matched filters, confidence and edge measures," *IEEE Transactions on Medical Imaging*, vol. 25, no. 12, pp. 1531–1546, 2006.
- [19] S. Y. Tang, Y. T. Wang, and Y.-W. Chen, "Application of ICA to X-ray coronary digital subtraction angiography," *Neurocomputing*, vol. 79, pp. 168–172, 2012.
- [20] Y. Bentoutou, N. Taleb, M. Chikr El Mezouar, M. Taleb, and L. Jetto, "An invariant approach for image registration in digital subtraction angiography," *Pattern Recognition*, vol. 35, no. 12, pp. 2853–2865, 2002.
- [21] P. Zou, P. Chan, and P. Rockett, "A model-based consecutive scanline tracking method for extracting vascular networks from 2-D digital subtraction angiograms," *IEEE Transactions on Medical Imaging*, vol. 28, no. 2, pp. 241–249, 2009.
- [22] A. Frangi, W. Niessen, K. Vincken, and M. Viergever, "Multiscale vessel enhancement filtering," in *Proceedings of the Medical Image Computing and Computer-Assisted Intervention (MICCAI '98)*, pp. 130–137, 1998.
- [23] T. Lindeberg, "Edge detection and ridge detection with automatic scale selection," *International Journal of Computer Vision*, vol. 30, no. 2, pp. 117–154, 1998.
- [24] T. Lindeberg, *Scale-Space Theory in Computer Vision*, Springer, New York, NY, USA, 1994.
- [25] D. Eberly, R. Gardner, B. Morse, S. Pizer, and C. Scharlach, "Ridges for image analysis," *Journal of Mathematical Imaging and Vision*, vol. 4, no. 4, pp. 353–373, 1994.
- [26] I. J. Schoenberg, *Cardinal Spline Interpolation*, vol. 12, SIAM, Philadelphia, Pa, USA, 1973.
- [27] P. Xue and D. L. Wilson, "Detection of moving objects in pulsed-x-ray fluoroscopy," *Journal of the Optical Society of America A*, vol. 15, no. 2, pp. 375–388, 1998.
- [28] Y. Xu, H. Zhang, H. Li, and G. Hu, "An improved algorithm for vessel centerline tracking in coronary angiograms," *Computer Methods and Programs in Biomedicine*, vol. 88, no. 2, pp. 131–143, 2007.
- [29] H. Greenspan, M. Laifenfeld, S. Einav, and O. Barnea, "Evaluation of center-line extraction algorithms in quantitative coronary angiography," *IEEE Transactions on Medical Imaging*, vol. 20, no. 9, pp. 928–941, 2001.